Bjørn Markus Qvenild-Svennungsen

Experimental Study of Microparticle Aggregation Inside a Sessile Droplet Subjected to Surface Acoustic Waves

Master's thesis in Mechanical Engineering
Supervisor: Maria Fernandino
Co-supervisor: Etien Martinez Roman and Diego Sánchez Saldaña
June 2023

Master's thesis

NTNU
Norwegian University of
Science and Technology

Bjørn Markus Qvenild-Svennungsen

Experimental Study of Microparticle Aggregation Inside a Sessile Droplet Subjected to Surface Acoustic Waves

Master's thesis in Mechanical Engineering
Supervisor: Maria Fernandino
Co-supervisor: Etien Martinez Roman and Diego Sánchez Saldaña
June 2023

Norwegian University of Science and Technology
Faculty of Engineering
Department of Energy and Process Engineering

NTNU
Norwegian University of
Science and Technology

Sammendrag

Innovative metoder for å manipulere partikler og celler i blandinger har hatt enorm innvirkning i medisinsk progresjon i det siste århundre. Det spiller en avgjørende rolle i å takle ulike medisinske utfordringer, spesielt innen klinisk diagnostikk og terapeutikk. Dette krever nøyaktig kontroll av partiklenes oppførsel, og en harmløs og effektiv metode for partikkelaggregering er bruken av akustiske bølger.

Målet med denne masteroppgaven er å undersøke partikkelaggregeringsmønsterene inne i en stasjonær dråpe utsatt for akustiske overflatebøler produsert av spiral interdigital transdusere (IDT) for ulike frekvenser. Karakterisering av de distinkte aggregeringsmønsterene oppnådd for 7 μm polystyrene (PS) partikler inne i den 2 μL dråpen ble studert. Undersøkelsen ble gjennomført eksperimentelt for varierende frekvenser på 20 MHz, 40 MHz, 80 MHz og 120 MHz med en inngangseffekt på 100 mW for multisystemet. En kvalitativ undersøkelse av de innflytelsesrike hydrodynamiske effektene og den akustiske strålingskraften er adressert for å tilegne en bredere forståelse av aggregeringsmekanismen.

Resultatene viste at det høyere frekvensområdet akkumulerer partiklene i klynger, med en singel klynge som raskt dannes ved 80 MHz og flere klynger observert ved en frekvens på 120 MHz. Til motsetning fanget de lavere frekvensene på 20 MHz og 40 MHz partiklene i 2D konsentriske ringformasjoner på bunnen av dråpen. Avstanden mellom de konsentriske ringene ble målt til å være omtrent halvparten av bølgelengden til de akustiske bølgene i væsken. Disse resultatene indikerer en dominerende kraftkonvertering henhold til frekvensområdet. Hydrodynamiske effekter indusert av den akustiske strømmen inne i dråpen er mer dominerende ved høyere frekvenser, noe som resulterer i flere virvler i strømmen som er i stand til å samle partikler til klynger. Til motsetning, ved lavere frekvenser dominerer den akustiske strålingskraften, og trykknodene til det stående feltet av akustiske overflatebøler i bunnen av dråpen tiltrekker seg partiklene, som resulterer i den fangede ringformasjonen.

Enkeltsystemet opererte med en inngangseffekt på 100 mW for de forskjellige frekvensene, som resulterte i konsentriske ringer med en frekvens på 20 MHz, mens klyngeformasjoner ble observert at 120 MHz. I motsetning til multisystemet, ble makropartikler produsert med en frekvens på 40 MHz. Et fasediagram ble konstruert ved å justere både inngangseffekten og driftsfrekvensen, som avslørte seks aggregeringsregimer. Fasediagrammet viste at enkeltsystemet kan generere det samme aggregeringsmønsteret som multisystemet ved å velge passende inngangseffekt og driftsfrekvens. Den mest optimale konfigurasjonen for konsentrisk partikkelfanging ble funnet å være 5 mW for 20 MHz-konfigurasjonen og 10 mW for 40 MHz-konfigurasjonen. Til motsetning, en høy inngangseffekt på 200 mW for 120 MHz-konfigurasjonen ble funnet å være mest effektiv for multiklynge aggregering.

Abstract

Innovative methods for manipulating particles and cells in mixtures have greatly impacted medical progression in the recent century. It plays a crucial role in tackling various medical challenges, particularly in the domains of clinical diagnostics and therapeutics. This requires accurate control over the behaviour of the particles, and one method for harmless and effective particle aggregation is the use of acoustic waves.

The aim of this thesis is to investigate the particle aggregation pattern inside a sessile droplet subjected to surface acoustic waves (SAW) generated by spiral interdigital transducers (IDT) for various frequencies. Characterisation of the distinct aggregation pattern obtained for 7 μm polystyrene (PS) particles inside a 2 μL droplet was studied. The investigation is conducted experimentally at various frequencies of 20 MHz, 40 MHz, 80 MHz, and 120 MHz with an input power of 100 mW for the multi-system. A qualitative examination of the influential hydrodynamic effects and acoustic radiation force is addressed to gain a broader understanding of the aggregation mechanism.

The results showed that the higher frequency range accumulates the particles into clusters, with a single cluster rapidly forming at 80 MHz and multiple clusters observed at a frequency of 120 MHz. Conversely, the lower frequencies of 20 MHz and 40 MHz trapped the particles in 2D concentric ring formations at the bottom of the droplet. The spacing between the concentric rings was measured to be roughly half the wavelength of the acoustic waves in the liquid. These results are obtained from a dominant force conversion corresponding with the frequency. Hydrodynamic effects induced by the acoustic streaming inside the droplet are more dominant at higher frequencies, resulting in multiple vortices in the flow capable of accumulating particles in the vortex centre to create clusters. At lower frequencies, the acoustic radiation force dominates, and the pressure nodes of the standing SAW field at the bottom attract the particles towards them, resulting in the entrapment of particles.

Operating the single-system at an input power of 100 mW for the various frequencies resulted in concentric rings at a frequency of 20 MHz, whereas cluster formations were observed at 120 MHz. However, unlike the multi-system, macro particles were produced at a frequency of 40 MHz. A phase diagram was constructed by tuning both the input power and operational frequency, which revealed six aggregation regimes. The phase diagram demonstrated that the single-system can generate the same aggregation pattern as the multi-system by selecting the appropriate input power and operational frequency. The most optimal configuration for concentric particle trapping at low frequencies was found to be 5 mW for the 20 MHz configuration and 10 mW for the 40 MHz configuration. Conversely, a high input power of 200 mW for the 120 MHz configuration was found to be efficient and optimal for multiclusters aggregation.

Acknowledgement

I would like to express my sincere gratitude to my supervisor Prof. Maria Fernandino for introducing me to the fascinating topic of acoustofluidics and allowing me to be a part of the Thermal Two-Phase Flow Lab (Th2FLAB) research group. Her expertise, availability, and helpfulness have been invaluable throughout the project, and she has always been there to guide me through any questions or difficulties that I encountered. Additionally, I am deeply grateful to my co-supervisors; PhD candidate Diego Sánchez Saldaña and postdoc Etien Martinez Roman. Throughout the journey of this project, Diego S. Saldaña has been remarkably helpful and supportive, sharing his extensive knowledge of acoustofluidics with me and engaging in challenging and enlightening discussions. He has also taught me how to operate the experimental equipment to obtain high-quality results. I would like to express my appreciation for Etien M. Roman for his inspiring rational and critical thinking, his contributions to valuable discussions, and his encouragement to investigate a sessile droplet. His knowledge and positive personality are highly admirable.

Contents

Figures

Tables

Acronyms

Symbols

Chapter 1

Introduction

The progression of medicine in the recent century has been greatly influenced by the emergence of inventive methodologies that facilitate the manipulation of particles and cells in mixtures. Effective manipulation of both synthetic and biological particles that are suspended in small liquid volumes plays a critical role in tackling various medical challenges, particularly in the domains of clinical diagnostics and therapeutics. Precise manipulation of particles is crucial for the effective functioning of lab-on-a-chip devices and point-of-care diagnostics which are essential in bio-sensors. This requires accurate control over their motion, such as levitation [1], trapping [2], transportation [3], separation [4] and aggregation [5][6].

1.1 Motivation

Ahmed et al. [7] have reviewed a variety of on-chip techniques available today. These techniques include both passive and active actuation mechanisms. Passive mechanisms rely on the topology [8] and geometry [9] of the system to manipulate particles while active mechanisms use external forcing, such as thermal [10], mechanical [11], electrokinetic [12], magnetic[13] or acoustic effects [14] to manipulate the particles. Passive mechanisms are simpler, but they are limited by their fixed geometry, which restricts the degree of flow intensity tuning. Additionally, these mechanisms require the assistance of pumps to compensate for a pressure drop caused by the fixed geometry. Active systems are more complex to implement but offer the flexibility of active regulation of the flow field. However, both electrokinetic and mechanical actuation have reliability issues and wear due to the wear of the chemical surface over time and moving parts, respectively. Besides, some electrokinetic systems have an increased risk of evaporation effects, large pressure drops and channel clogging, leading to a growing need for pumps to drive the flow. Extended exposure to high temperatures can harm biosamples, making thermal actuation mechanisms unsuitable for particle manipulation. Magnetic actuation

methods work great for manipulating magnetic beads, however, the process becomes more complex when transitioned over to bioparticles. In that case, the cells must be labelled with a magnetic probe before the manipulation can take place [13]. This is very inconvenient for bio-sensors.

Acoustic actuation is a feasible alternative to the aforementioned methods for exciting microparticles in a harmless manner. This approach enables flexible tuning of the centrifugal intensity by modifying the frequency or/and input power. Furthermore, it remains unaffected by the electric or magnetic characteristics of the particles. The system's minimal, fast, real-time setup and easy-to-use configuration makes it suitable for medical practitioners such as doctors or nurse. Acoustic actuation also allows for contact-free manipulation, reducing the risk of contamination. While piezoelectric substrates used in acoustic actuation tend to be more expensive than other materials used in microfluidic devices, such as regular silicon wafers, this approach doesn't require a large sample volume to perform analysis, making it more operational cost-efficient and allowing for multiple experiments from one sample [7].

The manipulation of suspended particles through sound waves is made possible by acoustic actuation mechanisms. This combination of sound waves and fluid flow is referred to as acoustofluidics. Electrodes on the surface of the piezoelectric substrate generate surface waves that travels along the air-substrate interface. When these waves encounter the liquid on the substrate, kinetic energy is transferred to the flow, inducing hydrodynamics. Thereby influencing the motion of microparticles present in the liquid.

The use of acoustofluidics has been applied to the segregation of cells and their exosomes, particularly extracellular vesicle (EV) that are released by the parent cell and possess an average diameter ranging from 30 to 150 nm. Exosomes carry information about their parent cell. Researchers can obtain vital insights into the cancer cell by precisely isolating both cancer cells and their corresponding exosomes. As a result, this technology plays a significant role in the advancement of early cancer detection and cancer research [15].

Various setups for particle manipulation through acoustic actuation exist today, like, for example, microchannels [16], chambers [17] and cylinders [18]. However, these systems typically consist of external structures to withhold the liquid, making them more complex and less portable. The structure is positioned between the electrodes and the liquid, implying that the waves have to propagate through the structure to reach the liquid. When doing so, the structures will attenuate the waves such that waves are weakened when they enter the liquid. Furthermore, microchannels usually consist of pumps to drive the fluid medium, which increases the complexity of the system. On the contrary, a sessile droplet deposited directly onto the surface of the substrate exhibits far less complexity while still managing to effectively manipulate the particles.

In a recent study conducted by Han et al. [19], synthetic polystyrene (PS) particles measuring 3 μm and 7 μm in diameter were successfully aggregated and segregated in a sessile droplet. This was achieved through the application of surface waves from two straight electrodes situated on opposite ends of the droplet. The experiment was conducted at varying frequencies of 19.1 MHz, 30.6 MHz, 62 MHz, and 98 MHz. The researchers concluded that higher frequencies result in easier particle aggregation and segregation as compared to lower frequencies. Observations also showed that 7 μm particles tend to aggregate easier than 3 μm

particles.

In a recent study, Song et al. [20] explored flow patterns for different sized polystyrene particles suspended in sessile droplets of varying viscosity. Using progressive helical electrode design, they successfully aggregated particles measuring 5 μm and 10 μm in diameter into a single cluster at a frequency of 20 MHz and an input power of 200 mW. However, this aggregation pattern was not observed for smaller particles, confirming the aforementioned observations made by Han et al. [19] that only larger particles tend to cluster.

The spiral design of the electrodes has gained increasing attention the recent years for its ability to effectively form vortices in the flow that aggregate particles [21, 22]. Destgeer et al. [21] conducted experiments with spiral electrodes to aggregate particles into a cluster by using frequencies below 40 MHz, where the radiative force at the bottom of the droplet is more dominant. The authors reported that an increase in frequency would result in more dominant hydrodynamics in the droplet and less radiative effects at the bottom. In their recent study, Zhang et al. [22] successfully achieved the aggregation and segregation of both synthetic PS particles and cells through the creation of centrifugation by the incorporation of a spiral design of the electrode containing tilted fingers, operating at three different frequencies of 40 MHz, 56.5 MHz, and 100 MHz. The outcome of this method was the formation of rings at the periphery of the droplet by smaller polystyrene particles, while larger particles aggregated to a cluster in the centre. In Zhang's study, it was found that spiral electrodes were effective in quickly and consistently separating red blood cells (diameter range of 4-7 μm) from platelets (diameter range of 1-2 μm). This research highlights the potential of spiral electrodes for efficient aggregation and separation processes. The findings in [23] also suggest that other aggregation patterns are possible to observe for various frequencies.

1.2   Goals and objectives

The goal of this work is to investigate particle aggregation patterns inside a sessile droplet subjected to surface acoustic waves (SAW) generated by spiral IDTs, particularly at various and higher frequencies than the ones reported in the literature. The objectives necessary to attain this goal are:

- To characterise the particle aggregation pattern that occurs inside the sessile droplet under the actuation of surface acoustic waves at different frequencies (20 - 120 MHz)

- To qualitatively examine the influential hydrodynamic effects and the radiative forces acting on the particles at different frequencies to gain a better understanding of the aggregation mechanism.

- To compare the particle aggregation behaviour when using one IDT design for each targeted frequency and when using a single IDT operating at different frequencies.

- To further explore new regimes of particle aggregation pattern inside the droplet that occur when tuning the operational frequency and the input power for a single IDT.

For the accomplishment of the proposed objectives, a series of specific subtasks must be undertaken. The initial subtask involves the microfabrication of the acoustofluidic device that can operate within the desired frequency range. The subsequent task address visualising the particle behaviour during the experiments. The following subtask requires testing of the experimental setup to obtain more trustworthy outcomes for the experiments.

1.3   Scope of work

This thesis is focused on the utilization of surface acoustic waves to aggregate micro-sized synthetic particles within a 2 μL water droplet that are deposited on the surface of a piezo-electric material. This thesis facilitates a spiral electrode design at different widths to obtain the various design frequencies of the surface acoustic waves. For the experiments, synthetic microsphere particles with a diameter of 7 μm were utilized. The size of 7 μm is chosen to resemble the size and density of red blood cells [24, 25]. The range of frequencies performed is 20 MHz, 40 MHz, 80 MHz and 120 MHz. Furthermore, any attempt to extract the resulting multicluster is outside the scope of this work and left as part of further future work. Additional exclusion from the thesis is the use of cells.

1.4   Structure / Outline

The report is divided into five chapters that aim to provide a clear understanding of the goal and objectives. The first Section, Sec. 2, provides an overview of particle manipulation principles and the necessary background and theory. The second section, Sec. 3, focuses on the chemicals, machines, and procedures required to create the targeted electrode geometry and the acoustofluidic device. Section 4 describes the experimental setup and procedure, along with potential sources of error. The fourth section, Sec. 5, presents the observed aggregation patterns at various frequencies and discusses the influence of the distinct forces that act on the particles.

Chapter 2

Theory and background

This chapter builds upon the specialisation project [23] completed in the previous semester. Although the theory is similar to that presented in the project, this thesis aims to broaden it by incorporating supplementary literature and theory.

2.1 Generation of electroacoustic waves

Acoustic waves can be generated in piezoelectric materials by converting an external electric potential into mechanical deformation within the substrate. This is referred to as the inverse piezoelectric effect and links electrical signals and mechanical movement in certain materials. Conversely, the phenomenon where mechanical deformation induces electrical signals is referred to as the direct piezoelectric effect.

When an electric potential is applied to the piezoelectric material, it induces a strain along one axis. By alternating the polarity of the electric potential, the piezoelectric material can oscillate between expansion and contraction, producing nanometer-scale displacements at frequencies in the magnitude of 1 Hz to 1 GHz. These oscillations generate acoustic waves in the surrounding medium.

If the external electrical potential is applied to the surface or the volume of the piezo-electric material, surface acoustic waves (SAW) or bulk acoustic waves (BAW) are generated, respectively. SAW-based acoustofluidic devices are designed to generate acoustic waves that propagate along the surface of the piezoelectric material. Most of surface acoustic wavess are classified as Rayleigh waves, whose name was given after its discovery by Lord Rayleigh in 1885 [26]. Figure 2.1 illustrates the lattice motion within the piezoelectric material. Propagating Rayleigh waves have both longitudinal and transverse shear components. Consequently, particles on the surface of the piezoelectric substrate undergo an elliptical motion. The ellipticity of the particle motion attenuates rapidly in the transverse direction of the substrate. This

motion exhibits a close analogy to deep-water waves, which are natural phenomena in the oceanic environment [26].
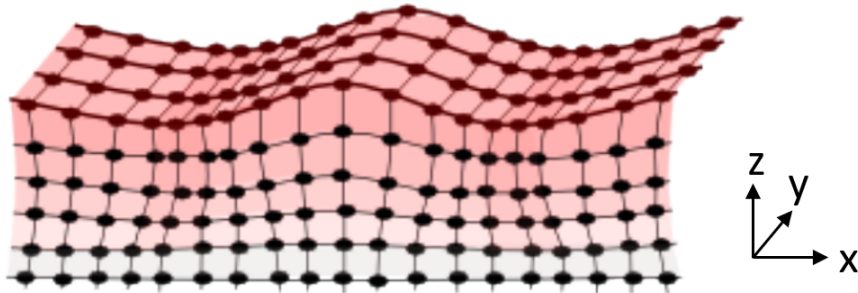
Figure 2.1: When a surface acoustic Rayleigh wave travels through a solid material, it causes the piezoelectric material to experience lattice displacement in both longitudinal and transverse directions. However, the motion of displacement in the transverse direction tends to decay rapidly [27].

A conventional Rayleigh SAW device usually comprises electrodes to generate travelling surface acoustic waves (TSAW)s as depicted in Fig. 2.2a). When two identical electrode patterns are employed and positioned opposite to each other, they produce two counter-propagating TSAWs that interfere with one another, resulting in a standing surface acoustic wave (SSAW) field, as illustrated in Fig. 2.2b). The SSAW field creates pressure nodes (PN)s and antinodes (AN)s, which are commonly utilized for particle manipulation since particles tend to attract to either node, depending on the compressibility and density of the particles.
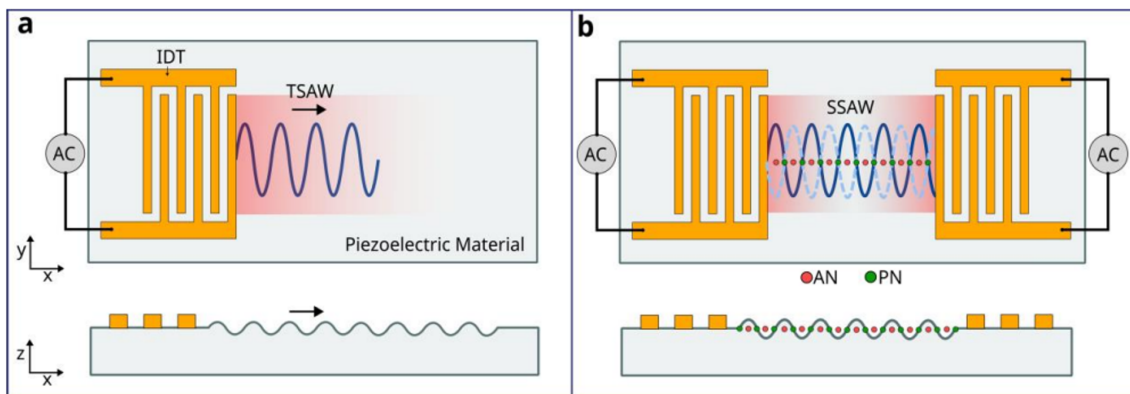
Figure 2.2: Illustration of travelling SAW and standing SAW. a) Travelling surface acoustic waves (TSAW) propagating along the surface of the piezoelectric material. The straight electrodes are responsible for the SAW generation. b) Two straight opposite electrodes both generate SAW that will interfere with each other and create a standing surface acoustic wave (SSAW) field. The waves create zero-pressure points referred to as anti-nodes (AN) and pressure nodes (PN). The particles tend to attract towards either node depending on their density and compressibility. Figure obtained from [28].

2.2 Transducer design

The phenomenon of piezoelectricity has paved the way for the development of efficient mechanisms that convert electrical signals into mechanical displacement through the inverse piezoelectric effect. This process is generated due to metal electrodes that are patterned onto the surface of the piezoelectric material. These metal electrodes are referred to as interdigital transducer (IDT)s and their patterned design affects the characteristics of the surface acoustic waves, such as their wavelength, frequency and propagation direction. Therefore, it is important to optimize the IDT design for its respective purpose and application.
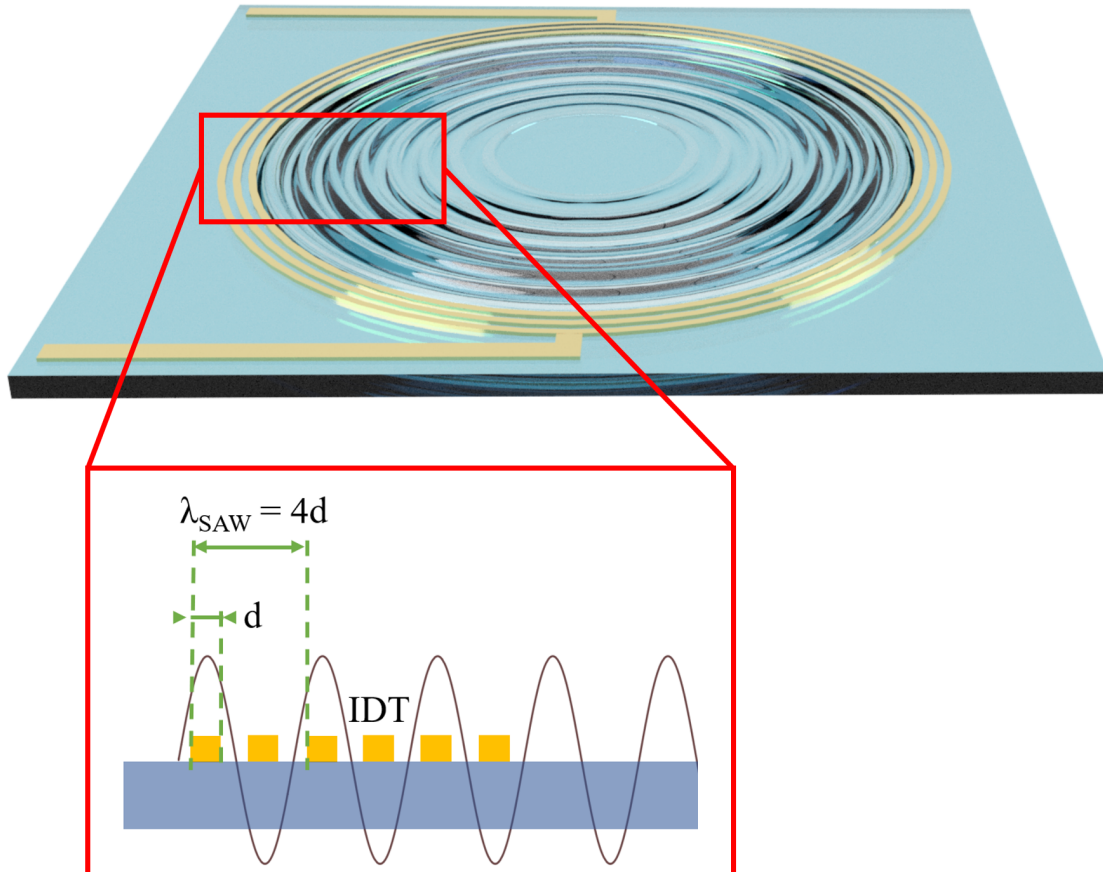
Figure 2.3: A schematic representation of the generation of surface acoustic waves using a spiral IDT. The surface acoustic waves causing the piezoelectric material to oscillate, and the waves propagate in an omnidirectional manner. The width of the IDT bar is denoted d, and the wavelength of the acoustic waves induced by the IDTs is expressed as $\lambda_{SAW} = 4d$.

Figure 2.3 illustrates how the Rayleigh surface acoustic waves from a spiral IDT design make the substrate oscillate as they propagate radial inwards. The magnified subfigure illustrates how the width of the IDT and the spacing between them are of equal distance, denoted d. As a result, the propagating SAW exhibits a wavelength of four times the width of the IDT bar, i.e. $\lambda_{SAW} = 4d$. This relationship is evidently shown in the aforementioned figure.

The design frequency, i.e. the frequency that the acoustofluidic device is designed to operate at given the width of the IDT bar, is identified by knowing the speed of the Rayleigh wave

along the surface of the piezoelectric substrate, v_R, and the width of the IDTs. The design frequency is then expressed by,

$$f = \frac{v_R}{\lambda_{SAW}} = \frac{v_R}{4d}. \tag{2.1}$$

v_R is dependent on the propagation direction of the wave. For example, Ciplys et al. [29] showed v_R to equal 3994 ms^{-1} in the favourable x-direction for a specific cut of the piezoelectric material lithium niobate. This implies that the design frequency f is a function of the inverse width of the IDT, i.e. $f \sim d^{-1}$. Meaning that increasing the width of the IDT bars results in a decrease of the design frequency.

As indicated above, acoustic waves with desirable characteristics are dependent on the properties of the piezoelectric material. A vast collection of such materials exists today, all with their own advantages and limitations. Therefore, choosing the right one becomes a challenge. The next subsection will explain some important materialistic properties for the creation of SAWs, and further introduction of lithium niobate is presented.

2.3   Piezoelectric materials

The mentioned piezoelectric effect is a well-established phenomenon that dates back to the late 19th century and has been widely used in various technologies since the early 20th century. In fact, the piezoelectric effect was discovered already back in 1880 by the renowned brothers and physicists Paul-Jacques Curie and Pierre Curie, who observed this sensation while experimenting with the piezoelectric material quartz [30]. Today, a wide range of applications, such as energy harvesting [31], telecommunication [32], and biosensors [33] utilise the piezoelectric effect in piezoelectric materials.

Piezoelectric materials can mainly be classified into two types of crystalline structures, namely single-crystal and polycrystalline substrates, both with their respective advantages and limitations. In single-crystal materials, the internal lattice orientation is uniformly distributed throughout the solid [34]. Therefore, these structures exhibit a higher quality factor compared to polycrystalline structures, indicating lower energy loss per cycle of the wave propagation in the material. This leads to less attenuation of the wave amplitude per cycle, resulting in more persistent waves. Thus, the quality factor characterizes the degree of underdamping of the oscillations [35]. A high quality factor is greatly preferable and especially compatible with acoustofluidic devices that utilise propagating acoustic waves. The quality factor also depends on the number of electrode bars that the spiral IDT exhibits. The amount of electrode bars is reflected in how many circular turns the spiral IDT consists of. The higher number of IDT turns, the higher the quality factor. Consequently, less energy loss per oscillation is provided [36].

On the other hand, polycrystalline materials exhibit an internal lattice structure built up by various single crystal grains [34]. They facilitate piezoelectric applications due to their great advantage of effectively transferring electrical energy to mechanical energy. This quantitative parameter is referred to as the electromechanical coupling coefficient and indicates the converted energy with respect to the supplied energy [29]. The high electromechanical coupling coefficient have made the polycrystalline materials very applicable for acoustofluidics, with the

most common being the lead zirconate titanate (PZT) [37]. Unfortunately, PZT suffers some limitations, such as low wave velocity, low-quality factor and high energy loss [35]. Additionally, PZT contains excess lead oxide, making it toxic. As a result, regulatory measures have been introduced with the intention of eradicating its presence from daily usage [38] [39].

Multiple replacements for the toxic PZT piezoelectric material have been discovered in recent years, among them the single crystalline material lithium niobate (LN) expressed by its chemical formula $LiNbO_3$. Lithium niobate exhibits far less energy loss compared to PZT and it is more compatible with microfabrication. Additionally, lithium niobate also exhibit a relatively larger electromechanical coupling coefficient compared to other single crystalline piezoelectric materials [35].

Lithium niobate (LN) is a highly anisotropic material, meaning that its properties are dependent on the orientation and direction of the substrate. To optimize the energy transition into mechanical deformation indicated by the electromechanical coupling coefficient, the orientation of the wafer is of utmost importance. In 1976, Shibayama et al. [40] conducted a study to determine the optimal configuration of lithium niobate, and their findings have remained highly influential in the field. According to their research, the 127.86° Y-rotated X-propagating cut, also referred to as the 128° YX cut, exhibits the highest electromechanical coupling coefficient while simultaneously being free of any wave disturbances. The favourable direction of wave propagation is along the x-direction where the electromechanical coupling coefficient is relatively high. Figure 2.4 A illustrates the local coordinate system of the LN wafer, while Fig. 2.4 B illustrates the 128° rotation from the Y-axis. Given its superior properties, the 128YX cut remains a popular choice for a wide range of applications.
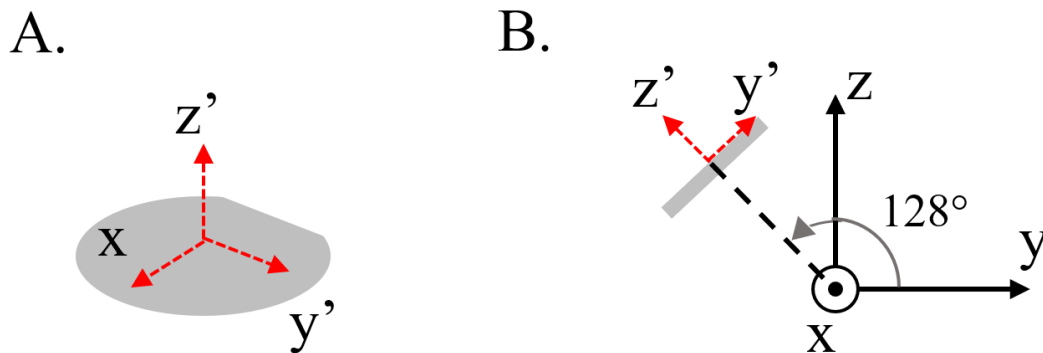
Figure 2.4: Description of the 128° Y-rotated X-propagating cut (128 YX cut) of the lithium niobate wafer. Subfigure A. shows the local coordinate system of the wafer, where the x-axis is the direction of favourable wave propagation. Subfigure B. showcase the 128° rotation from the Y-axis.

2.4   Fluid manipulation in sessile droplets

Acoustofluidic devices that rely on sessile droplets are commonly designed to position the droplet in the wave field of a propagating SAW on the surface of a piezoelectric material. As

waves propagate along the surface, they will penetrate the periphery of the droplet and affects the internal flow. Variation in the position of the droplet relative to the wave propagation direction will cause the waves to dissipate differently within the liquid, leading to distinct flow dynamics. As a result, the particles inside the droplet will act differently depending on the flow field. Therefore, the position of the droplet relative to the propagation direction of the waves is important. A spiral IDT is optimal for omnidirectional wave propagation along the surface of the substrate. A sessile droplet is positioned in the centre of the spirals to experience the entire wave field.
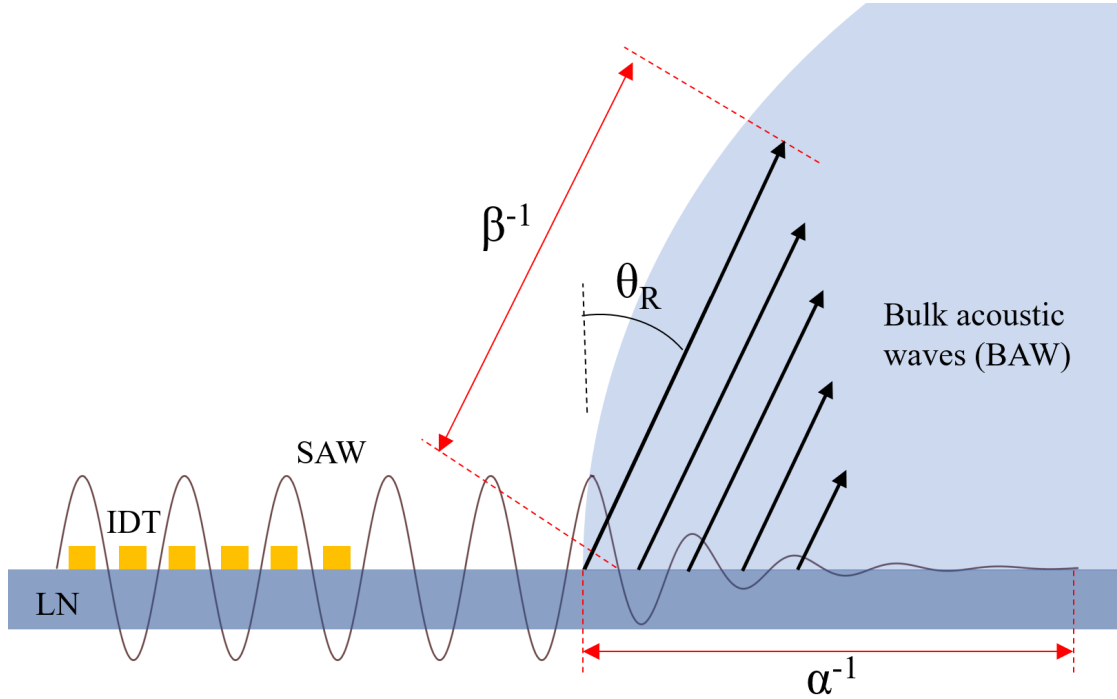
Figure 2.5: Schematic of the wave interference with the sessile droplet. Surface acoustic waves (SAW) propagate along the surface of the lithium niobate (LN) substrate before interfering with the droplet. The SAW along the liquid-substrate interface will attenuate inside the droplet. The distance in which this SAW wave will decay by a factor of e inside the droplet is given by α^{-1}. Additionally, the acoustic wave will refract with the Rayleigh angle, θ_R, upon entering the periphery of the droplet. The refracted acoustic waves propagate into the volume of the liquid, hence referred to as bulk acoustic waves (BAW). The attenuation length corresponding to the BAW is denoted β^{-1}.

The hydrodynamic movement is referred to as streaming and is caused by the refraction of the acoustic waves upon encountering the droplet. This results in the propagation of bulk acoustic waves within the volume of the liquid. The acoustic wave refracts with an angle referred to as the Rayleigh angle (θ_R), expressed by the equation

$$\theta_R = \sin^{-1}\left(\frac{v_l}{v_R}\right), \tag{2.2}$$

where v_l and v_R denotes the speed of sound in the liquid and velocity of the Rayleigh SAW along the surface of the substrate, respectively. Figure 2.5 illustrates how the SAW refract with the Rayleigh angle into the liquid to produce BAW. For the 128° YX lithium niobate cut

considered above, the propagating SAW will refract with a Rayleigh angle $\theta_R = 21.8$ ° for v_l and v_R equal to 1485 ms^{-1} [36] and 3994 ms^{-1} along the x-direction [29], respectivly.

Furthermore, Fig. 2.5 illustrates how the incoming SAW attenuates along the solid-liquid interface and into the volume of the droplet. The propagating BAW in the volume experiences a decrease in energy due to viscous dissipation, implying that some of the acoustic energy is converted into thermal energy in the liquid. This happens because the oscillating wave pressure from the BAW induces movement in the droplet, referred to as acoustic streaming, i.e acoustic energy in the wave is transformed into kinetic energy in the fluid.

On the other hand, the propagating SAW along the solid-liquid interface in the droplet experience a decrease in energy due to dilatative dissipation. This happens when the SAW causes the solid surface to oscillate underneath the liquid. The oscillating wave motion of the substrate induces oscillations in the liquid in the region close to the bottom. Energy is required to oscillate the liquid, resulting in more energy being lost in this process.

The decrease in acoustic energy along the solid-liquid interface results in damping of the oscillating SAW, i.e. the wave will attenuate. To quantify this attenuation, Arzt et al. [41] came up with a theoretical formula for calculating the distance in which the encountering wave will decay by a factor of e inside the droplet. This attenuation length of the wave along the solid-liquid interface is denoted α^{-1} and expressed as

$$\alpha^{-1} = \frac{\rho_s v_R \lambda_{SAW}}{10^3 \cdot \rho_f v_l}, \tag{2.3}$$

where ρ_s and ρ_f are the density of the solid and fluid, respectively, and λ_{SAW} is the wavelength of the SAW. By expressing Eq. 2.1 with respect to λ_{SAW}, the aforementioned equation can be rewritten as

$$\alpha^{-1} = \frac{\rho_s v_R^2}{10^3 \cdot \rho_f v_l f}. \tag{2.4}$$

Not only does wave attenuation occur along the solid-liquid interface, but it also occurs within the droplet itself as the bulk acoustic wave diminishes due to the mentioned viscous dissipation. The attenuation length for the BAW in the liquid β^{-1} is given by the equation [42]

$$\beta^{-1} = \frac{10^3 \rho_f v_l^3}{4 \cdot \pi^2 f^2 \left(\frac{4}{3}\mu + \mu'\right)}, \tag{2.5}$$

where μ' and μ represent the bulk and shear viscosities of the fluid, respectively.

Figure 2.5 illustrates the attenuation lengths in both directions, α^{-1} and β^{-1}. Observe from the equations that the attenuation lengths are a function of the frequency, i.e. $\alpha^{-1} \propto f^{-1}$ and $\beta^{-1} \propto f^{-2}$. An increase in frequency will result in a decrease in attenuation length for both directions, as shown in Tab. 2.1. α^{-1} and β^{-1} are calculated based on the parameters given by Kushibiki et al. [43] (ρ_s = 4647 kg/m^{-3}) and Holmes et al. [44] (ρ_f = 997 kg/m^{-3}, μ = 8.88e-4 Pas and μ' = 2.47e-3 Pas at 25 °C). Speed of the sound in water, v_l, and speed of SAW, v_R, are provided above for the Rayleigh angle, θ_R.

Table 2.1: Attenuation length of the acoustic wave along the liquid-substrate interface expressed as α^{-1} (Eq. 2.4) and attenuation length of the refracted acoustic wave in the liquid, expressed as β^{-1} (Eq. 2.5), both with respect to the targeted frequencies.

f [MHz]	α^{-1} [mm]	β^{-1} [mm]
20	2.5	57
40	1.3	14
80	0.63	3.5
120	0.42	1.6

2.4.1 Influential forces

The particles within the droplet in an acoustofluidic system experience various forces due to the acoustic waves, the hydrodynamics and the interaction of other particles. The latter includes van der Waals forces and electrically-driven forces, like electrostatics and electrodynamics. However, these forces are assumed to be negligible for micro-sized polystyrene (PS) particles in acoustofluidic [36]. Additionally, the density of the PS particles, 1.06 g/mL [45], is roughly the same density of the water liquid, 1.00 g/mL, hence the gravitational force and buoyancy force cancel each other out. There are mainly three effects acting on the particles inside the droplet. Acoustic radiation force ARF (direct and indirect) that arises from the acoustic waves along the surface, centripetal force induced by the vortex motion and drag force from the hydrodynamics, which in turn is induced by the acoustic streaming.

Indirect acoustic force occurs when the propagating acoustic wave interferes with a particle which in turn will start to oscillate and create an omnidirectional wave moving radially outwards from the particle. This is called scattering and is illustrated in Fig. 2.6. The scattered waves from a particle will interfere with another particle, which will start to oscillate due to the scattered waves from the first particles. When this happens, the second particles will create scattering waves that will affect other particles, and so on.

The direct SAW radiation force, further referred to as acoustic radiation force (ARF), for rigid spheres can be divided into two, the force acting on particles in a traveling SAW field and the force acting on particles in a standing SAW field. These equations was first derived by King et al. [46] back in 1934. He derived an expression for the ARF that the particles experience in both the standing SAW field and travelling SAW field. Later research by Yosioka and Kawasima [47] further developed King's equations by taking the compressibility of the spheres into account. This yields especially for the standing SAW field. Some assumptions need to be satisfied for the equation to yield. Firstly, the host fluid in which the particles are submerged is assumed ideal, implying that the fluid is incompressible and non-viscous. Secondly, the spheres are assumed to be very small compared to the wavelength, which yields for the 7 μm particles at all targeted frequencies.

Connacher et al. [36] presenters the direct acoustic pressure derived by King et al. [46] as a force, F_{ARF}^{tr} expressed as

$$F_{ARF}^{tr} = 2\pi\rho_f A^2 \left(\frac{kr}{2}\right)^6 \left(\frac{1 + \frac{2}{9}\left(1 - \left(\frac{\rho_f}{\rho_p}\right)^2\right)}{2 + \left(\frac{\rho_f}{\rho_p}\right)^2}\right), \tag{2.6}$$

12
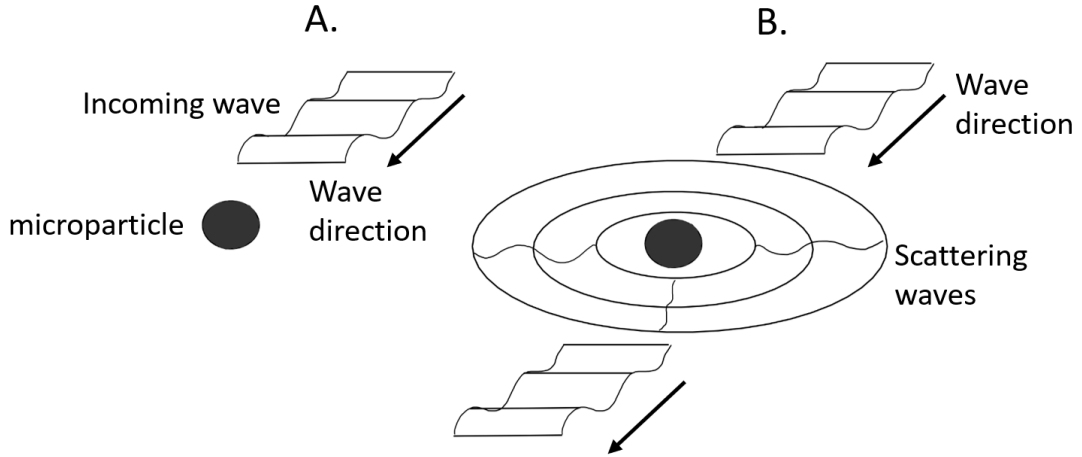
Figure 2.6: Concept of indirect acoustic radiation force referred to as scattering. When an acoustic wave interacts with a particle, the particle beginners to oscillate and then induce an omnidirectional wave field. This is known as indirect acoustic force or scattering. Subfigure A. displays the acoustic wave prior to its interaction with the particle, while subfigure B. depicts the scattering waves that are induced as a result of their interaction [23].

where A is the amplitude of the incident waves, r is the radius of the particles and $k = 2\pi f / v_r$ is the wavenumber.

Furthermore, the direct acoustic pressure in a standing SAW field was derived by Yosioka and Kawasima [47] to take into account the compressibility of the spheres. Connacher et al. [36] also present the acoustic pressure derived by Yosioka and Kawasima as a force, F_{ARF}^{st} expressed as

$$F_{ARF}^{st} = \frac{\pi p_0^2 r^3 \beta_l}{2\lambda_{SAW}} \Phi \sin(2kx), \tag{2.7}$$

where x denotes the position of the particle, p_0 present the acoustic pressure, and β_l is the compressibility of the liquid. Φ is the acoustic contrast factor expressed as

$$\Phi = \frac{5\rho_p - 2\rho_l}{2\rho_p + \rho_l} - \frac{\beta_p}{\beta_l}, \tag{2.8}$$

where β_p is the compressibility of the solid particles. The acoustic contrast factor determines whether the particles tend to be attracted towards the pressure node ($\Phi > 1$) or the antinode ($\Phi < 1$). Bellebon et al. [48] calculated a theoretical acoustic contrast factor of 0.573 for PS beads.

The drag force, F_D acting on the particles due to the fluid motion induced by the acoustic streaming can be determined by the Stokes drag equation [49]

$$F_D = 6\pi\mu r v_D. \tag{2.9}$$

v_D denotes the velocity difference between the particles and the surroundings. This force takes the surface pressure force and frictional shear force into account, and it is directed in the opposite way of the movement of the particles. Geometries that experience a flow field

will also experience a lift force, which the surface pressure force and frictional shear force in the normal direction of the flow. However, the lift force is zero for symmetrical geometries parallel to the flow direction due to the equal pressure and fictional forces acting in opposite directions. Thus, the lift is then to be neglected for a sphere.

Fluid in a circular motion will experience forced vortex motion, where the free surface of the vortex will become concave due to the centripetal acceleration [49]. Consequently, the isobars (constant pressure) within the liquid will also become concave. The hydrodynamic pressure, $P_{hydrodynamic}$, is a combination of the pressure due to centripetal acceleration and the hydrostatic pressure. This can be expressed by the formula

$$P_{hydrodynamic}(r,z) = -\rho_f g z + \frac{1}{2}\rho_f \omega^2 r^2 + P_{sur} \tag{2.10}$$

where g, ω and P_{sur} denotes the gravitational acceleration, the angular velocity of the vortex and the surrounding pressure. Note that r and z in this formula indicate positional variables, r in the radial direction and z in the upwards direction. The origo for the afore-mentioned equation is at the bottom centre of the cylinder container illustrated in Fig. 2.7.
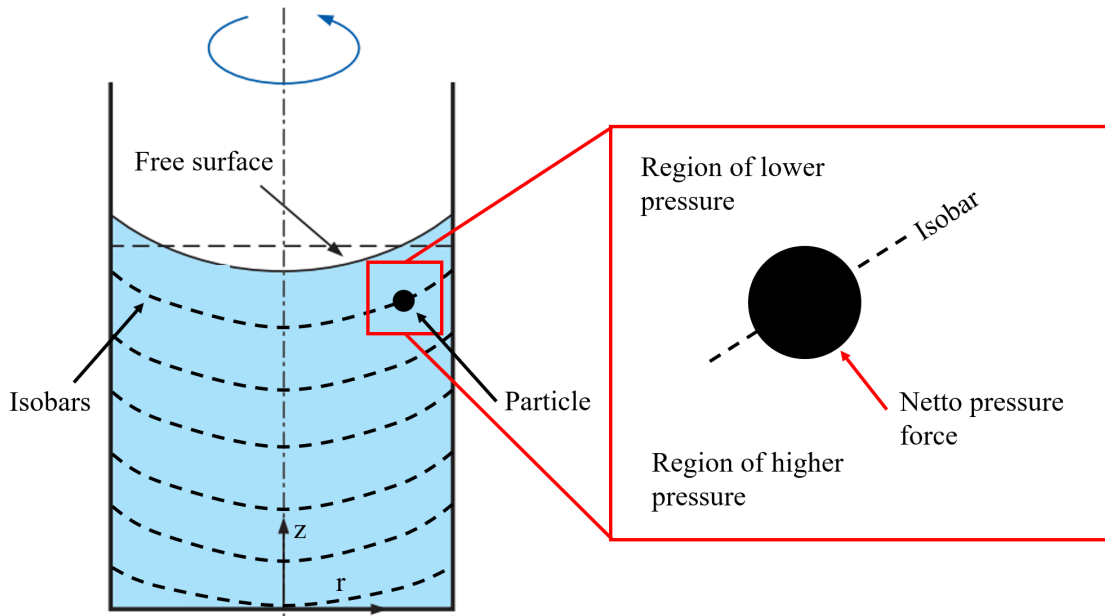
Figure 2.7: Illustration of forced vortex motion where the free surface of the liquid becomes concave due to the vortex. Consequently, the isobars (lines indicating constant pressure) become concave. A netto hydrodynamic force induced from the centripetal acceleration and the hydrostatic pressure acts radially inwards and upwards in the vortex.

A particle in the vortex region will experience a netto pressure force due to the difference in hydrodynamic pressure from each side of the isobar. The netto pressure force acts both radial inwards and upwards as illustrated in the figure.

2.5   Wettability

The introduction of surface acoustic waves into a droplet induces flow patterns within the droplet. The morphology of the droplet will have a strong impact on the resulting flow structures. A surface that exhibits a contact angle of less than 90° for a water droplet is referred to as

hydrophilic. Conversely, a surface that displays a contact angle greater than 90° is recognized as hydrophobic. Figure 2.8 illustrate the distinct differences.
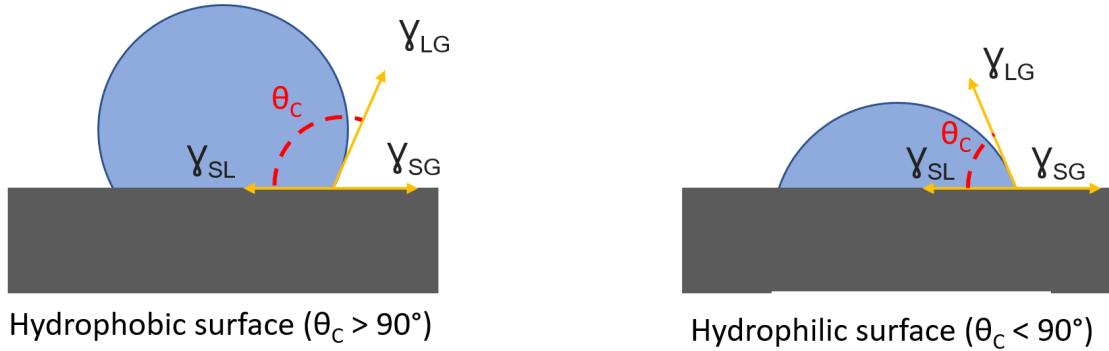
Figure 2.8: Schematic illustration between a hydrophobic surface ($\theta_C > 90°$) and a hydrophilic surface ($\theta_C < 90°$) as a function of the contact angle. γ_{LG}, γ_{SG} and γ_{SL} represent the interfacial energy along the liquid-vapour, interface of solid-vapour and solid-liquid, respectively [23].

The static contact angle, θ_C, is described by the Young equation [50] expressed by

$$\theta_C = cos^{-1}\Big(\frac{\gamma_{SG} - \gamma_{SL}}{\gamma_{LG}}\Big), \tag{2.11}$$

where γ_{LG}, γ_{SG} and γ_{SL} represent the interfacial energy along the liquid-vapour, interface of solid-vapour and solid-liquid, respectively. When a liquid comes into contact with a solid surface, the angle formed by the tangent to the liquid surface and the solid surface is known as the contact angle [49]. The droplet's shape is influenced by whether the surface is hydrophilic or hydrophobic (Fig. 2.8), resulting in a flatter or more rounded droplet, respectively. This, in turn, affects the flow structures that can be generated within the droplet. Nam et al. [51] have demonstrated that a decrease in contact angle leads to a shift in the flow pattern and consequently, the behavior of particles. Thus, it is imperative to characterize the substrate's wetting properties.

2.6   Scattering parameter

The actual energy transferred to the acoustofluidic device is typically less than the targeted input energy due to the mismatch between the input impedance and the reference impedance (50 Ω) of the SAW generator. Meaning that some of the targeted input energy is transmitted to the acoustofluidic device and some are reflected back to the SAW generator. The scattering parameter, referred to as the S-parameter, indicates the relationship between the targeted input energy and the reflected energy for a system. Meaning that only a fraction of the targeted input

energy, denoted a_1, will be transmitted into the system, while the remaining portion of the energy is reflected back, b_1. The reflected portion of the energy is given by the S-parameter S_{11}, which states the relation

$$S_{11} = \frac{b_1}{a_1}.$$

(2.12)

Table 4.1 tabulate the S-parameter and the actual energy supplied to the system.

2.7 Statistical error analysis

When conducting experiments, it is crucial to obtain physical quantities that are highly precise and accurate. However, this is not always possible, so it is essential to include the uncertainty of the measurements to determine how trustworthy and reproducible the results are. When it comes to measuring experimental results, accuracy and precision are two important factors to consider. Accuracy refers to how close the results are to the true value, while precision refers to how consistent the results are when an experiment is repeated. Figure 2.9 illustrate the combinations of accuracy and precision. Establishing accuracy can be difficult, especially in physical measurements where determining the true value is challenging. On the other hand, precision is easier to determine by conducting multiple equal experiments and calculating the standard deviation σ The standard deviation is expressed as

$$\sigma = \sqrt{\left(\frac{1}{N-1} \sum_{i=1}^{N} (x_i - \bar{x})^2 \right)},$$

(2.13)

where

$$\bar{x} = \frac{1}{N} \sum_{i=1}^{N} x_i,$$

(2.14)

is the average value, $\bar{x}$ [52]. The parameter x_i and N are the current measured value and the total number of measurements, respectively. One can format the resulting measurements as the average value plus/minus, $\pm$, the standard deviation, for example, 50s$\pm$ 5s. There are two ways to state the standard deviation; absolute uncertainty or relative uncertainty, δ. Equation 2.13 and the aforementioned example illustrate the absolute uncertainty, whereas the relative uncertainty is given by the percentage deviation from the average, i.e

$$\delta = \frac{\sigma}{\bar{x}} \cdot 100.$$

(2.15)

Throughout this thesis, absolute uncertainty will mainly be utilized. However, there are certain instances where the relative uncertainty is mentioned, so it is wise to be aware of both.
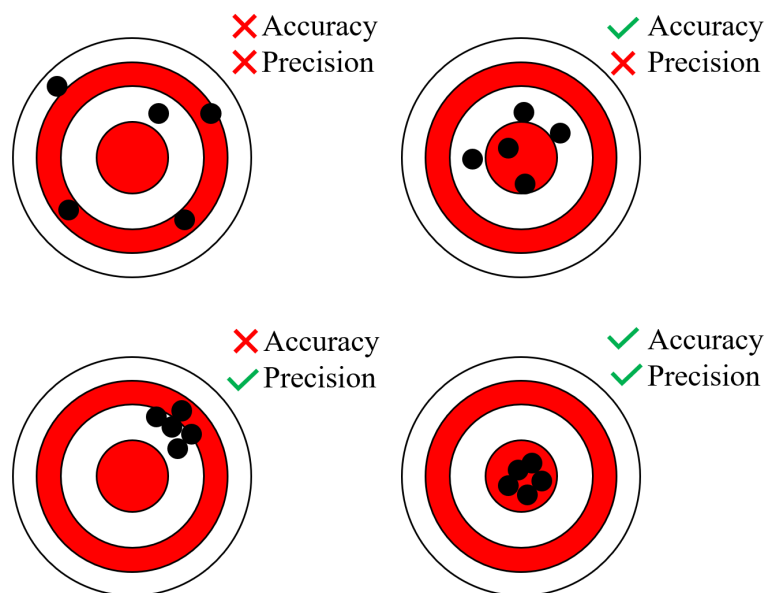
Figure 2.9: An descriptive illustration between accuracy and precision.

Chapter 3

Microfabrication procedure

This chapter is based on the work conducted for the specialisation project course TEP4541 [23] last semester. It covers the microfabrication procedure for producing spiral IDTs which is the first subtask required to achieve the objectives. Given that the design frequency is determined by the spacing of the fingers (Sec. 2.2), various spiral IDT is produced to match these frequencies. However, the same microfabrication procedure yields for every spiral IDT in this study. Only the exposed design of the fingers varies. Figure 3.1 illustrates the fabrication procedure. The production of the spiral IDT consist of positive photolithography and a subsequent step of depositing a thin film of metal. The subsequent section will chronologically describe the procedure in more detail. The recipe for the microfabrication of spiral IDT is documented in Appendix. A. The fabrication is conducted in a controlled environment, i.e., a cleanroom located in the NTNU Nanolab, to avoid any potential contamination of the samples caused by atmospheric pollution.

The microfabrication procedure presented below is based on the fabrication recipe that PhD candidate Diego Sanchez Saldaña is working with, and which has become the common recipe for the Thermal Two-Phase Flow Lab (Th2FLAB) group at NTNU. All the spiral IDT designs are constructed in AutoCAD by Diego S. Saldaña, and the microfabrication process is carried out by the author.
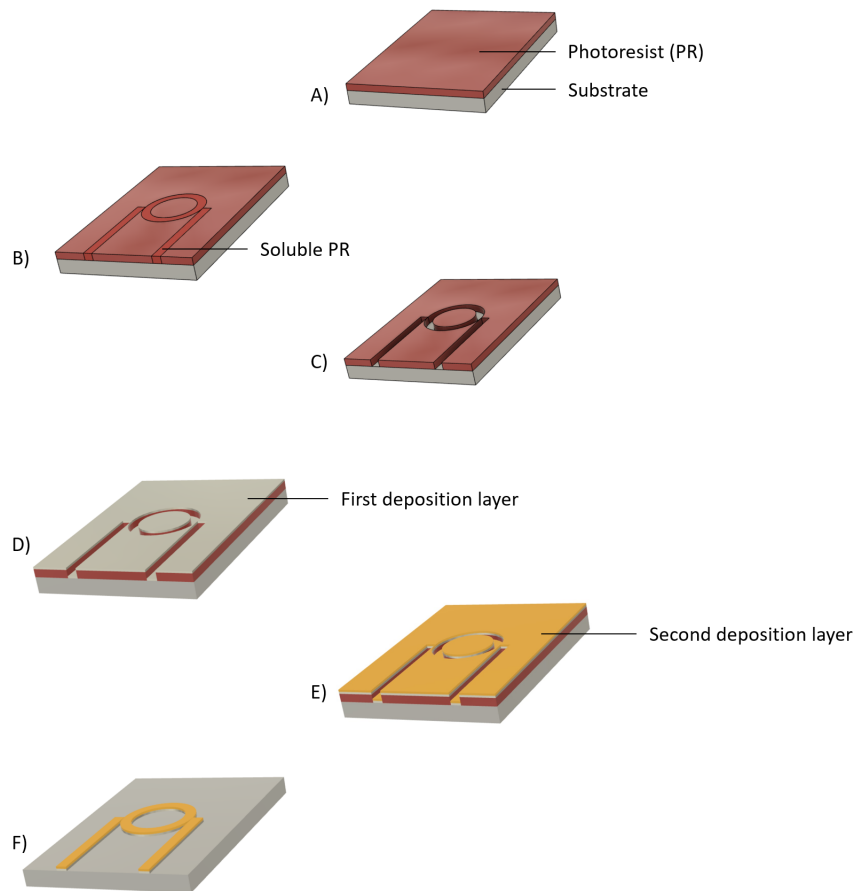
Figure 3.1: The microfabrication procedure for the production of a spiral IDT. A) A uniform layer of photoresist (PR) is deposited on top of the cleaned substrate. B) Targeted spiral regions of the photoresist are exposed to ultraviolet (UV) light in order to make these areas soluble. C) A developer facilitates the removal of the soluble photoresist. D) and E) Two thin layers of titanium and gold is the deposited through the process of thermal evaporation. F) Ultrasonic bath is responsible for the removal of the remaining photoresist, consequently leaving only the desired spiral IDT left [23].

3.1   Cleaning

The initial step in preparing the substrate is to thoroughly remove unwanted dust and residues from the surface to achieve high-precision microfabrication. The presence of undesirable particles can result in a heterogeneous surface, which can have negative effects on the fabrication process and lead to damage in certain areas of the spiral IDT. Acetone and isopropanol (IPA) are both excellent solvents that are preferred due to their ability to effectively clean the surface without causing damage to the lithium niobate (LN) substrate. Additionally, their low boiling point makes them highly desirable for use in microfabrication as they can easily evaporate.

First, acetone is utilized to eliminate unwanted impurities from the factory. However, it should be noted that acetone may leave behind residues that are difficult to remove. Therefore,

the substrate is subsequently cleaned with isopropanol (IPA) to ensure complete removal of any remaining dirt. Additionally, pure N_2 nitrogen gas facilitates an effective drying process of the sample.

3.2 Vacuum plasma cleaner

To make sure that the substrate is properly cleaned before starting the lithography process, plasma cleaning is necessary. Plasma treatment is a rapid and efficient technique for enhancing the surface characteristics of materials via the use of plasma. Plasma, which is a gas that has undergone ionization, is left with free electrons and positive ions, thereby causing the gas to be energetic and reactive [53]. When low-pressure oxygen plasma is employed, it can eliminate organic contaminants and impurities from the surface of the substrate by oxidation reactions with bombarded oxygen ions. The resultant oxidation products, namely CO_2, CO, and H_2O [54], are volatile and can be removed from the vacuum chamber. To prevent the process of recombining ions and electrons into neutral normal atoms, the plasma treatment in this project is carried out in a vacuum to avoid the cooling of the oxygen plasma by air. The appropriate parameters are essential to achieve the intended cleaning process, as incorrect parameters may lead to a separate process, such as surface activation, etching, or coating. Specifically, for cleaning purposes, the plasma cleaner operates at 50% O_2 (50 sccm) and 50% power (50W) for a duration of 5 minutes.

3.3 Dehydration bake

In order to completely remove any remaining fluid and enhance the adhesion of photoresist deposition in the subsequent step, a dehydration bake is conducted on a tempered hotplate. The sample is placed on the hotplate at a temperature of 115 °C for a duration of 5 minutes. Following the dehydration bake, it is recommended to place the sample on a tissue for cooling to reduce the risk of substrate breakage caused by rapid temperature change.

3.4 Spin coating of photoresist

In the photolithography process used to transfer the IDT design onto the LN substrate, a light-sensitive substance called photoresist (PR) is deposited onto the surface, as shown in Fig. 3.1 A). This substance contains a polymer, a solvent, and a sensitiser. When exposed to UV light, the polymer undergoes a change in structure in which the bonds break and the resist is more prone to dissolve. The solvent helps in achieving a homogeneous layer during spinning, while the sensitiser regulates the photochemical reaction [55][56]. In this study, the substance MEGAPOSIT SPR700-1.0 is utilised as the photoresist due to its low kinematic viscosity of 14.1 cSt (=mm^2/s) [57]. This property makes it relatively easy to deform.
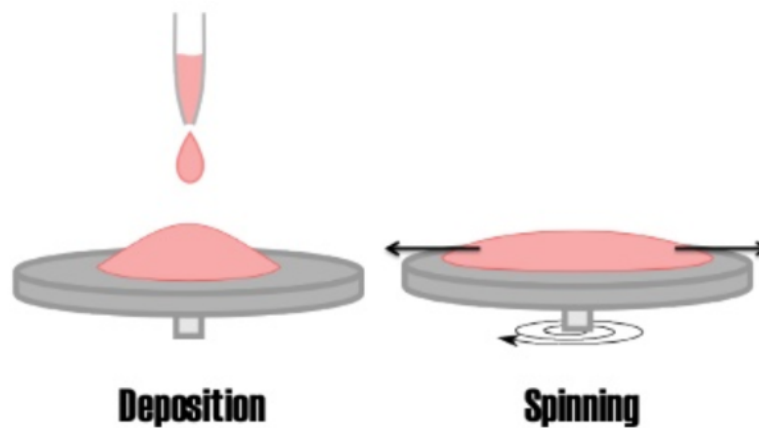
Figure 3.2: The concept of spin coating. The deposition of the photoresist at the centre of the sample initiates the process, followed by the actuation of targeted spin speed to attain a uniform thickness. The centrifugal force facilitates the expansion of the photoresist, [58].

In the field of microfabrication, the spin coater is an essential tool for obtaining a uniform layer of photoresist on a wafer. This is achieved through the use of centrifugal force, which allows for even distribution of the photoresist. The centrifugal effect of the spin coating is demonstrated in Fig. 3.2, which highlights the intention of spreading the photoresist. The purpose of this even distribution is to ensure homogenous exposure to ultraviolet (UV) light, which avoids any potential areas of unequal depths and quality. The SUSS MicroTec spin coater is used for photoresist MEGAPOSIT SPR700-1.0. Vacuum suction facilitates the stabilization of the wafer on the chuck. Initially, a low-speed rotation is initiated to facilitate the spreading of the resist material. The chuck gradually accelerates to attain the desired spin speed. The thickness of the uniform layer can be controlled by adjusting the spin speed, which is measured in rpm and can be found in Fig. 3.3. A single spin at 4000 rpm for 45 seconds with a ramp acceleration of 1000 rpm/s ensures a uniform thickness of 1 μm for the photoresist layer.

3.5 Soft baking

To ensure the solvent contained in the photoresist evaporates, it's crucial to load the sample back onto the hotplate for soft bake process. Additionally, soft baking enhances the density of the photoresist, leading to better exposure conditions. It's important to note that the sample must be clean to achieve optimal thermal transfer. Soft baking is carried out at 115°C for 1 minute. Also for this baking process, cooling down the substrate on a tissue is recommended (Sec. 3.3).
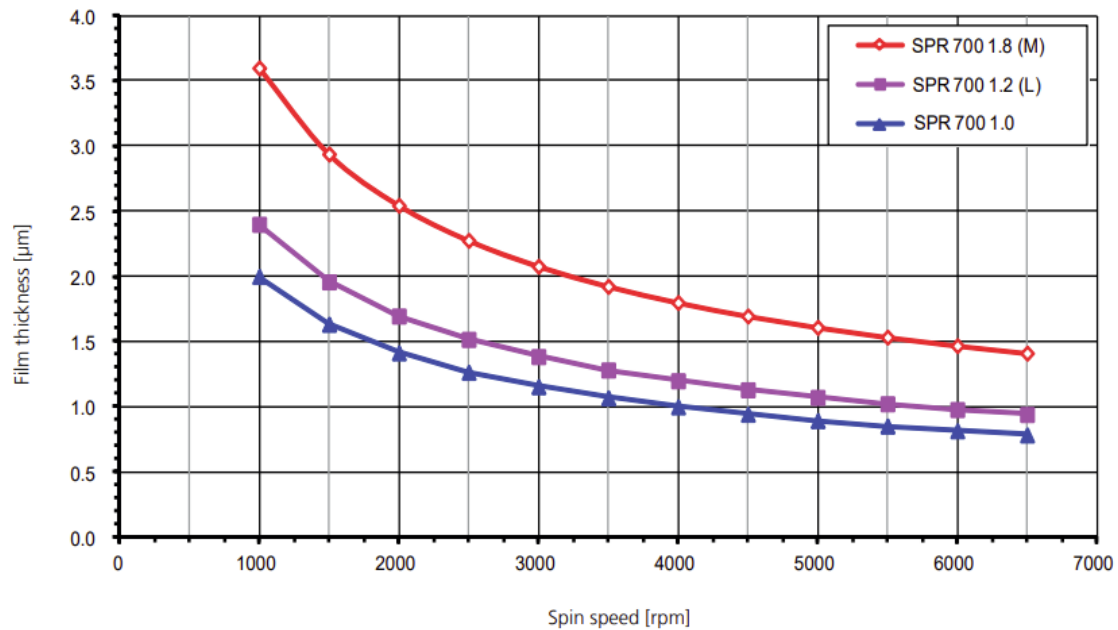
Figure 3.3: The graph displays the necessary spin speed to achieve the desired film thickness for the SPR700 photoresist series [57].

3.6   Positive exposure photolithography

The next step is to apply the desired pattern of the spiral IDT (Fig. 3.1 B)) onto the substrate by positive photolithography facilitated by the MLA150 machine. Figure 3.4 shows the Maskless Aligner MLA150 from Heidelberg Instruments used for the UV exposure of the photoresist. The MLA150 can achieve precise and effective exposure of the desired pattern. A UV light source with a wavelength of 405 nm is used for the exposure to ensures a sufficient penetration depth of the light. The maskless aligner MLA150 employs a direct-write lithography technique that eliminates the need for a mask. The machine receives a 2D drawing of the desired pattern and traces it with a laser beam on a substrate coated with photoresist. This is analogous to drawing a shape on paper with a pen, where the laser serves as the pen and the photoresist as the paper. The IDT design is drawn in AutoCAD and imported to CleWin 4, which converts it to a Crystallographic Information File (CIF) compatible with the MLA150 software. Figure 3.5 depicts the desired spiral IDT design in Clewin.

For a positive photoresist SPR 700-1.0, the irradiated regions undergo chemical changes that increase their solubility by weakening the polymer structure. Once the exposed regions of the photoresist come into contact with a developer, they dissolve. This leads to verticle profiles in the photoresist which is important to control in order to avoid an overcut vertical profile. This profile is a disadvantage for photoresist removal in the ultrasonic bath in the later step. An exposure dose of 110 mJ/cm^2 is applied to achieve a high-quality vertical profile of the irradiated regions. This parameter serves as an indicator of the amount of energy that will be applied during the process.

Figure 3.4: The Maskless Aligner MLA150 facilitates the photolithography procedure where photoresist is exposed to UV light in order to become soluble [59]

3.7   Post-exposure baking

The heat treatment utilised in the post-exposure baking process will facilitate and finalize the photoreaction that was initiated in the SPR700-1.0 photoresist during the positive exposure process. Load the sample onto the hotplate at 115 °C for 1 minute. It is recommended to cool down the sample on a tissue for the same reason stated in the dehydration process (Sec. 3.3).

3.8   Development

The development step involves removing the soluble photoresist to achieve the pattern illustrated in Fig. 3.1 C). The positive photoresist undergoes selective dissolution by the developer MF-26A, which removes the regions exposed to UV light and retains the unexposed regions. The choice of this developer is based on the compatibility with the photoresist as specified by the manufacturer and the previous results obtained by the Thermal Two-Phase Flow Lab group.

Two petri dishes are prepared for this step, one containing the MF-26A developer and one with deionized water. The sample is completely submerged in the first petri dish containing the developer for a duration of one minute, where a gentle stir is provided for the last 30 seconds. Subsequently, the sample is rinsed in the second petri dish containing deionized water. Once the sample is removed from the petri dish, it is thoroughly washed with deionized water and dried using nitrogen gas.
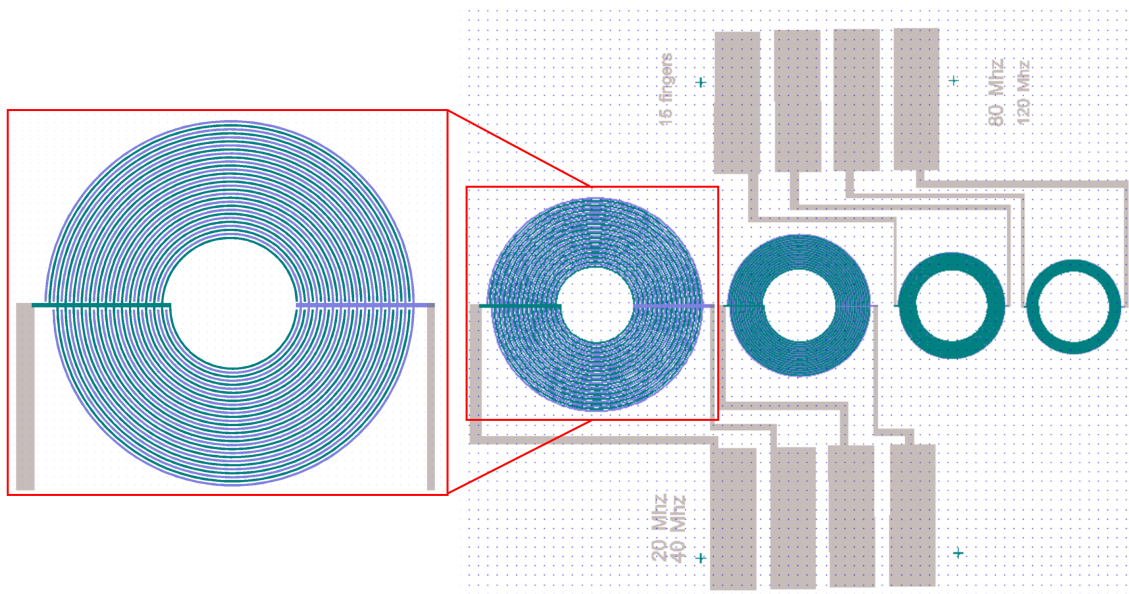
Figure 3.5: Image of the CleWin file containing the various spiral IDT designs utilized for the UV exposure performed in the MLA150 machine. Additional magnification image of the 20 MHz design showing the spiral pattern which the IDT consists of. The colour schemes differentiate the design layers.

3.9   Reflectometer

Prior to proceeding with the following fabrication steps, the quality of the current fabricated sample is measured by the use of a reflectometer. Poor fabrication features of the sample upon this point can be redoable, but proceeding with poor features through the next steps won't allow for redoing the sample. Then a new wafer has to be selected and a new fabrication process has to take place.

3.10   Thermal PVD E-beam evaporation

The next step in the microfabrication process involves depositing a thin layer of titanium (Ti) and gold (Au) to create the IDTs. Both Figure 3.1 D) and E) depict the sample following the deposition of Ti and Au, respectively. Gold is preferred for its exceptional electrical conductivity, biocompatibility, and chemical stability [60]. However, the insufficient adhesion of gold to oxide substances, such as lithium niobate, has necessitated the use of an adhesion layer. Therefore, a 10 nm thick layer of titanium is deposited between the 80 nm thick gold layer and the LN substrate. The deposition rate of titanium is 2 Å/s and 5 Å/s for gold.

Creating a uniform layer on a wafer substrate through the process of physical vapour deposition is a common technique used in microfabrication. This involves removing atoms from an evaporant material and depositing them on the substrate through energetic means. At NTNU NanoLab, the E-Beam evaporator Sputter AJA utilizes physical sputter deposition or thermal evaporation deposition for the thin film deposition method. For the fabrication of spiral IDT, only thermal evaporation is used. This method is illustrated in Fig. 3.6.

Sample ← Deposited of thin film

Vapour

Path of the
electron beam

Evaporation point

Evaporant
material

Magnetic Field
(out of the screen)

Water Cooled Holder

Filament

+

-

- +

+
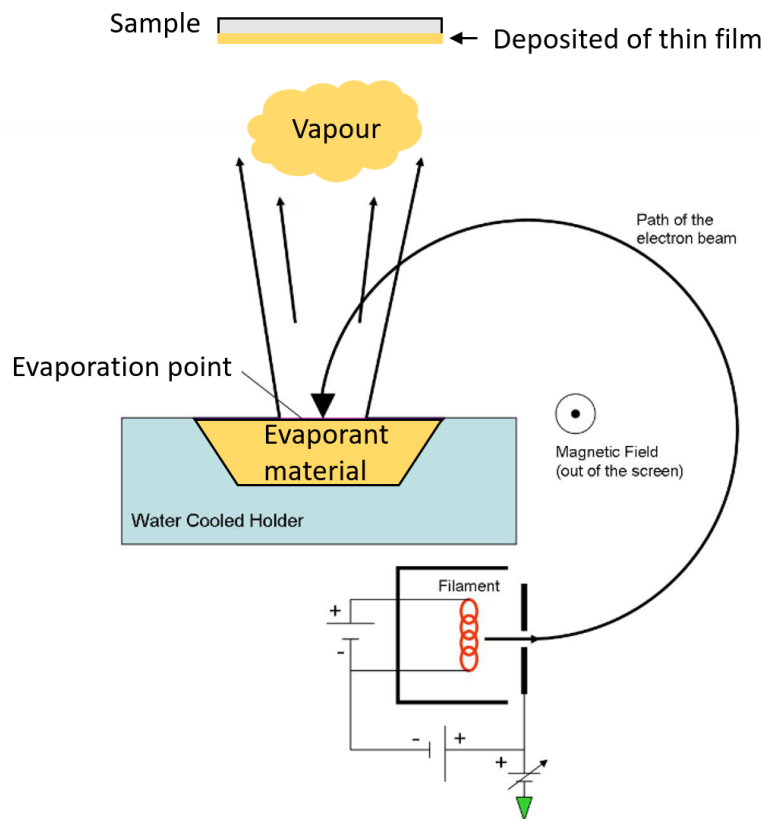
Figure 3.6: Scheme of the thermal physical vapour deposition (PVD) by means of an electrode beam. Electrons emitted from an electron beam located below the material are directed towards the surface using a magnetic field. The path of the electrons is aimed at a single point on the evaporate material, referred to as the evaporation point. This causes the material to melt and evaporate. As the vapour rises towards the low-pressure area where the sample is spinning, a layer of the desired evaporant material is deposited on top of the substrate. The water-cooled holder surrounding the evaporant material helps to keep it solidified along the edges of the material to avoid any melted spill [23].

To make sure that a substrate is evenly coated with evaporated material, a vacuum chamber is used to create low-pressure conditions. This prevents the vapour from returning down again to its source. The substrate is rotated within the chamber to ensure an even coating. Electrons emitted from an electron beam located below the material are directed towards the surface using a magnetic field. This results in an evaporation point that causes the material to melt and evaporate. As the vapour rises towards the low-pressure area where the substrate is spinning, a layer of the desired material is deposited on top of the substrate. The process is stopped once the desired thickness is achieved. It is important to maintain a low pressure of 5E-6 Torr during the process to ensure a uniform layer of deposition without any atomic collisions.

Thermal evaporation is a preferred technique for material deposition. The utilization of a single evaporation point on the targeted material helps to maintain a low temperature along the interface of the material and the water-cooled cup holder, thereby preventing any potential chemical reactions.

3.11   Ultrasonic bath

The subsequent step involves the removal of any remaining photoresist by means of an ultrasonic bath. The ultrasonic bath is a device that uses cavitation to effectively clean objects. It works by using electrical energy to create oscillation in the water tank, which generates pressure waves that produce cavitation bubbles. As these bubbles implode, shockwaves are released into the water medium in order to safely dissolve any contaminants on the submerged sample without damaging it. This method of cleaning is thorough, and the device is known for being reliable and easy to use. Additionally, it is a time-efficient way to achieve a clean result [61]. Once the SPR700-1.0 photoresist is removed, only the spiral IDT remains, as demonstrated in Fig. 3.1 F). It must be noted that the generation of cavitation bubbles during the ultrasonic bath process may cause damage to small samples. Therefore, it is preferable to confine the sample within a beaker of acetone to restrict its environment. Additionally, the beaker should be semi-submerged in a bath tank filled with water. The exertion of pressure waves on the fluid for a duration of 1 minute allows for the dissolution of SPR700-1.0. Consequently, the thin film layers of titanium and gold situated on the surface of the photoresist are also removed during this process. Any residual areas that still contain deposited layers are cleared by using tiny swabs soaked in acetone. Subsequent to this, the sample is removed and rinsed with acetone. It is then further cleaned with IPA before the remaining acetone has a chance to dry. Finally, the sample is dried off with nitrogen gas.

3.12   Saw cutting

Multiple samples are typically fabricated simultaneously on a 4-inch LN wafer, as depicted in Fig. 3.7. The aforemonetioned image shows various IDT design for various other experiments conducted by the Th2FLAB group. The centre-right square of the substrate exhibits spiral IDTs with a design frequency of 20 MHz, 40 MHz, 80 MHz and 120 MHz. The straight lines indicated where to cut the checkered substrate in order to separate all the various devices. A Disco DAD 3220 automatic dicing saw facilitated the cutting process of the LN wafer.
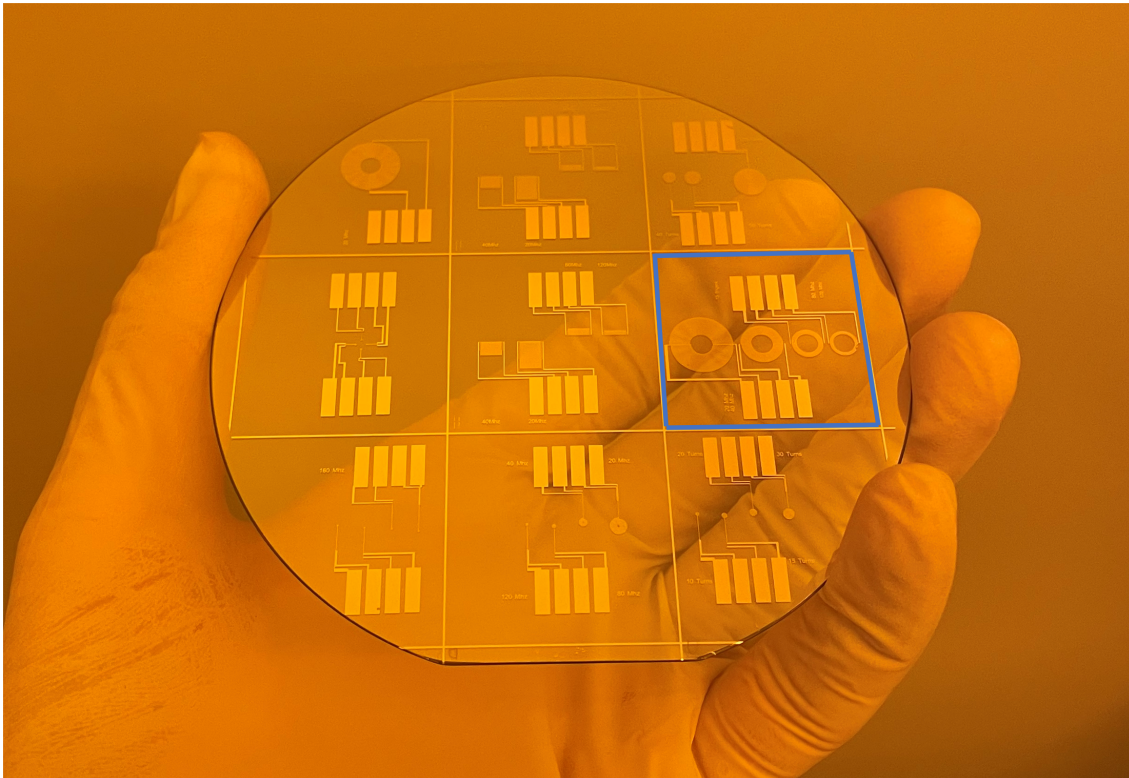
Figure 3.7: The presented image showcases a 4-inch lithium niobate wafer which has undergone the microfabrication process described above and exhibits distinct electrode designs. The final step of this process involves cutting the wafer into the respective squares marked on the wafer. The blue rectangles in the image highlight the spiral IDTs which were implemented for experiments in the thesis. These IDTs possess an identical pattern as the CleWin file shown in Figure 3.5.

Chapter 4

Experimental setup and method

This chapter presents a comprehensive description of the experimental procedure utilized for operational analysis and particle image velocimetry (PIV) analysis. The laboratory equipment, materials, and procedures are elaborated below. Furthermore, the final section highlights possible sources of error that could emerge during the experimental phase of the project. This section answers the last two subtasks regarding the visualisation of particles inside the droplet under the action of acoustic waves and examining the experimental setup. When all the subtasks are accomplished, more reliable and trustworthy results can be performed in order to answer the objectives.

The experimental setup is similar to the one used for the specialisation course TEP4541 [23] last semester. However, something is new, like the cameras and PIV measurements etc. Nevertheless, the main experimental procedure is similar. Thus, some sections are refined and extended from the project work last semester.

4.1   Description of experimental setup

A schematic setup of the experiments is illustrated in Fig. 4.1, and the facility setup is shown in Fig. 4.2 and Fig. 4.3. The inverted microscope Nikon Eclipse Ti2 allows for 2D visualisation of the droplet. An inverted microscope implies that the light source is illuminating from above, and the objective lens is located underneath the stage. The acoustofluidic device is secured onto a stage that suits the Nikon microscope to maintain its positional stability during experimentation. The stages can be manually moved in the x and y-plane by the Nikon Ti2 joystick, whereas an integrated nub on the side of the microscope is responsible for the z-movement. The droplet is deposited in the centre of the spiral IDT in the acoustofluidic device by a Hamilton syringe that is placed in a stationary syringe holder. In order to actuate surface acoustic waves (SAW) into the droplet, the acoustofluidic system is equipped with a printed circuit board (PCB) that transmits the signals into the system. The PCB is strategically posi-

tioned to maintain direct and consistent contact between its connectors and the electrodes of the IDTs. This ensures that the applied electrical signal is transferred from the PCB over to the IDTs. The PCB consist of two small cables which are responsible for transferring the electrical signals to the right ports. Additionally, the PCB is connected to a Belektroning SAW generator, which transfers the alternating electrical signal. Furthermore, the aforementioned light source can be adjusted by operating the incorporated CoolLED pE-100 white light panel. The transmitted light through the device is collected by a Nikon CFI Plan Fluor objective lens with 4x magnification. The objective lens exhibits a 17.2 mm working distance [62], allowing for complete focus through the whole sessile droplet. The transmitted light gets reflected within the microscope in order to be directed to the desired output port. The output port is connected to two cameras, an AOS PROMON U1000 Color camera for visualisation and recording of the experiment, and the Photron FASTCAM MINI UX100 high-speed camera for the particle image velocimetry (PIV) analysis.
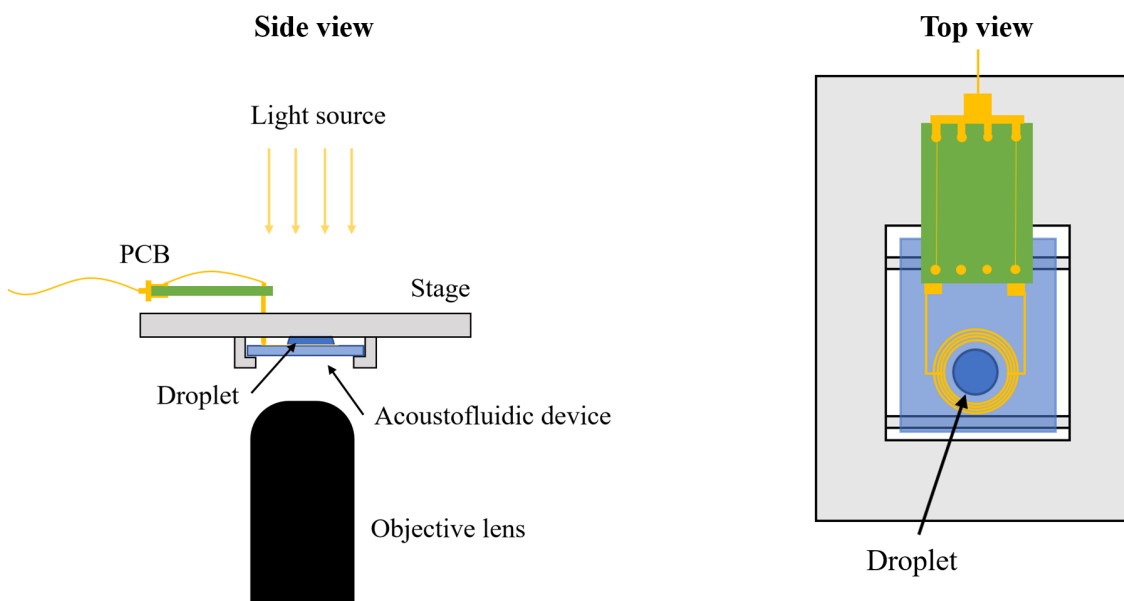
Figure 4.1: Schematic of the experimental setup seen from a side view and a top view. The light source above the stage and the objective lens underneath are responsible for visualising the experiments. The experiments are conducted on the acoustofluidic device consisting of a sessile droplet that is deposited in the centre of the spiral electrodes. The power supply is transmitted through a printed circuit board (PCB) that is connected to a SAW generator for initiating the acoustic waves.

1	**Nikon Eclipse Ti2 inverted microscope**
2	**AOS PROMON camera**
3	**CoolLED pE-100 white light source**
4	**Nikon Ti2 joystick**
5	**Belektronig SAW generator**
6	**Stage**
7	**Stationary holder for the syringe**
8	**Photron FASTCAMERA**
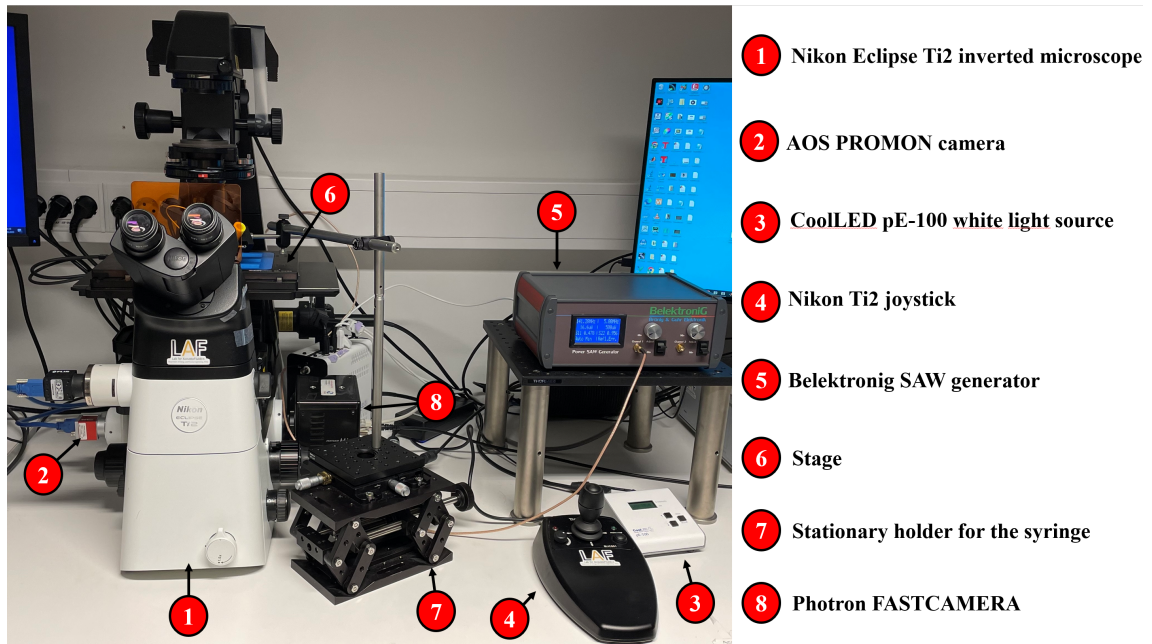
Figure 4.2: Overview of the experimental setup used. The apparatus facilitating the experiments are enumerated and explained in the image

9	**Printed circuit board (PCB)**
	Acoustofluidic device
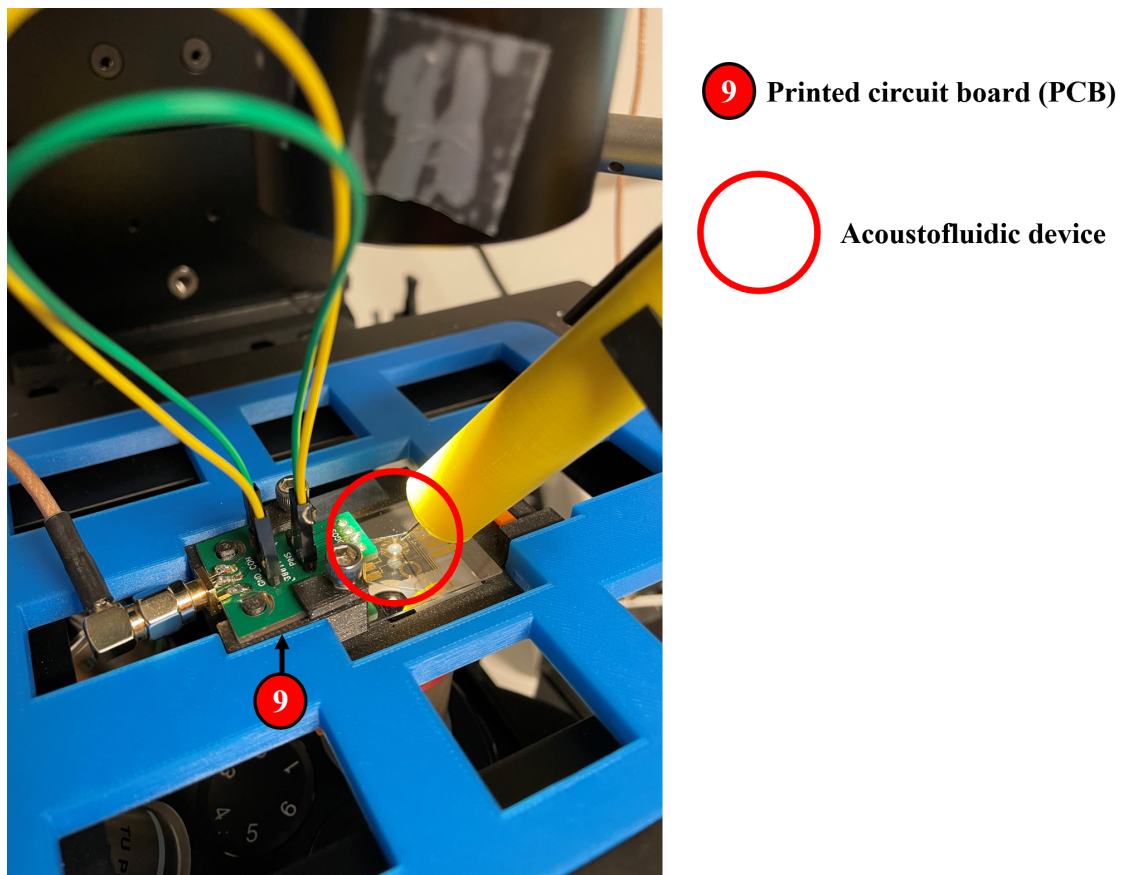
Figure 4.3: Overview of the experimental setup used. The apparatus facilitating the experiments are enumerated and explained in the image

Different light configurations were tested to ensure homogenous light distribution for better visibility of the internal process of the droplet. Based on qualitative analysis, the optimal configuration for illumination was a LED level of 10 (out of 100) and an exposure time of 5000 μs. The exposure time was chosen to be smaller than the time in between consecutive frames, but long enough for the illuminating light to visually capture the particles inside the droplet. Furthermore, to improve the spatial light distribution, three diffusers from THORLABS with various diameters (1-inch and 2-inch diameter) and grit polish (600 grit and 1500 grit) were employed (DØ10-600-MD, DG20-600-MD and DØ20-1500-MD, depicted in Fig. 4.4). Figure 4.5 compares the light distribution with and without the diffusers.

Figure 4.4: Showcase of the three THORLAB diffusers, DØ10-600-MD, DG20-600-MD and DØ20-1500-MD, which are responsible for providing homogeneous light distribution of better visualisation of the droplet and the particles within.
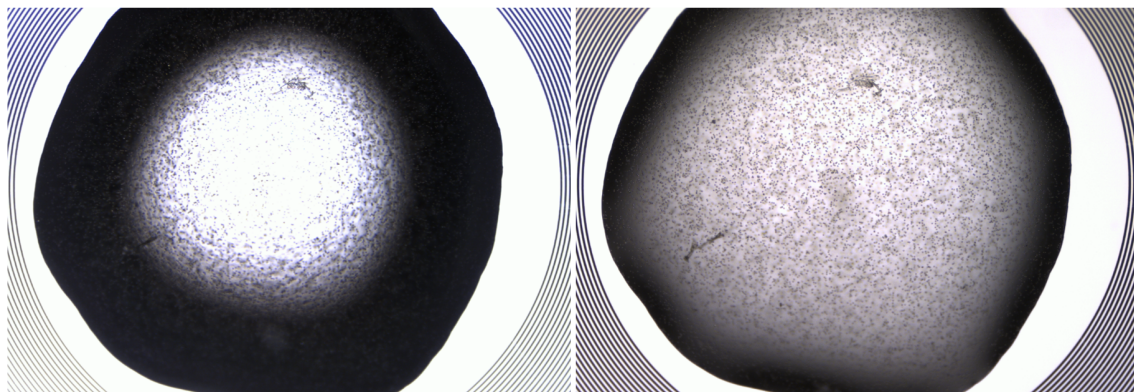
Figure 4.5: A comparison of the droplet with and without the diffusers. The left image shows how the light is transmitted through the droplet without the diffusers, whereas the right shows the refracted light through the different DØ10-600-MD, DG20-600-MD and DØ20-1500-MD in order to create the homogenous light distribution of the droplet. The darker region close to the periphery occurs due to the refraction of incoming light at the steep surface of the droplet. The surface close to the bottom exhibits a higher incline, and the light refracts with a greater angle than for the flatter region closer to the top surface of the droplet.

In order to verify that the real frame rate of the recorded videos corresponded with the acquisition one set in the software, a frame rate analysis was conducted. Previous observations

evidently showed that some frames were dropped while recording the experiments, meaning that the camera wasn't able to capture the experiments in the targeted acquisition frame rate. Measurements were taken to solve the issue, and a frame rate analysis was conducted to verify that the real frame rate of the recording corresponded with the targeted acquisition frame rate. To verify this, videos for various lengths were recorded at the same frame rate of 125 fps. The same recording settings used for the main experiments were used in this analysis, and the duration of the various recordings was fixed. By obtaining the total amount of recorded frames and dividing it by the duration of each video, the frame rate was calculated to be 125 fps. Consequently, verifying that the acquisition frame rate corresponded with the real one. Some reasons for unequal frame rates are provided by Basler Product Documentation [63].

4.1.1 Acoustofluidic device and operational analysis

An acoustofluidic device exhibits two different frequencies, a design frequency and an operational frequency. The patterned electrodes determine the design frequency, and the wave generator determines the operational frequency. Figure 4.6 depicts the fabricated spiral IDTs for the various design frequencies. The largest one corresponds to the 20 MHz design frequency, where the width of the electrode bar is 50 μm given by Eq. 2.1. The equation states the relation $f \propto d^{-1}$, implying that higher frequencies exhibit a narrower width of the IDT. That is why the smallest spiral IDT corresponds to the highest design frequency of 120 MHz, where the width of the IDT is 8.3 μm. The 40 MHz and 80 MHz IDT exhibit a width of 24 μm and 12.5 μm, respectively.

The inner circle diameter of the spiral IDTs was measured to be 3.2 mm at 20 MHz, 3.1 mm at 40 MHz and 80 MHz, and 3.0 mm at 120 MHz. Additionally, all devices had a spiral IDT with a turn count of 15 electrodes to improve the quality factor and reduce energy loss per oscillation of the wave, as described in Sec. 2.3. While the fabrication quality of the 20 MHz, 40 MHz, and 80 MHz spiral IDTs were sufficient, some portions of the 120 MHz spiral IDT exhibited deficient patterning. Subsequently, a new, identical spiral IDT was fabricated for the 120 MHz case and utilized in the experiments.

When the operational frequency performs at the respective design frequency, more of the targeted input power is transferred into the acoustofluidic system. For this reason, the typical procedure is to fabricate different electrode designs for experimenting with different frequencies as shown in Fig. 4.6. However, it was found that it is possible to operate the system on a different frequency than what it is designed for. Therefore, the thesis distinguishes between a multi-system and a single-system. The multi-system implies that each spiral IDT in Fig. 4.6 operates at a frequency that is equal to the design frequency. Meaning that the large spiral IDT on the left side which is designed at 20 MHz given the fabricated width of the IDTs, will operate at 20 MHz during the experiments. The same yields for the other spiral IDTs. However, this is not the case for the single-system. Thus, the single-system utilizes the 80 MHz fixed spiral IDT (the third spiral IDT from the left in the aforementioned figure) for the design frequency but performs experiments at various operational frequencies.

The single-system would be particularly advantageous in bio-sensors, as the desired aggregation pattern could be obtained from a single device by adjusting the operating frequency and input power, eliminating the necessity of fabricating various devices for each frequency.

The experimental procedure involved diluting 7 μm polystyrene Polybead supplied by Bangs Laboratories in deionized water. Subsequently, the concentration of microsphere particles
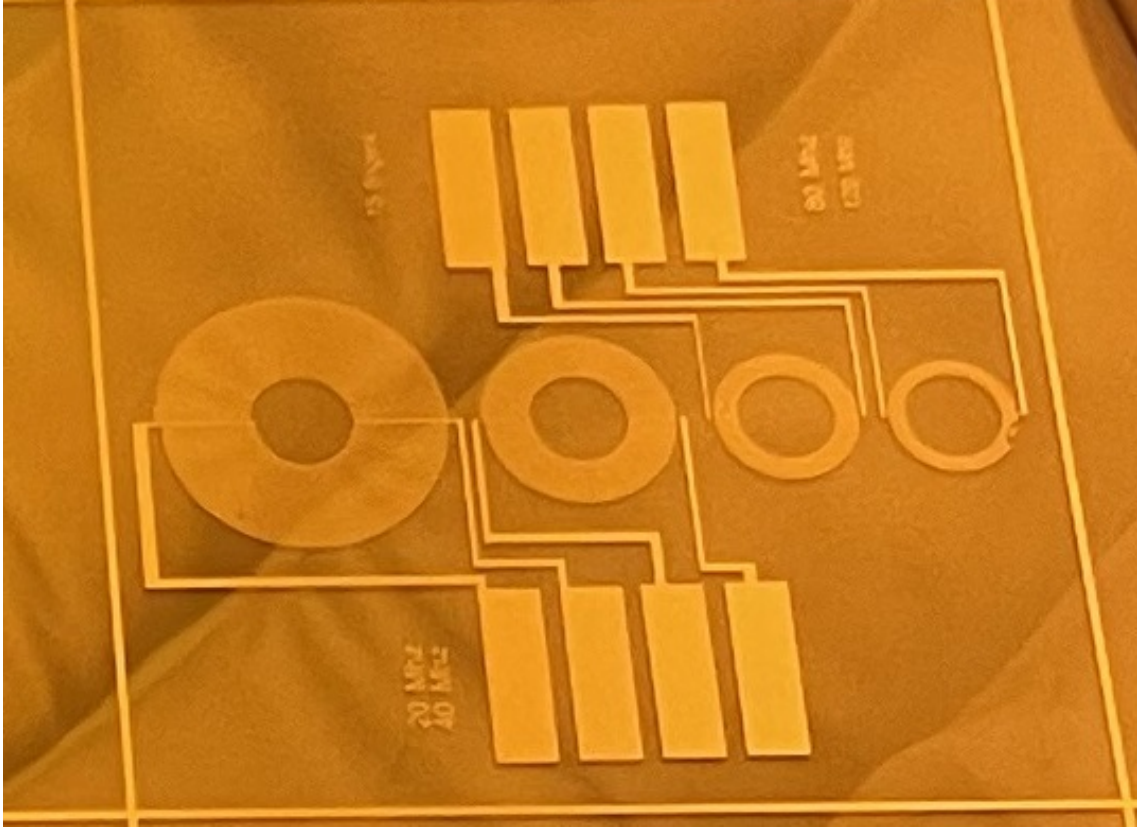
Figure 4.6: The image presents the fabricated spiral IDT utilized for the experiments conducted. The larger one to the left is the 20 MHz, given its wider IDTs expressed by Eq. 2.1. As the width of the IDT decreases, the frequency increases. This results in a corresponding increase in design frequency towards the right side of the images, where the width of the IDT becomes smaller. Therefore, following to the right of the 20 MHz spiral IDT is the 40 MHz, then the 80 MHz and all the way to the right is the 120 MHz spiral IDT.

per volume mixture, denoted by C, was computed using the prescribed equations from Bangs Laboratories [64]

$$C = \frac{6 \cdot 10^{10} \cdot \rho_L}{\pi \cdot \rho_p \cdot D^3} \cdot \frac{1}{1+m}. \tag{4.1}$$

The weight percentage of solids is represented by S, while D denotes the mean diameter. The density of the solid sphere is indicated by ρ_p, and m denotes the proportion of liquid water. Additionally, the density of the microsphere suspension, ρ_L, is expressed as

$$\rho_L = \frac{100 \cdot \rho_p}{S(1 - \rho_p) + (100 \cdot \rho_p)}. \tag{4.2}$$

When microspheres are deposited into water, their density is very similar to that of the water. In fact, the microspheres have a density of 1.06 g/mL, while water has a density of 1.00 g/mL. This close density relation allows the microspheres to slow down and distribute themselves evenly within the droplet. To extract the solution of microparticles, a Hamilton microliter syringe is used, which has the ability to withdraw up to 5 μL of liquid with a high

level of precision. In fact, it can measure liquid amounts with a resolution of 0.05 μL and a step of 0.5 μL [65].

In order to prevent the occurrence of double vision caused by the refraction of incoming light, a plane transparent piece of a lithium niobate wafer is carefully positioned between the objective lens and the acoustofluidic device, as depicted in Figure 4.7. The orientation of this additional piece of lithium niobate is critical, and various rotations have been experimentally evaluated to determine the most suitable position. It is important to note that the careful placement of this piece is a necessary step in ensuring accurate and reliable results in acoustofluidic experiments.
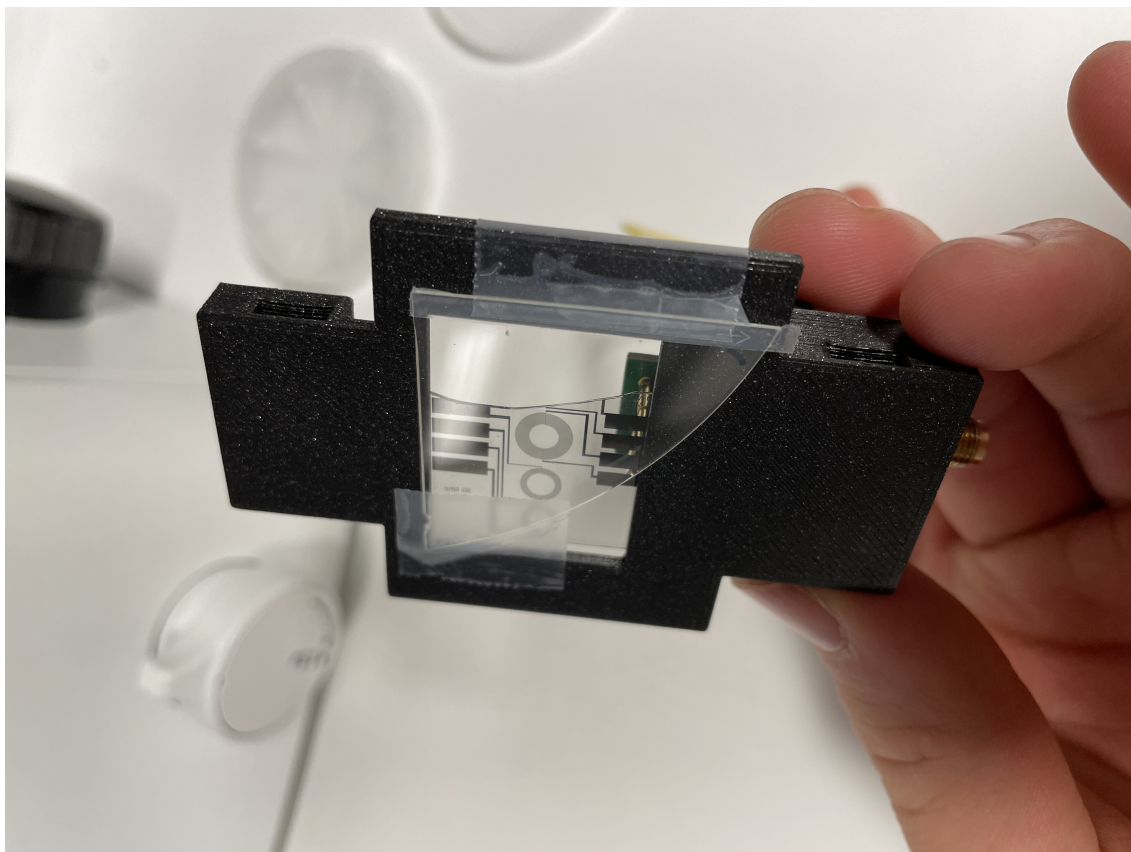
Figure 4.7: To avoid double vision, an additional piece of lithium niobate is attached to the back of the acoustofluidic device to refract the transmitted light back onto its original path after it has already been refracted by the device's own lithium niobate.

Initial contact analysis

In order to achieve consistent experimental results, an initial analysis of the contact angle was conducted. The purpose of this analysis was to examine the consistency of the initial contact angle, thereby reducing uncertainty in aggregation time and lifetime resulting from variations in droplet conditions. The optical tensiometer OneAttension supplied by Biolin Scientific, depicted in Fig. 4.8, was utilized to accurately measure the surface wetting characteristics,. The static initial contact angle of the droplet was measured using the Young equation (Eq. 2.11). It is crucial to consider the distance between the droplet and the camera when calculating the static contact angle. To attain precise results, the tensiometer was calibrated by adjusting the

stage and lens position to focus on a needle with a diameter of 0.8 mm. The resulting measured initial contact angle is given further down in Sec. 4.2.3.
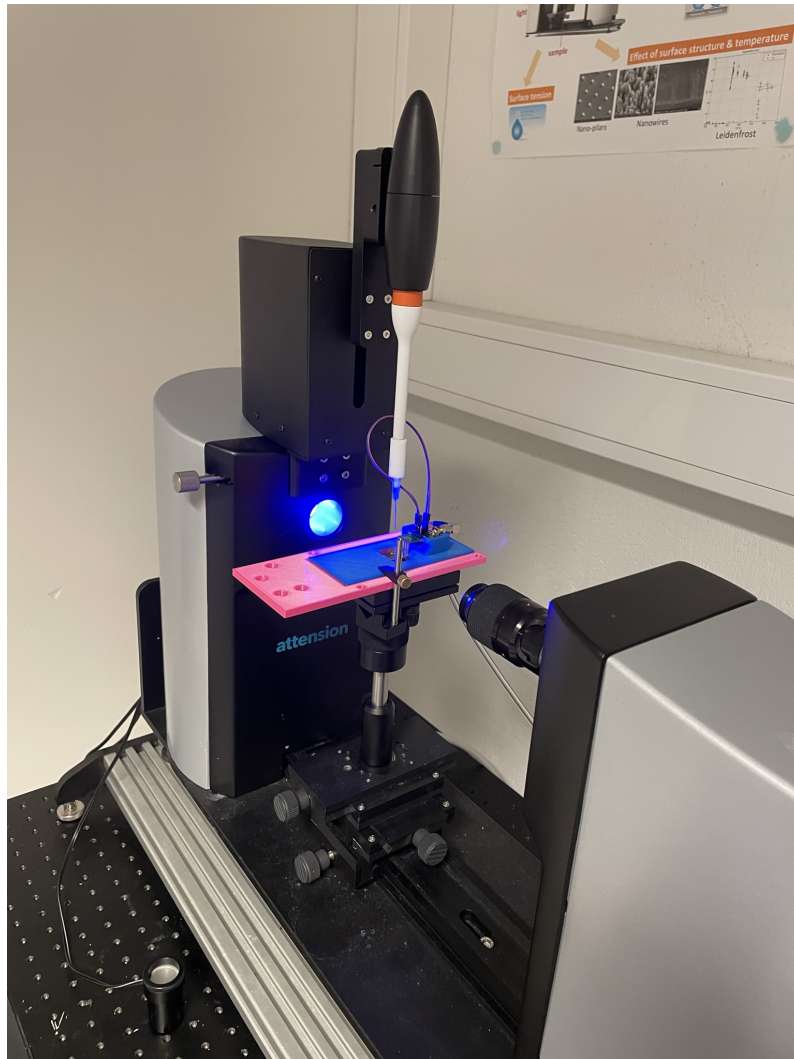
Figure 4.8: Image of the OneAttention tensiometer utilised in the initial contact analysis of the sessile droplet. The acoustofluidic device is positioned in front of the camera and a droplet was deposited onto the device.

4.1.2   Particle Image Velocimetry (PIV) analysis

Particle Image Velocimetry (PIV), is an technique that is commonly utilized to measure fluid flow, such as the velocity field or the vorticity field. This method involves analyzing the movement of particles that are suspended within the fluid, using high-speed cameras to capture a sequence of images, and processing the data to extract valuable insights about fluid flow patterns. As mentioned previously, the Photron high-speed camera facilitates the recordings for particle image velocimetry (PIV) measurements due to its ability to perform high frame rate videos. There exist a variety of PIV methods today for different flows and applications. The flow field for experiments conducted in this thesis is calculated by examining the movements of the particles between two consecutive frames of the recorded videos. This means that no laser or strobe is used for these measurements, which is contrary to traditional PIV techniques

[66]. The PIV measurements are performed using the PIVlab extension created by William Thielicke in MATLAB$^{®}$ [67]. The operational procedure of this software is further discussed in the next subsection, Sec. 4.2.2.

Criteria for accurate PIV measurements

In order to conduct accurate and reliable PIV measurements, various factors must be taken into account. Firstly, it is important to obtain a homogeneous seeding of particles inside the liquid. This is accomplished by mixing the particles in the solution before each experiment [68]. Given that the particles are more uniformly distributed in the first seconds after the actuation of the SAW, the PIV recordings are done in this time period. Hence, the videos satisfy this first criterion. Secondly, it is important that the illumination is uniform. This is done by implementing three diffusers for greater spatial light distribution. Thirdly, the ITTC [69] mentioned that the study by Prasad et al. [70] concluded that particles should display a diameter between 2-4 pixels in order to reduce undesirable effects on particle recognition. Figure 4.9 illustrates that the 7 μm PS particles used in this work are indeed between this diameter range. Fourthly, the interrogation window should be determined such that at least 6-8 particles are present in each interrogation window [71]. Figure 4.10 shows a magnification of a 32x32 pixel interrogation window for different frames with a desired particle volume concentration of 1:5. Counting the number of particles in the interrogation window shows that the fourth criterion is satisfied. The last criterion says the maximum displacement of a particle between two consecutive frames should be approximately 25% of the interrogation window. Keane et al. [72] established this criterion as mentioned by the ITTC [69]. That corresponds to a displacement of 8 pixels per frame for the case of a 32x32 pixels interrogation window. A framerate of 500 fps was tested, and an image sequence of 10 frames was analysed in the region of the highest particle velocity. The analysis of those ten images showed an average displacement of 2.5 pixels per frame. Meaning that a frame rate of 500 fps is sufficient for PIV analysis. All video processing in order to quantify and satisfy the criteria is done in the software (PFV4) supplied by Photron Limited.
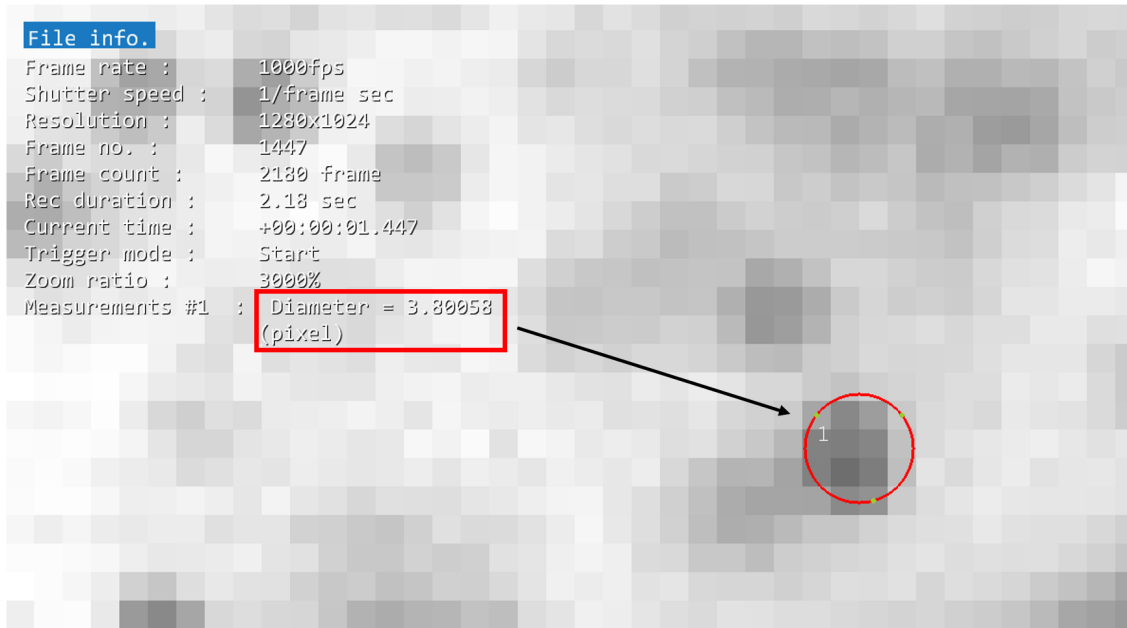
Figure 4.9: Measurement of 7 μm particles was conducted in the PFV4 software in order to verify that the pixel diameter satisfied the third criterion for accurate PIV analysis regarding the use of particles with a pixel diameter between 2 μm and 4 μm. The pixel diameter is shown to be 3.8 pixels, hence satisfying the third criterion.
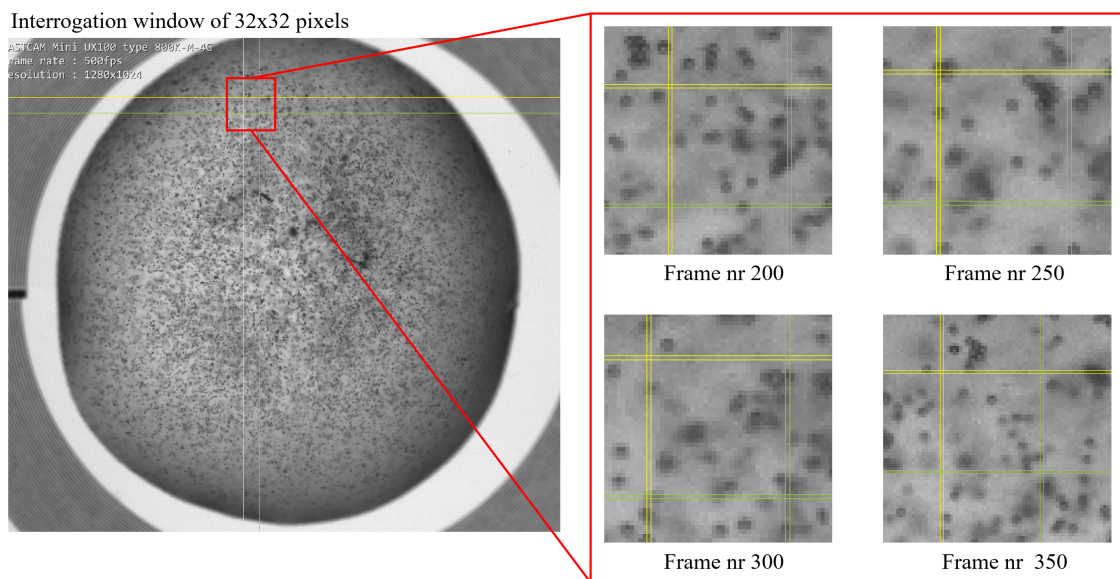
Figure 4.10: A magnification of the flow field showing a 32x32 pixel square that contains at least 6-8 pixels at four random timeframes, hence indicating that the fourth criterion for accurate PIV measurement is satisfied. PFV4 facilitated the analysis regarding the size of the interrogation window.

The PIV criteria suggest that a frame rate of 500 fps is sufficient. However, preliminary testing at 1000 fps was conducted to compare the accuracy between those frame rates. Note that separate experiments were performed due to the impossibility of recording the fast cluster

aggregation at two frame rates. The frame sequence for PIV analysis is taken after the first second of SAW actuation and with a duration of 0.1 seconds. Figure 4.11 depicts the histogram for both frame rates. Additionally, manual measurements were conducted in the PFV4 software to verify that the velocity measurements provided by the PIV analysis were of the correct magnitude. Both histograms showed to yield the same order of magnitude as the manual measurement. The histogram from the 1000 fps frame rate displayed a greater tendency to form a single peak around the manually calculated average velocity. Additionally, the peak width of the 1000 fps histogram was close to the manually measured standard deviation. A small width indicates a lower standard deviation of the measurements. Consequently, it was concluded that PIV recordings should be conducted at a frame rate of 1000 fps for optimal accuracy.
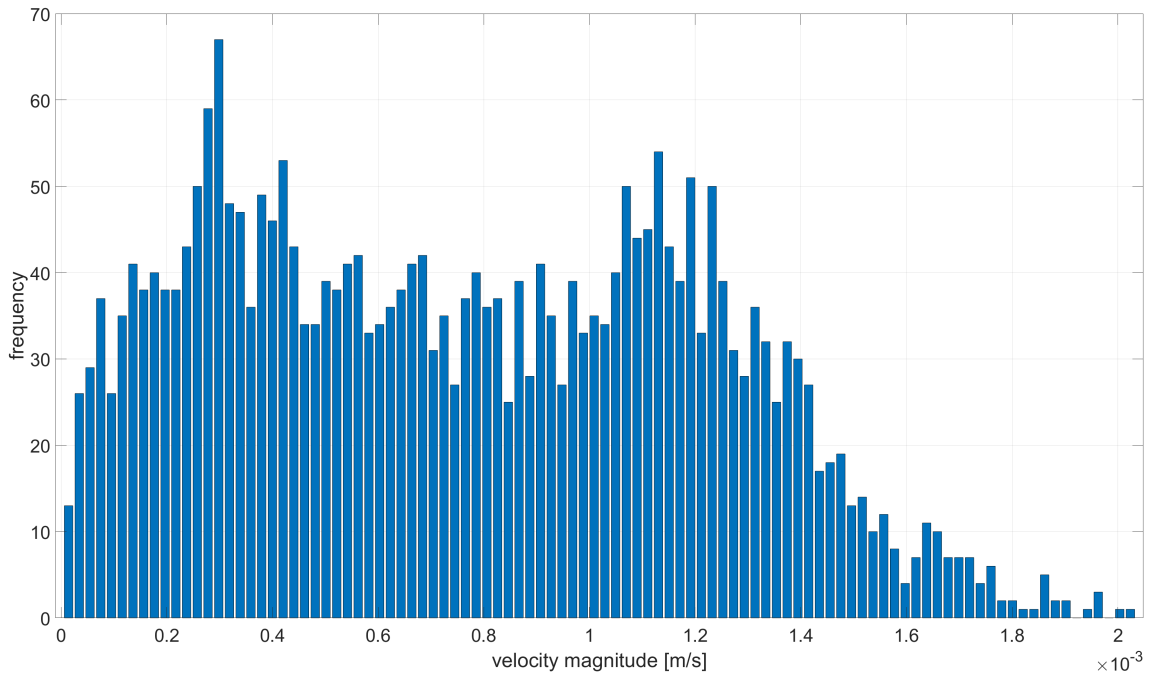
(a) Velocity data obtained through PIV analysis were used to generate a histogram at a frame rate of 500 fps.
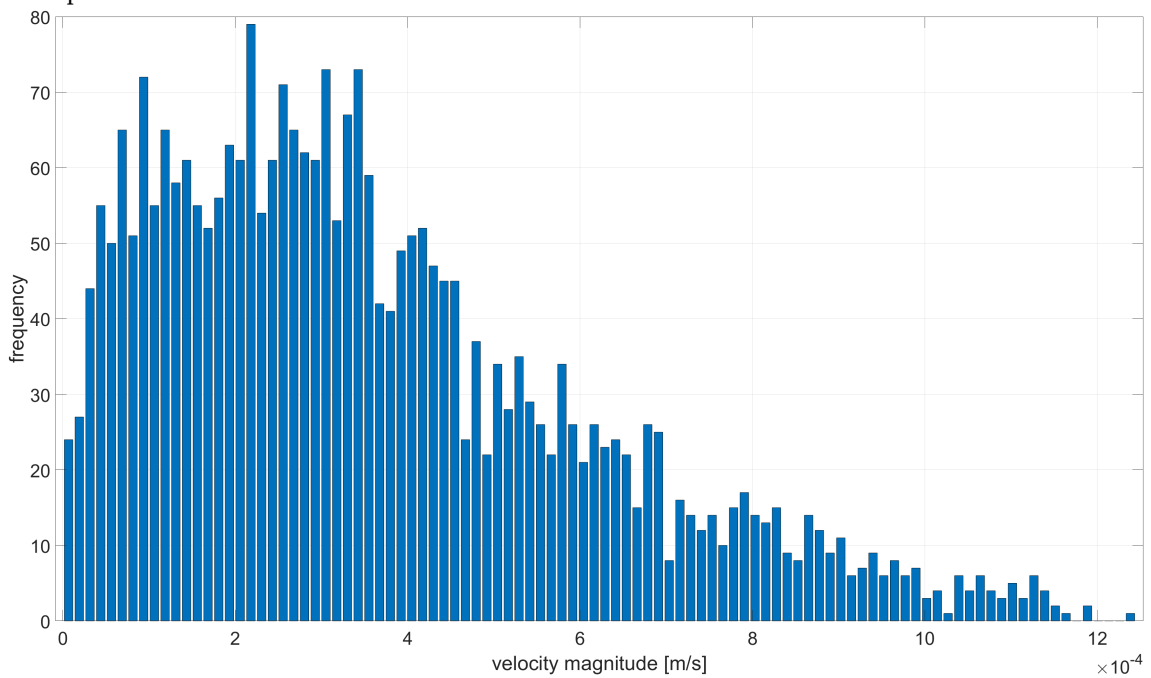
(b) Velocity data obtained through PIV analysis were used to generate a histogram at a frame rate of 1000 fps.

Figure 4.11: Comparing histograms of the particle velocity for a frame rate of (a) 500 fps and (b) 1000 fps.

4.2 Experimental method

To ensure consistent outcomes, it is crucial to provide a clear explanation of the methodology used for conducting the analyses. Therefore, this section outlines the procedure for the experiments, PIV analysis and initial contact angle analysis.

4.2.1 Operational procedure

The experimental setup involves placing the acoustofluidic device onto a stage, which is subsequently placed within an inverted Nikon Eclipse Ti2 microscope for visualizing the behaviour of particles. To obtain a concentration of microspheres per mL mixture of $5.26 \cdot 10^7$ determined by Eq. 4.1, a ratio of suspensions containing Polybead and deionized water is kept at a volume ratio of 1:5. Homogeneous dilution of microparticles in the mixture was facilitated using a vortex mixer. Subsequently, 2 μL of the mixed solution was extracted by a Hamilton syringe and loaded into the fixed syringe holder for precise and accurate deposition of the droplet in the centre of the spiral IDT. A marker in the software upon depositing served as a guide for consistent droplet placement. Three diffusers were placed between the light source and the droplet to ensure homogeneous light distribution. The shutter was fully opened, and the light intensity was adjusted to 10. The AOS PROMON camera recorded the experiments at a resolution of 1984x1264, using a timed exposure mode of 5,000 μs and a frame rate of 125 fps, which was set in the AOS Imaging Studio 4 software.

Upon deposition of the droplet onto the acoustofluidic device, a timer was initiated with a targeted time of 10 seconds to initiate the recording and activate the SAW generator. During this brief pause, the power input is recorded, and the fixed syringe holder is removed. Once the target time limit is reached, 100 mW of input power is initiated into the system. After the experiments, the acoustofluidic device is cleaned of any residues. First with 70% ethanol, then with IPA. Cleaning the sample will affect the surface energy of the piezoelectric material, hence influencing the initial contact angle of the droplet. Therefore, the cleaning procedure is crucial for obtaining consistent and reproducible results for each experiment.

MATLAB$^®$ facilitates the post-processing of the recorded videos in order to extract the relevant data that is presented in the Result and Discussion chapter. The scripts are written by the author himself.

4.2.2 Operatinal procedure for PIV measurements

The operational procedure for PIV analysis was similar to the aforementioned experimental procedure. The main difference in the experimental setup was a decrease in the light intensity, down to 6.6, and the change of camera. The Photron FASTCAM MINI recorded the experiments at a resolution of 1280x1024 and a frame rate of 1000 fps. Another experimental difference was that PIV analysis was only done for the higher frequency range of 80 MHz and 120 MHz. It was mainly two reasons for this. Firstly, the majority of the particles at lower frequencies were located at the bottom of the droplet, hence partly blocking the field of view of particles higher up in the droplet where the hydrodynamics occurred. This blockage made it hard to conduct PIV measurements since the calculations depended on the visible displacement of the particles. Secondly, PIV analysis was mainly used to discover the particle behaviour of cluster formation that occurred at higher frequencies. The recorded videos were then exported into PIVlab for further processing. Figure 4.12 shows an example of the average velocity magnitude field obtained form the PIV analysis.
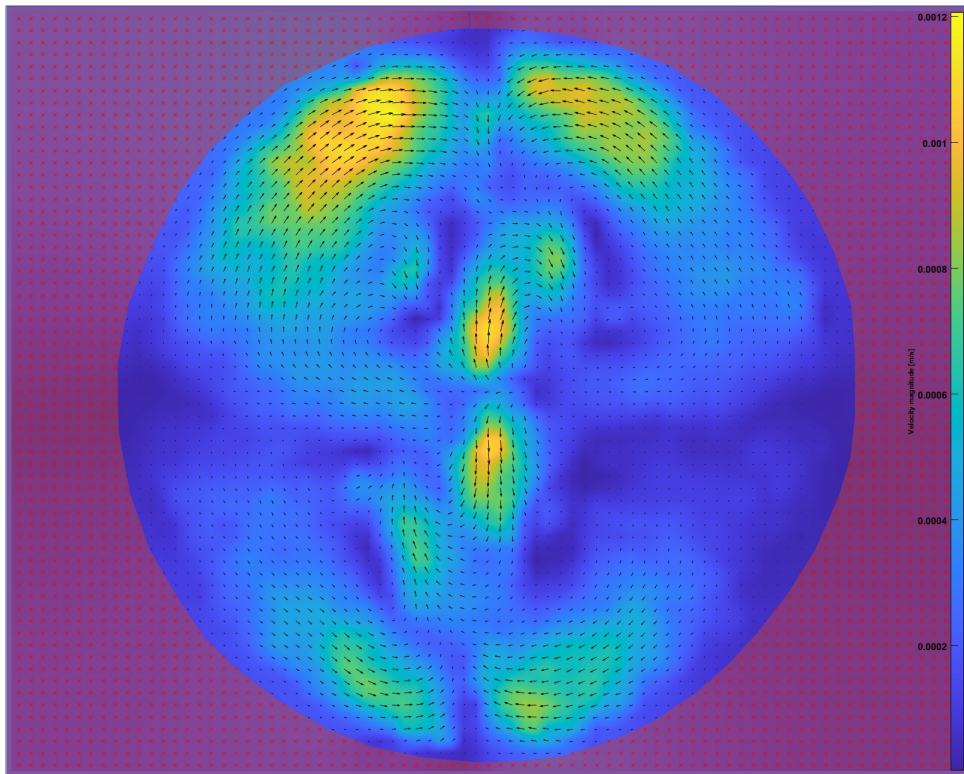
Figure 4.12: Velocity magnitude field obtained by PIVlab.

PIVlab

Figure 4.13 shows the masked region of interest (ROI) around the droplet that was to be analysed. The PIV analysis is based on the fast Fourier Transform (FFT) window deformation algorithm, which was the fasted and most advanced algorithm implemented in PIVlab, hence also recommended by the developer William Thielicke. A progressive three-pass interrogation window was chosen, where the window size decreased from a coarse size of 128x128 pixels to 64x64 pixels and then, finally, the finest size of 32x32 pixels. This was for capturing any large displacements in the flow field [73]. For precise estimation of geometrical quantities on a sub-pixel level, a Gauss 2x3-point function was utilized [74]. The correlation robustness was set to the recommended standard mode. A 500 μm calibration grid supplied by THORLABS facilitated the conversion of quantities from px/frame to m/s. Furthermore, post-processing was necessary to exclude large deviations in the velocities. This was accomplished by refining the velocity limits calculated by the aforementioned PIV settings, as shown in Fig. 4.14.
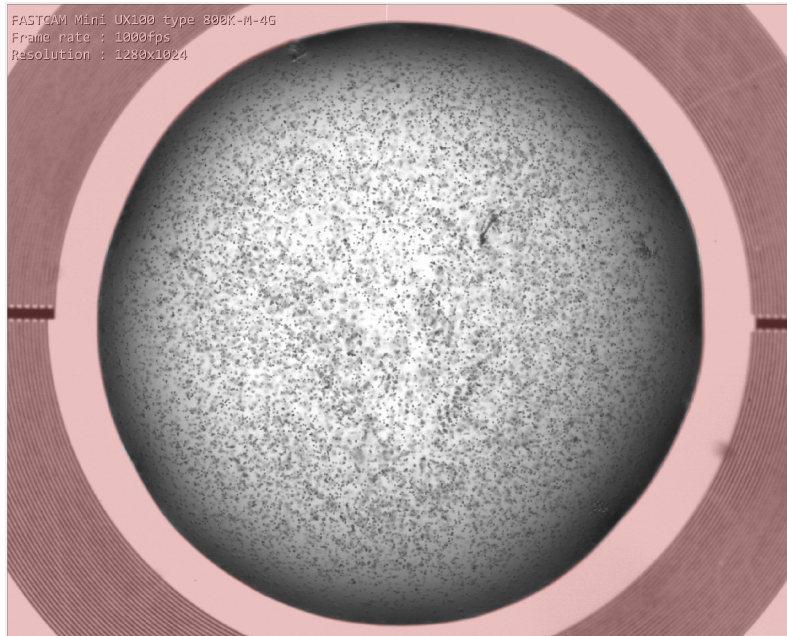
Figure 4.13: Region of interest (ROI) is the droplet, hence only this region will be analysed by PIVlab.
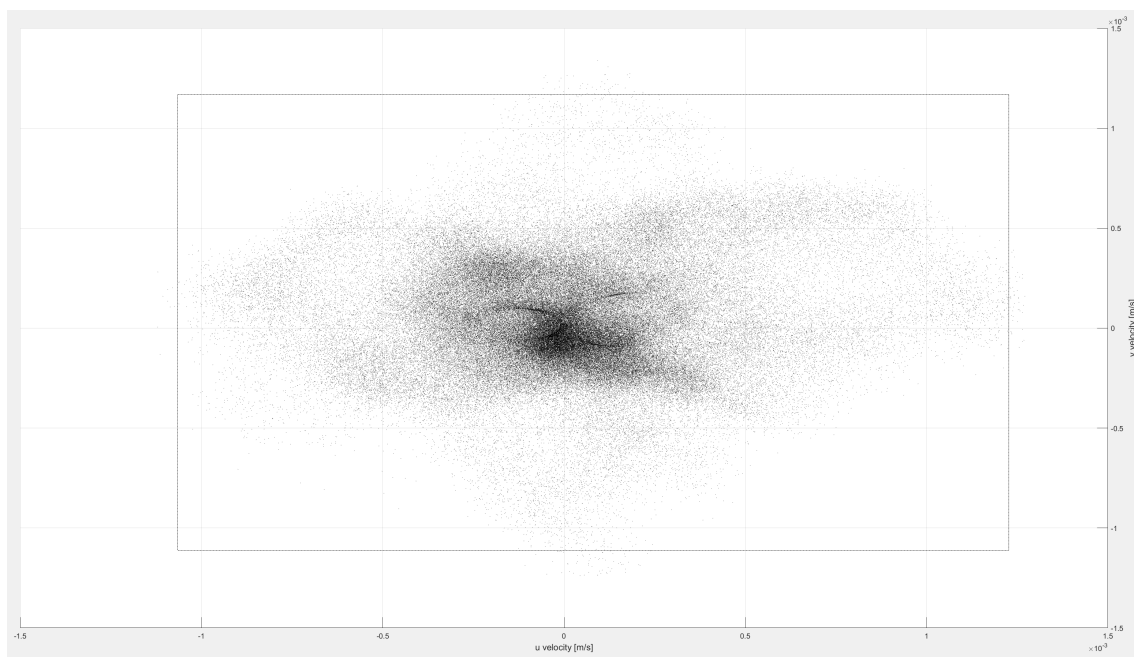
Figure 4.14: Post-processing step in PIVlab includes refining the velocity limits, thereby excluding unrealistically high velocities measured by the software. The scattered point indicates the measured velocity components in the x- and y-directions.

4.2.3   Initial contact angle analysis

An analysis was conducted to determine the initial contact angle and the influence of the deposition angle of the syringe. Multiple tests were conducted, indicating that the initial contact

angle remained consistent at $42° \pm 1°$. Interestingly, the different angles did not have an impact on droplet deposition. For resemble purposes between the initial contact angle analysis and the main experiments, disinfection and IPA cleaning were performed on the sample between each experiment. It is important to note that the SAW was not connected during the initial contact analysis, as it does not affect the contact angle in the instantaneous time when the droplet is deposited. Prior to testing, calibration of the optical tensiometer was performed.

4.3   Possible sources of error

To ensure the reliability and validity of experimental findings, it is important to address potential sources of error. Such sources are typically categorized into two types of inaccuracies, namely measurement inaccuracy (noise) and sensor inaccuracy (bias). While the latter is typically provided by the supplier, the former can be calculated through the use of equations such as Eq. 2.13, 2.14, and 2.15, and is more reliant on experimental procedures. A number of potential sources of error, including both bias and noise inaccuracies, are listed below.

Firstly, the microsphere particles are subject to geometrical uncertainty, as the supplier provides spheres with a diameter of 7.32 μm $\pm$ 0.53 μm, which deviates slightly from the targeted diameter of 7 μm [45]. However, with this small variation in particle geometry, any deviations in the forces acting upon the particles is likely to be negligible.

Secondly, the provided input power from the SAW generator deviates from the targeted one. The targeted input power is 100 mW, however, it deviates. This is because the power is determined by the applied dB, and then converted to mW. So tuning the dB might not always correspond exactly with the targeted input power of 100 mW. Furthermore, only a portion of the input powers is actually transmitted into the system. The rest is either lost or reflected back. The S-parameter indicates how much has been reflected and how much has been absorbed into the system. Table 4.1 shows the input power, S-parameter and the real power supply to the multi-system at various frequencies.

Table 4.1: The table displays the input power settings for different frequencies, along with the corresponding S-parameter that represents energy loss in the system. Although energy and power are two separate quantities, they both suffer from this loss, resulting in a fraction of the power being transmitted into the system. Therefore, also the real supplied power is provided.

Frequency [MHz]	Input power [mW]	S-parameter [-]	Real power supplied to the system [mW]
20	99 ± 1	0.086 ± 0.003	90 ± 1
40	101 ± 1	0.016 ± 0.002	100 ± 1
80	98 ± 1	0.152 ± 0.002	83 ± 1
120	103 ± 3	0.394 ± 0.004	62 ± 2

Thirdly, if the droplet deposition deviates from the targeted location in the centre of the spiral IDT, it can result in varied behaviour during the aggregation process. This is because omnidirectional acoustic waves will enter the droplet unevenly, which will lead to uneven force distribution of the particles. However, the behaviour of the particles doesn't deviate much

between the experiments for small dislocations of the droplet. Still, droplets that are deposited far from the centre are cleaned away.

Fourthly, deviation in the initial contact angle will lead to various flow phenomena, as evidently observed by other researchers in the Th2FLAB group and reported by Nam et al. [51]. Therefore, an initial contact angle analysis was conducted as described above. How much deviation in the initial contact angle is necessary to change the flow is unknown. However, the same aggregation pattern occurred for the main experiments in this thesis, hence, the variation in initial contact angle seems to have little influence on the conducted experiments.

Lastly, the extracted volume of 2 μL with the Hamilton syringe will also provide uncertainty since the measured extraction is done by qualitative means. The precise resolution and step of the syringe described in Sec. 4.1.1 assist the accuracy of the extraction to a certain degree, so the deviation from the targeted volume of 2 μL is assumed to be minimal. This is also reflected in the experiments, where the same aggregation pattern occurs. Therefore, this uncertainty is assumed to be neglectable.

Chapter 5

Results and discussions

In this chapter, the results obtained from the investigation on the influence of frequency on the aggregation pattern of dispersed microparticles within a water droplet for both the multi-system and single-system are presented and analyzed. The results can be divided into two parts, where each part attempt to address the objectives stated.

The first part investigates the particle aggregation for the targeted frequencies facilitated by the traditional multi-system where both operational frequency and design frequency are equal, hence referred to as a single "frequency" in this part. The first part covers the first three sections, namely "Temporal evolution of the aggregation pattern", "Concentric particle trapping", and "Cluster aggregation". The two first objectives are looked into as a characterisation of the aggregation pattern is carried out, and a qualitative examination of the influential hydrodynamic effects and the radiative forces acting on the particles are discussed to gain a better understanding of the aggregation mechanism.

The second part aims to explore the aggregation pattern obtained for the single-system device. The final section of this chapter, "Single-system 80 MHz acoustofluidic device", is devoted to this investigation. An analysis of the particle aggregation behaviour is conducted and compared to the multi-system, hence completing the third objective set for this thesis. Furthermore, the last objective is addressed by conducting an investigation of the aggregation regimes corresponding to various operational frequencies and input powers to further explore the potential of the single-system. A qualitative examination of the influential hydrodynamic effects and radiative forces acting on the obtained aggregation pattern is discussed, consequently answering the mentioned second objective for the single-system. Finally, a recommendation of the most optimal single-system configuration of operation frequency and input power for producing the most effective and optimal concentric particle trapping and cluster formation is presented and compared to the same aggregation pattern for the multi-system.

5.1 Temporal evolution of the aggregation pattern

The two first objectives are examined by a qualitative analysis of the particle behaviour for the multis-system. The performed study characterises the temporal evolution of the aggregation pattern and discusses the conversion between the dominant hydrodynamic effects and the radiation effect for various frequencies.

Figure 5.1 shows the temporal evolution of 7 μm polystyrene particles dispersed in a 2 μL droplet under the action of surface acoustic waves for different operational frequencies, 20 MHz, 40 MHz, 80 MHz and 120 MHz. An input power of 100 mW was chosen based on previous experiments conducted in the specialisation course TEP4541 [23] that showed promising cluster formation and stability for the high frequency of 120 MHz.
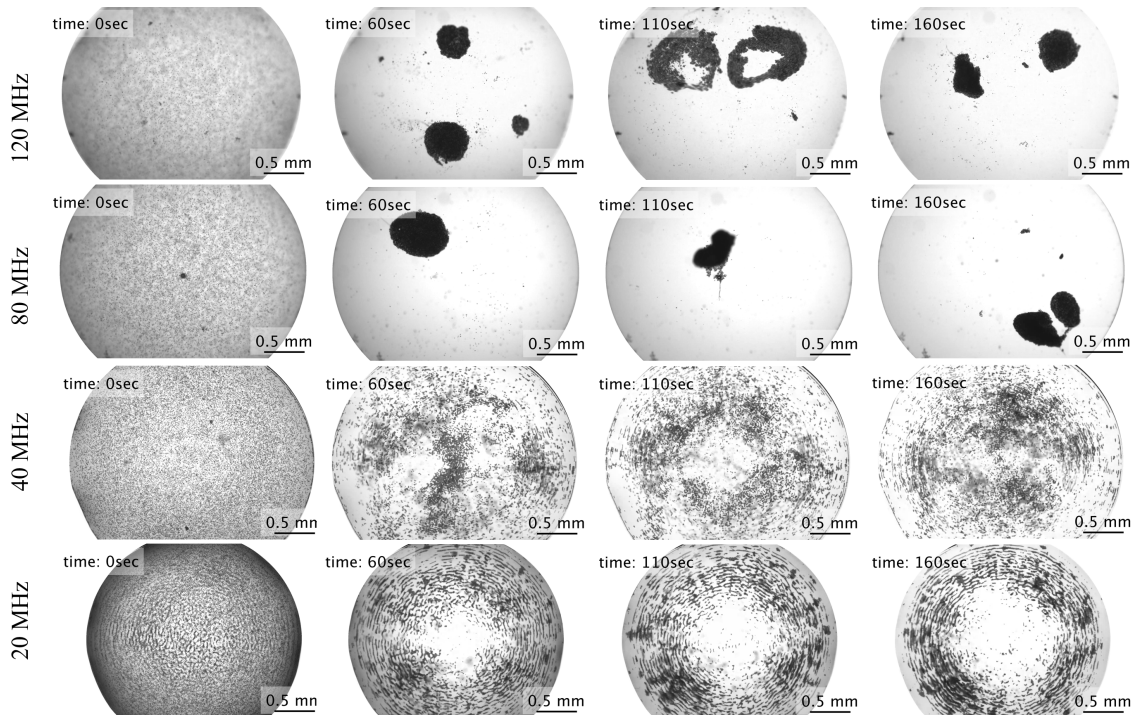
Figure 5.1: Temporal evolution of 7 μm PS particles at the frequencies of 20 MHz, 40 MHz, 80 MHz and 120 MHz at a fixed input power of 100 mW. Higher frequencies tend to form cluster aggregations, whereas lower frequencies tend to entrap the majority of the particles in 2D concentric rings at the bottom of the 2 μL droplet. The cluster formation at higher frequencies disperses and reassemble multiple time within the lifetime of the droplet. On the contrary, the trapped particles at the lower frequencies are stationary and do not fluctuate.

The main observation from the temporal evolution reveales that higher frequencies tend to form particle clusters, while lower frequencies result in the trapping of the particles. The hydrodynamic at high frequencies causes vortices in the flow field, which the particles tend to accumulate towards, hence establishing cluster formations. During the early stages, the former frequency showed the tendency of 80 MHz to form a single cluster and 120 MHz to form multi-clusters. As the process progressed, 80 MHz also appeared to form a multi-cluster, although the main cluster formation was that of a single one. Both frequencies provided clusters with a reasonable degree of temporal stability, implying that the cluster formation stayed united over a period of time. However, over time, the clusters began to disperse. At 120 MHz, the clusters

disintegrated and formed two larger rings in the upper region of the droplet, as can be observed in Fig. 5.1, which eventually collapsed into two clusters once again. Even three clusters were observed for some of the experiments, where one of them typically was significantly smaller than the others. For 80 MHz frequency, the single cluster in the early temporal stage tended to be reformed into a tornado structure. The tornado is a three-dimensional phenomenon where the particles form a cylindrical rotating assembly from the bottom to the top of the droplet. This tornado tended to collapse into a single cluster or two clusters after a while. This shift in formation can appear multiple times during the lifetime of the droplet. Although, when the droplet evaporates and shrinks, it becomes less space for the three-dimensional phenomena to occur. Consequently, the tornado becomes a cluster aggregation in the late temporal stage of its lifetime.

The clusters were observed to be located on the top periphery of the sessile droplet, which is advantageous for the extraction of the cluster. Extraction at this location minimizes interference with the inside flow field because less penetration of the droplet is required. By reducing the disturbance in the flow, the risk of breaking the aggregated clusters due to a shift in the hydrodynamic is reduced. Maintaining the integrity of the cluster during the extraction process might be of benefit for external examination of the particle assembly. This examination is outside the scope of this thesis, nevertheless, it is worth mentioning.

Upon examining the droplet subjected to 20 MHz and 40 MHz frequencies, it was observed that particles had been captured in a concentric ring formation located at the base of the droplet. Despite a few particles moving along with the flow, the majority remained trapped at the bottom. The trapping process began at the initiation of the SAW and persisted throughout the lifespan of the droplet. While circular rings were visible at both frequencies, their consistency was more pronounced at 20 MHz.

Visual observations of experiments at low-range frequencies showed that the trapped particles at the bottom exhibited small vibrations. One reason for this is the scattering effect from the particles. The incoming acoustic waves induce an oscillating motion on the particles, which in turn creates omnidirectional scattering waves from each particle, as illustrated in Fig. 2.6. The omnidirectional scattering waves will propagate in the liquid and interfere with other particles, which will induce a vibrating motion and create new scattering waves. This is not seen for the particles moving in the flow field since the scattering effect is negligible compared to the hydrodynamic. Another reason for the vibrating motion that occurs for the trapped particles is due to oscillations of the liquid close to the solid-liquid interface that are induced by oscillations in the surface of the lithium niobate substrate. When the liquid oscillates, the 7 μm particles within it follow the oscillating motion.

Figure 5.1 shows how the aggregation behaviour emerges from the conversion of forces that arises between low and high frequencies. At lower frequencies, the acoustic radiation force induces pressure waves along the bottom surface that dominates this region. The particles that are located in the acoustic pressure field will experience a pressure gradient that will influence their behaviour. When opposite waves interact with each other, a standing SAW field establishes, as illustrated in Fig. 2.2b. This will create pressure nodes, referred to as trapping wells. The pressure gradient acting on the particles pushes the particles to the well and traps them there. Thus, the main effect of trapping particles at the bottom is the acoustic radiation force. Since this force is more dominant than the hydrodynamic for lower frequencies, concentric rings are formed in this range. Conversely, at higher frequencies, the induced drag force by

the acoustic streaming and the centripetal force becomes more significant, leading to the formation of stronger vortex regions capable of compressing particles into clusters. That is not to say that the acoustic radiation force is not present at high frequencies. In fact, the acoustic radiation force will increase for higher frequencies. This is shown from the acoustic radiation force equations, Eq. 2.6 and Eq. 2.7, which both are dependent on the frequency, either through the wavenumber or through the wavelength. In fact, the acoustic radiation force for travelling waves increases exponentially by a factor of six for increasing frequencies. Neither the drag force nor the centripetal force is a function of the frequency; rather, they are a function of the velocities in the flow. The surprising observation is that an increase in frequency leads to an exponential increase in acoustic radiation force which is responsible for particle tapping, yet, very little to no trapping of particles at the bottom occurs at higher frequencies.

As previously discussed, two significant patterns have been observed in particle aggregation, namely cluster aggregation and particle trapping. These patterns have been noted to occur at different frequencies, with cluster aggregation being observed at higher frequencies and particle trapping at lower frequencies. The following sections investigate further the characteristics of the observed behaviour and provide an in-depth discussion of the findings. By doing so, it is possible to identify the unique features that distinguish them from each other and gain a better understanding of the mechanisms that drives them.

5.2   Concentric particle trapping

The study of concentric particle trapping aims to gain a deeper insight into the pattern obtained for various frequencies. Examining and characterising the 2D concentric pattern of particles on the bottom of the droplet will provide a greater understanding of the mechanisms acting inside the sessile droplet.

Experimental analysis of the temporal evolution revealed that droplets subjected to the low frequency of 20 MHz and 40 MHz exhibited 2D particle trapping, as mentioned in the previous section. Figure 5.2 depicts the temporal evolution of submerged 7 μm PS microspheres in a 2 μL sessile droplet at frequency 20 MHz and input power 100 mW at initial timestep and after 120 seconds. These timesteps illustrate how the uniformly distributed particles evolve both spatially and temporally at the bottom of the droplet.

Figure 5.3 shows the spatial and temporal evolution of the particles for 40 MHz at the initial timestep and after 20 seconds for an input power of 100 mW. The increase in frequency results in a stronger hydrodynamic effect within the droplet, indicating a potential shift from the dominant acoustic radiation force to hydrodynamic effects. Besides, the attenuation length is reduced, and a weaker standing SAW field is established due to less interference of opposite waves. These factors result in stronger hydrodynamic effects in the droplet, hence increasing the potential of releasing entrapped particles from the standing wave field. In turn, this leads to fewer particles being trapped at the bottom and a higher number of particles in the flow field compared to the 20 MHz configuration.

The phenomena of particle trapping for low frequencies and cluster formation at high frequencies can be explained by the attenuation length along the solid-liquid interface, represented by α^{-1} and illustrated in Fig.2.5. The attenuation length along this interface is inversely

Temporal evolution of 20 MHz
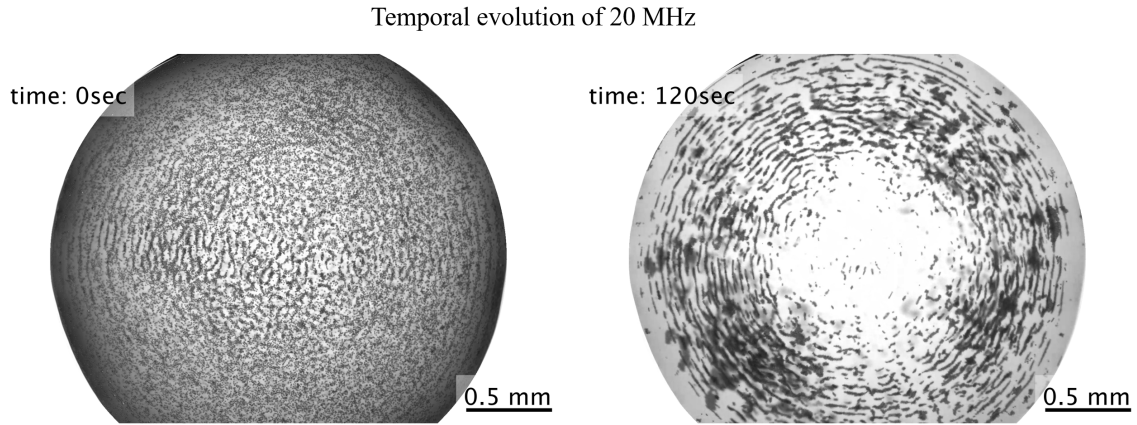
Figure 5.2: Temporal and spatial evolution of the 7 μm particles from the initial timestep to a time of 120 seconds at a frequency of 20 MHz. When the SAW is actuated, the acoustic wave field is capable of producing thick concentric rings of entrapped particles.

Temporal evolution of 40 MHz
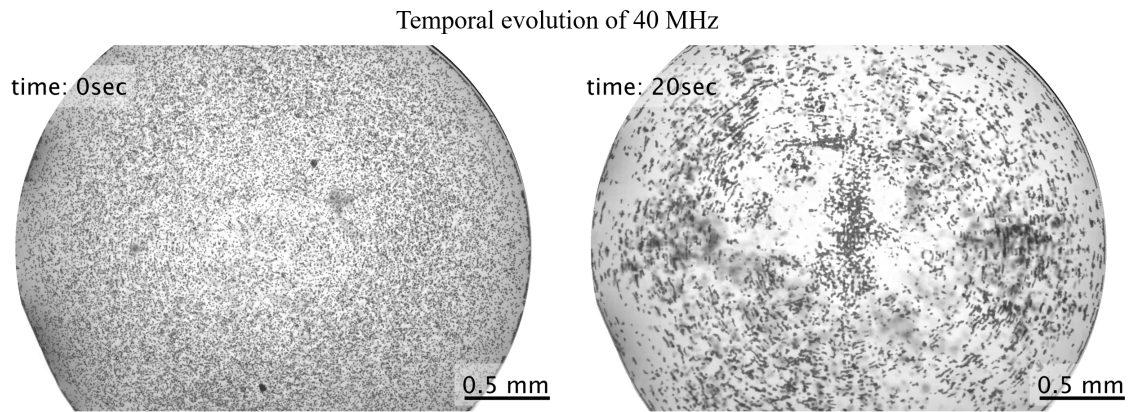
Figure 5.3: Temporal and spatial evolution of the 7 μm particles from the initial timestep to a time of 20 seconds at a frequency of 40 MHz. The majority of particles are entrapped in concentric rings at the bottom of the droplet, whereas the remaining particles are flowing inside the droplet due to hydrodynamic induced by the acoustic streaming.

proportional to the frequency, Eq. 2.4, implying that an increase in frequency leads to a decrease of the attenuation length α^{-1}. This is also presented in Tab. 2.1. Consequently, surface acoustic waves from opposite directions will not directly interfere with each other for higher frequencies. Hence a direct standing SAW field will not exist, and particles will not be trapped in the respective wells. The lowest frequency of 20 MHz exhibits an attenuation length along the solid-liquid interface, α^{-1} equal to 2.5 mm, Tab. 2.1. This length is longer than the radius of the droplet, 1.4 mm ± 0.1 mm, implying that the incoming SAWs will propagate beyond the centre of the droplet and interfere with the waves coming from the opposite side to create a standing SAW field capable of effectively entrapping particles. Conversely, 40 MHz exhibits an attenuation length, α^{-1} equal to 1.3 mm, which is shorter than the radius of the droplet, yet the experiments showed the entrapping of particles at this frequency as well. This comes from the definition of the attenuation length along the surface, which states that the waves decay with a factor of e. This means the acoustic wave is not fully attenuated when it reaches this length; it has only decayed by $1/e$. So opposite waves at 40 MHz have the possibility to encounter each other and create a standing SAW field for particle trapping.

The presence of thicker rings in the lowest frequency of 20 MHz compared to the 40 MHz configuration is noticeable when discussing the trapped particles at the bottom. This is attributed to the distance between the trapping wells or nodes of the acoustic field, which is determined by the wavelength of the SAWs that propagate. Longer wavelengths are associated with lower frequencies, resulting in larger spaces between each well. Consequently, the width of the well is greater, allowing for multiple particles to be trapped within the same well by expanding particles in the width of the well. The ability to store particles in the width of the well is demonstrated in Figure 5.4 by Collins et al. [17]. Notably, the diameter of the particle must be smaller than the wavelength, which holds true for both 20 MHz and 40 MHz frequencies.
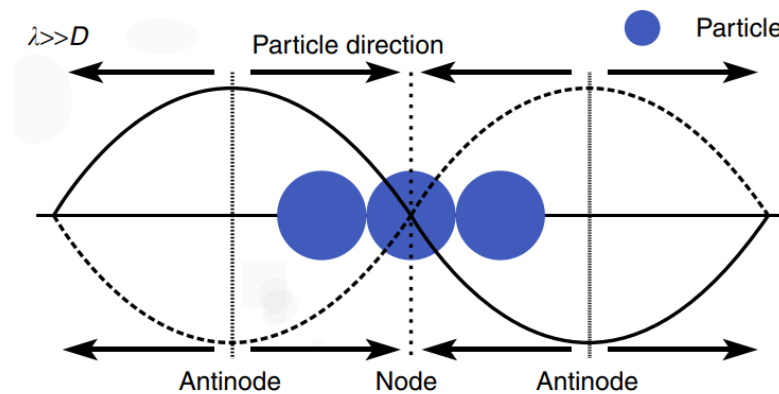
Figure 5.4: Illustration of particle accumulation at the pressure node. When the wavelength is greater than the particle diameter, multiple particles are attracted to the same pressure node. Accumulation of particles at the node results in an expansion of particles in width, consequently being visible as a thicker 2D concentric ring of trapped particles [17].

Particles in the region close to the bottom centre start to accumulate towards the middle, while the particles closer to the periphery are trapped for the 40 MHz configuration. This phenomenon suggests that the flow near the bottom of the droplet may move radial towards the centre. The particles experience a velocity gradient due to the no-slip condition at the solid-liquid interface, which causes them to roll with the flow along the bottom. This occurrence has been previously reported in the study conducted by Song et al. [20]. However, this rolling motion requires a significant velocity gradient to overcome the frictional force that keeps particles stationary at the bottom and the acoustic radiation pressure that entraps them. The weakest region of the standing SAW field is at the bottom centre of the droplet due to wave attenuation, as illustrated in Fig. 2.5. Consequently, implying weaker trapping abilities in this area. Therefore, hydrodynamics can more easily induce a rolling motion in this region, causing particles to accumulate around the bottom centre while particles closer to the periphery become trapped.

As previously mentioned, the trapping of concentric rings depends on the wavelength. Further examination of the spacing between the concentric rings was conducted to characterise the influence of the different wavelengths associated with the different frequencies. Figure 5.5 depicts a magnified view of the concentric rings located at the interface of the solid-liquid. The distance between the concentric rings was determined by measuring the distance between the consecutively marked crosses on the figure. The spacing distance is referred to as the spacing distance. This distance was measured in the favourable x-direction of the anisotropic material where properties such as the Rayleigh wave speed, v_R, are known.
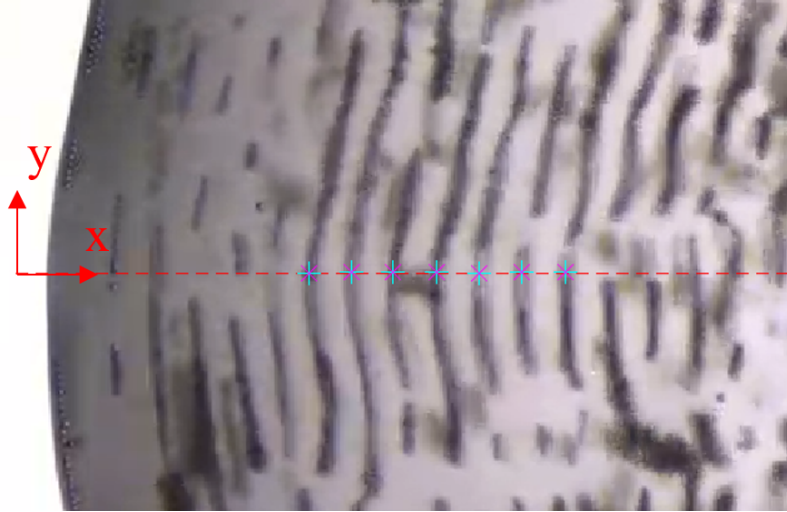
Figure 5.5: A magnification of the concentric rings formed at the bottom of the droplet at low frequencies. The spacing distance between the concentric rings is calculated by measuring the distance between the cross-marks, which indicates the position of the trapped particles. The distance is calculated in the x-direction of the anisotropic material where the Rayleigh wave speed is known. Thus, also the wavelength of the configuration can be calculated by Eq. 2.1.

Table 5.1 presents the average spacing distance and its respective standard deviation obtained during the experiments. The result shows an average spacing distance of 38 μm and 20 μm for the 20 MHz and 40 MHz frequencies, respectively. Observe that the spacing distance for 20 MHZ is roughly twice the value from 40 MHz. The equation for the wavelength, λ_{SAW} = v_R/f, indicates that half the frequency results in twice the wavelength. Since the trapping is dependent on the wavelength, it makes sense that 20 MHz obtains roughly twice the spacing distance of the 40 MHz configuration. The deviation might be due to the uncertainty of the measurements.

Table 5.1: Measured spacing distance between the concentric rings produced by the 20 MHz and 40 MHz configuration.

Frequency [MHz]	Measured spacing distance [μm]
20	38 ± 11
40	20 ± 5

According to the literature, there are two conflicting theories regarding the relationship between spacing distance and acoustic waves. Both theories state that the spacing of the concentric rings is half of the wavelength of the acoustic waves along the surface. However, there are two types of acoustic waves along the surface. One acoustic wave along the surface of the substrate and one oscillating acoustic wave in the liquid close to the surface induced by the underlying oscillations of the substrate. Meaning that the lithium niobate (LN) substrate underneath the droplet oscillates, which will induce oscillations in the liquid. Both acoustic waves vibrate with the same frequency, but the wavelength is different. This is due to the sound speed in the respective media, lithium niobate and water, which can be shown from the aforementioned equation for the wavelength λ_{SAW}. For the LN substrate, λ_{SAW} becomes v_R/f, whereas in the water liquid, λ_{SAW} becomes v_l/f. Li et al. [75] observed concentric

rings in a sessile droplet exposed by surface acoustic waves and observed that the distance between the rings was roughly half of the SAW wavelength, i.e. half the wavelength of the acoustic wave along the substrate given by the former aforementioned equation of λ_{SAW}. On the contrary, various literature regarding acoustic waves in the bulk liquid, Mazzaccoli et al., Strobl et al., and Raeymaeker et el. [18, 76, 77], report that the spacing distance between the trapped particles are half the wavelength of the acoustic waves in the liquid given by the latter aforementioned equation of $\lambda_{SAW} = v_l/f$.

Given that the speed of sound in water, v_l, and along the surface of the lithium niobate , v_R, are 1485 ms^{-1} and 3994 ms^{-1}, respectively, the wavelengths are calculated by the aforementioned equations and presented in Tab. 5.2 for both 20 MHz and 40 MHz frequency.

Table 5.2: Wavelenght of acoustic waves in water liquid and along the lithium niobate surface in the x-direction calculated by Eq. 2.1 equals 1485 ms^{-1} in the water and v_R equals 3994 ms^{-1} along the surface of the LN substrate.

Frequency [MHz]	Wavelength in water [μm]	Wavelength along LN surface [μm]
20	74	200
40	37	100

The findings of this study indicate that the distance between the particle rings is approximately equal to half the wavelength of the acoustic waves present in the liquid, as the measured spacing distance of 38 μm is roughly half of the wavelength in water, namely 37 μm for the 20 MHz frequency. This outcome is in line with previous research conducted by Strobl et al. [76], Raeymaekers et al. [77], and Mazzoccoli et al. [18], which suggests that the particles tend to assemble at the pressure nodes created by the pressure waves in the liquid. Furthermore, the study found that it is not the acoustic waves on the surface of the substrate that traps the particles, but rather the acoustic waves located in the liquid near the bottom of the droplet, which are induced by the waves of the substrate underneath. The particles move along with the vibrations of the liquid since they are suspended within it.

5.2.1 Analyzing the impact of parameter modifications on concentric particle trapping pattern

After examining the phenomenon of concentric particle trapping, further experiments were carried out to determine if adjusting the diameter, volume concentration, droplet volume or input power had any effect on the spacing distance. Ensuring successful particle trapping within droplets requires the prevention of hydrodynamic forces from overpowering and disrupting the concentric trapping at the bottom. In order to reduce the hydrodynamics and increase the influence of radiative forces, the volume of the droplet was increased to make more space for particle movement and hence reduce the velocities. On the contrary, to increase the hydrodynamics to see its effect, experiments of smaller particle diameter and concentration were conducted. Additionally, the power was increased to 260 mW for the same reason. The analysis was confined to the 20 MHz frequency due to its greater visibility of the concentric particle trapping compared to the 40 MHz frequency. All the different parameter tested are presented in Tab. 5.3.

The first configuration of Tab. 5.3 is the one used for the main experiments of this thesis. The findings indicated that the spacing distance was roughly similar to the first configuration

Table 5.3: Results from the analysis of parameter modification on the aggregation of concentrically trapped particles for 20 MHz frequency. The variation of parameters does not seem to have a sufficient influence on the spacing distance produced by the trapping process. Notice that the first configuration is the one utilised in the main experiments of the thesis.

Diameter and volume concentration	Volume	Input power	Spacing distance
[μm] / [-]	[μL]	[mW]	[μm]
7 / 1:5	2	100	38 ± 3
1 / 1:10	2	100	39 ± 2
7 / 1:5	2	260	38 ± 3
7 / 1:5	5	100	38 ± 3

regardless of the tested parameters. All configurations exhibited the same magnitude of uncertainty. Even for increased hydrodynamics, the particles tended to be trapped at the bottom solid-liquid interface.

After carefully analyzing the data, it seems that manipulating the operational and experimental conditions did not yield any noticeable changes in the average spacing distance. Reducing the particle size will exponentially reduce the acoustic radiation force since $F_{ARF}^{st} \propto r^3$. By doing so, the hydrodynamic becomes more dominant. However, reducing the size from a diameter of 7 μm down to 1 μm still produced concentric trapping, indicating that the acoustic waves in the water liquid responsible for trapping the particles exhibit sufficient enough pressure wells at 100 mW to entrap particles. Increasing the power also induces more hydrodynamics, which transmits more kinetic energy over to the particles in order for them to escape the entrapment. However, an increase in power also implies higher amplitudes of the waves [78]. And higher amplitudes of the acoustic waves lead to a higher pressure gradient that influences the particles and manages to trap them. Due to the strength of the acoustic radiation force, many particles at the bottom remain trapped, resulting in the formation of concentric rings. However, as the droplet evaporates, the hydrodynamic effects become more prominent due to the less movable space of the flow. This increase in hydrodynamics causes more particles to escape the concentric rings and move with the flow field.

5.2.2   High-Frequency concentric particle trapping at 120 MHz

In order to investigate the impact of operating frequency on particles, it was necessary to explore their particle trapping behaviour at high frequencies where hydrodynamics are minimized. To achieve this, power input was decreased, and volume was increased, as discussed in the previous subsection. Under high-frequency conditions, the attenuation length across the solid-liquid interface is small enough such that a standing SAW field is not established. Instead, particles experience travelling SAW along the bottom of the droplet.

In the absence of a standing surface acoustic wave (SSAW) field, particle trapping may not occur, and under the influence of a slow or stationary flow field, a distinct phenomenon could emerge. Devendran et al. [79] conducted a recent study on the trapping ability of particles through the self-interaction of travelling waves. Figure 5.6 illustrates the refractive behaviour of waves in a liquid, where the pressure field is denoted by red and blue colours. The upper images demonstrate the refraction of travelling SAW at the Rayleigh angle, as explained by Eq.

2.2. The middle image depicts the creation of cylindrically propagating waves as the travelling waves refract with the periphery of the droplet, known as the Huygens–Fresnel principle. The bottom image shows the superposition of these two wave refractions, with the zero pressure points denoted by black solid lines, which are the points of attraction for particles.
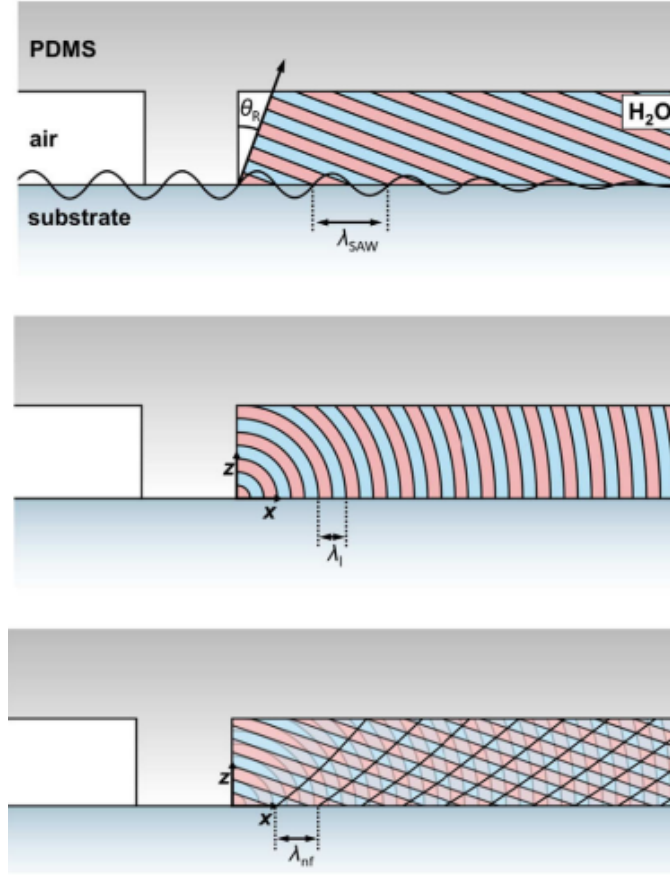
Figure 5.6: Illustration of the self-intersection theory of travelling SAW (lower image) by superposition of the pressure field created by refraction of waves with a Rayleigh angle (upper image) and the circular pressure field created by refracting upon the periphery of the droplet known as the Huygens–Fresnel principle (middle image) in a microchannel surrounded by polydimethylsiloxane (PDMS) [79]. The superposition of these two pressure fields creates zero pressure nodes which the particles attract to. The spacing distance of these pressure nodes at the solid-liquid interface is given by λ_{nf}.

The spacing in between the nodal pressure points due to this super-position is given by λ_{nf}, which is expressed by the equation

$$\lambda_{nf} = \frac{v_l}{f}\left(1 - \frac{v_l}{v_R}\right)^{-1}. \tag{5.1}$$

However, this study was conducted in a microchannel with a single straight IDT. Investigation regarding how applicable this is in a sessile droplet exposed by travelling SAW from spiral IDT is conducted in this thesis.

In order to perform the analysis at hand, a short attenuation length was required. As the frequency increases, the attenuation length along the solid-liquid interface becomes shorter.

Therefore, a frequency of 120 MHz was chosen for this purpose. According to the data presented in Tab. 2.1, the attenuation length at 120 MHz is 0.42 mm. Furthermore, the volume was increased, and the input power decreased in order to reduce the hydrodynamic inside the droplet. Figure 5.7 depicts the setup where a 40 μL droplet was exposed to SAW with a 120 MHz frequency and 10 mW input power. The results presented in Fig. 5.8 demonstrate that the particles were indeed trapped at the bottom in a circular pattern. Due to the high concentration of particles, some of them were stacked on top or in between the rings, thereby reducing the visibility of the rings. This indicated that the travelling SAWs have successfully entrapped the particles at the bottom, proving that a standing SAW field is not always necessary for trapping particles. It should be noted that the concentric rings obtained at lower frequencies were more visible and required less time to produce. Nevertheless, the results proved that it is possible to trap particles into concentric rings in a travelling SAW field.
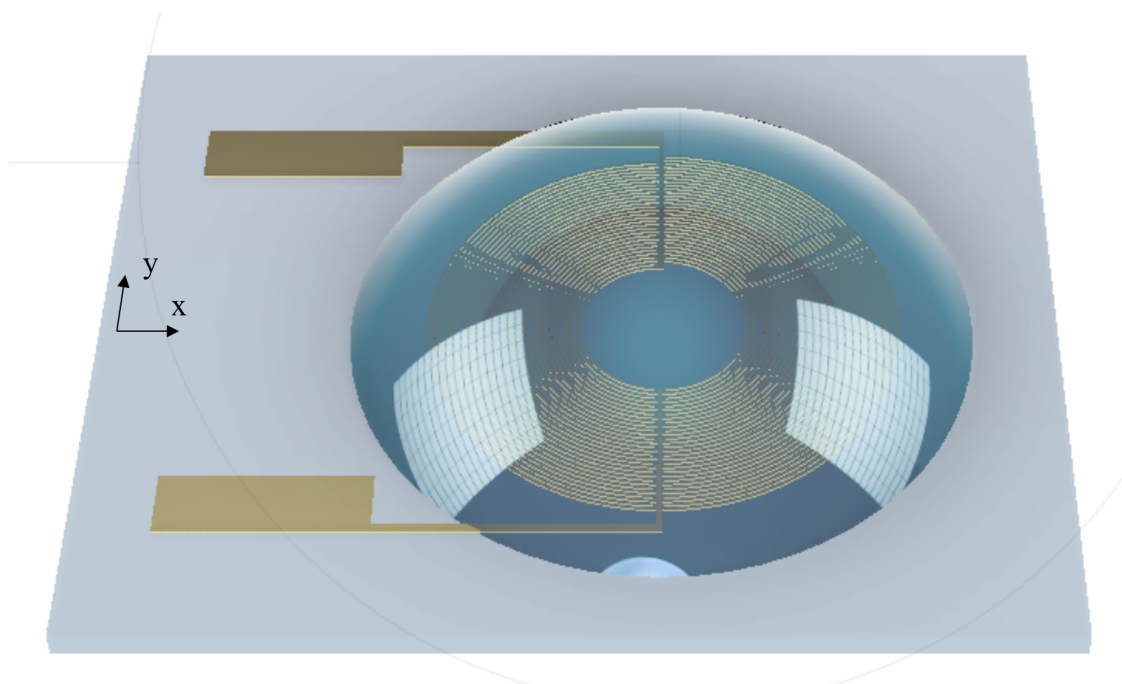
Figure 5.7: Illustration of the experiment conducted for 120 MHz with a 40 μL droplet at low power in order to investigate the trapping abilities for travelling SAW typically generated at high-frequency configurations. Note that the droplet covers the spiral IDT due to increased volume.

Table 5.4 presents the experimental findings for the distance between the trapped particle rings in a travelling SAW field at 120 MHz, which was measured to be 18 μm. The observed entrapment of particles in a standing SAW field is attributed to the acoustic waves generated in the liquid near the solid-liquid interface. The details regarding this phenomenon are discussed in Sec. 5.2. For the low frequencies that establish a standing SAW field, the spacing between the rings corresponds to half the wavelength of the acoustic waves in the liquid, as shown in the previous subsection. For the case of 120 MHz, that would be calculated to be 6.2 μm ($1/2\,\lambda_{SAW} = 0.5\,v_l/f$). However, the measured spacing is significantly larger than this value, indicating that the obtained spacing distance between the lower frequencies which exhibit a standing SAW field and the travelling SAW field at higher frequencies are dissimilar.

For the self-intersection theory illustrated in Fig. 5.6, the spacing distance λ_{nf} is calcu-

Table 5.4: Measured spacing distance for the 120 MHz frequency with a 40 μL droplet at 10 mW input power in order to investigate the trapping abilities for travelling SAW.

Frequency [MHz]	Measured spacing distance [μm]
120	18 ± 3

lated to be 19.7 μm by Eq. 5.1 described above. The average experimental measurement of 18 μm deviates by approximately 8.6% from the aforementioned analytical value. Nevertheless, taking into account the standard deviation, there exists a possibility that the spacing distance for the travelling surface acoustic wave (SAW) field at 120 MHz corresponds to the self-intersection theory, where pressure nodes are formed by the interaction between pressure waves generated at a Rayleigh angle and the cylindrical refraction of the waves. This result indicates that the spacing distance for standing SAW field achieved at lower frequencies corresponds with half the wavelength of the acoustic wave in the liquid, whereas the spacing distance for travelling SAW correspond with the spacing distance created by self-intersected waves, λ_{nf}.

This result has a huge potential for particle trapping at high frequencies. Even though the literature report concentric particle trapping inside a sessile droplet [21, 51], this only occurs at low frequencies below 20 MHz. In these cases, the attenuation length is sufficient enough to create a standing SAW field. Spacing of rings at a high frequency where only travelling SAW exist has not been reported to the best of the author's knowledge. Higher frequencies exhibit smaller wavelengths, which is essential in sub-micron particle manipulation. This is because controlling the trapping process of sub-micron particles implies the necessity of creating wavelengths in the order of micrometre or all the way down to nanometers. In turn, shorter wavelength means higher frequencies, hence also a shorter attenuation length. When the attenuation becomes shorter, the possibility of creating travelling surface acoustic waves increases since the opposite waves won't reach each other. Therefore, they will not interfere to create a standing SAW field. In order to obtain a standing SAW field at higher frequencies, the radius of the droplet has to be reduced such that the opposite waves reach each other. The higher the frequency, the smaller the droplet has to be in order to obtain a standing SAW field. Besides, higher frequencies emphasise the increase in hydrodynamic, which makes it more difficult to entrap particles due to the acoustic radiation force. This shift is previously discussed in Sec. 5.1. The theory of self-intersected waves makes it possible to trap particles in a travelling SAW field for high frequencies, and the results in this section show that this is possible in a sessile droplet. This has a huge potential for nanoscale particle manipulation since very high frequencies imply wavelength in the order of nanometers.

5.3   Cluster aggregation

Experimental analysis of the temporal evolution, Sec. 5.1, revealed that droplets subjected to the high frequency of 80 MHz and 120 MHz at 100 mW input power experience the formation of clusters. Further investigation into the cluster formation yields a characterisation of the particle aggregation pattern inside the droplet and provides a qualitative examination of the influential hydrodynamic forces and the acoustic radiation force, hence addressing the two first
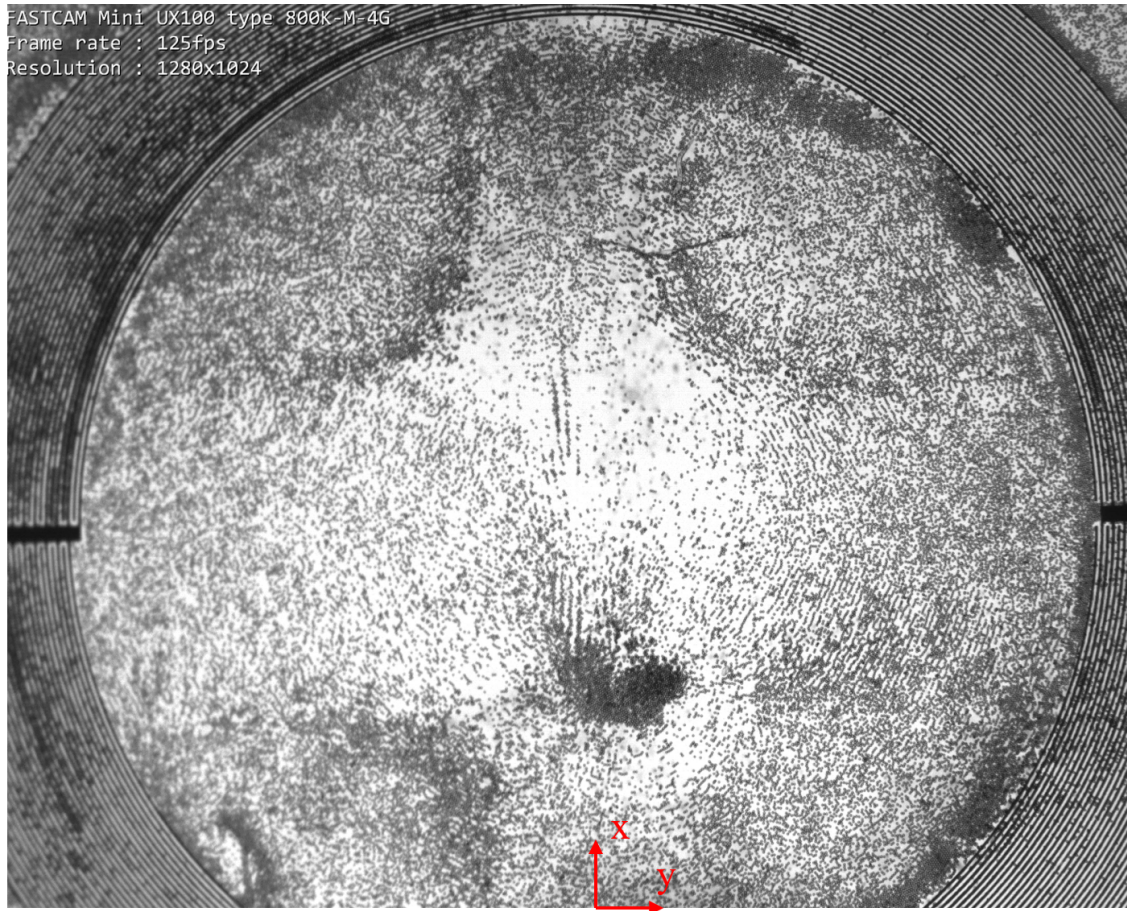
Figure 5.8: Image of the experiment conducted at a high frequency of 120 MHz with a 40 μL sessile droplet deposited in the centre of the spiral IDT. The experiment was conducted at a low input power of 10 mW, and the image was captured after 30 minutes of SAW actuation. Trapped 7 μm particles form ring patterns at the bottom of the droplet.

objectives of the thesis. Due to the fact that clusters only appear for these targeted frequencies, the lower range of 20 MHz and 40 MHz will not be included nor discussed in this subsection.

The aggregation process

In order to gain insights into the mechanism of particle cluster aggregation for higher frequencies, experiments were performed at frequencies of 80 MHz and 120 MHz for PIV analysis. The PIV analysis was performed for 100 consecutive frames, equal to 0.1 seconds, where the first frame in the sequence corresponded to one second after the SAW was turned on. The selected time frame was specifically chosen to analyze the initial dynamics of the particles while they are still dispersed in the fluid, providing insights into their behaviour prior to clustering. The recordings for the PIV measurements are taken from above by looking at the horizontal plane close to the top of the droplet.
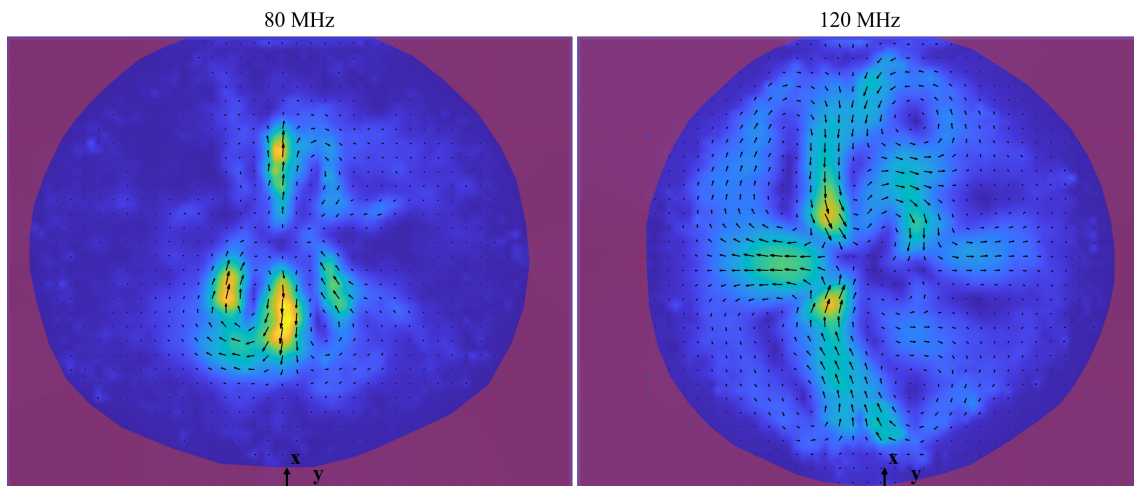
80 MHz   120 MHz

Figure 5.9: Velocity magnitude field for the 80 MHz and 120 MHz configurations obtained by PIVlab. A colour scheme is used, which represents an increasing velocity for increasing yellow saturation. The velocity scale bar ranges from zero to a maximum average velocity of 5.1 mm/s. The comparison shows a higher local velocity at 80 MHz in the centre, while 120 MHz exhibits a larger area around where the average velocity is higher than for 80 MHz.

Figure 5.9 displays the average velocity magnitude of the particles for both frequencies. A colour scheme represents an increasing velocity for increasing yellow saturation. The velocity scale ranges from zero to a maximum average velocity of 5.1 mm/s. The region close to the centre of the droplet shows the highest velocity region, indicating that the flow emerges or gets sucked up in this central area. Figure 5.10 illustrates the poloidal flow stream where the flow in the middle of the droplet streams upwards and emerges from the centre as it reaches the top periphery. The observations suggest a poloidal flow stream through the droplet, as indicated in Fig. 5.10. The poloidal flow implies a recirculation within the droplet, which explains why PIVlab software detects low velocity in the exact centre of the droplet. Although particles move upwards or downwards in the centre of the droplet, PIV software only calculates the 2D displacement in the horizontal focal plane. Therefore, PIVlab detects the particles as stationary while they travel in the out-of-plane direction.
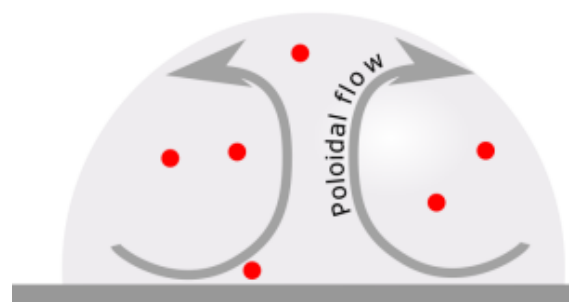
Figure 5.10: Schematic of a poloidal flow where the flow field recirculates inside the droplet [20].

At 80 MHz, the flow pattern indicates upward movement through the droplet in the central region due to the particle's movement away from the centre at the top At 120 MHz, PIV measurements reveal a range of motions in various directions. Although the highest velocity

regions move towards the centre, there exist broader regions with a lower velocity that move away from it. Hence, it is challenging to conclude whether the flow moves downwards in the middle of the droplet and therefore sucks all the particles in the top towards the central region or visa versa. This trend is also observed in other experiments at 120 MHz. Comparing the two frequencies reveals that while 80 MHz has a higher maximum velocity, it is confined to very local regions located closer to the centre and particle motion closer to the periphery is lower. At 120 MHz, flow fields tend to be more chaotic, leading to more vortices due to increased disturbance in the field. This is evidently shown in Fig. 5.11.

(a) Vorticity field for the frequencies 80 MHz and 120 MHz.

(b) Streamlines for the frequencies 80 MHz and 120 MHz.
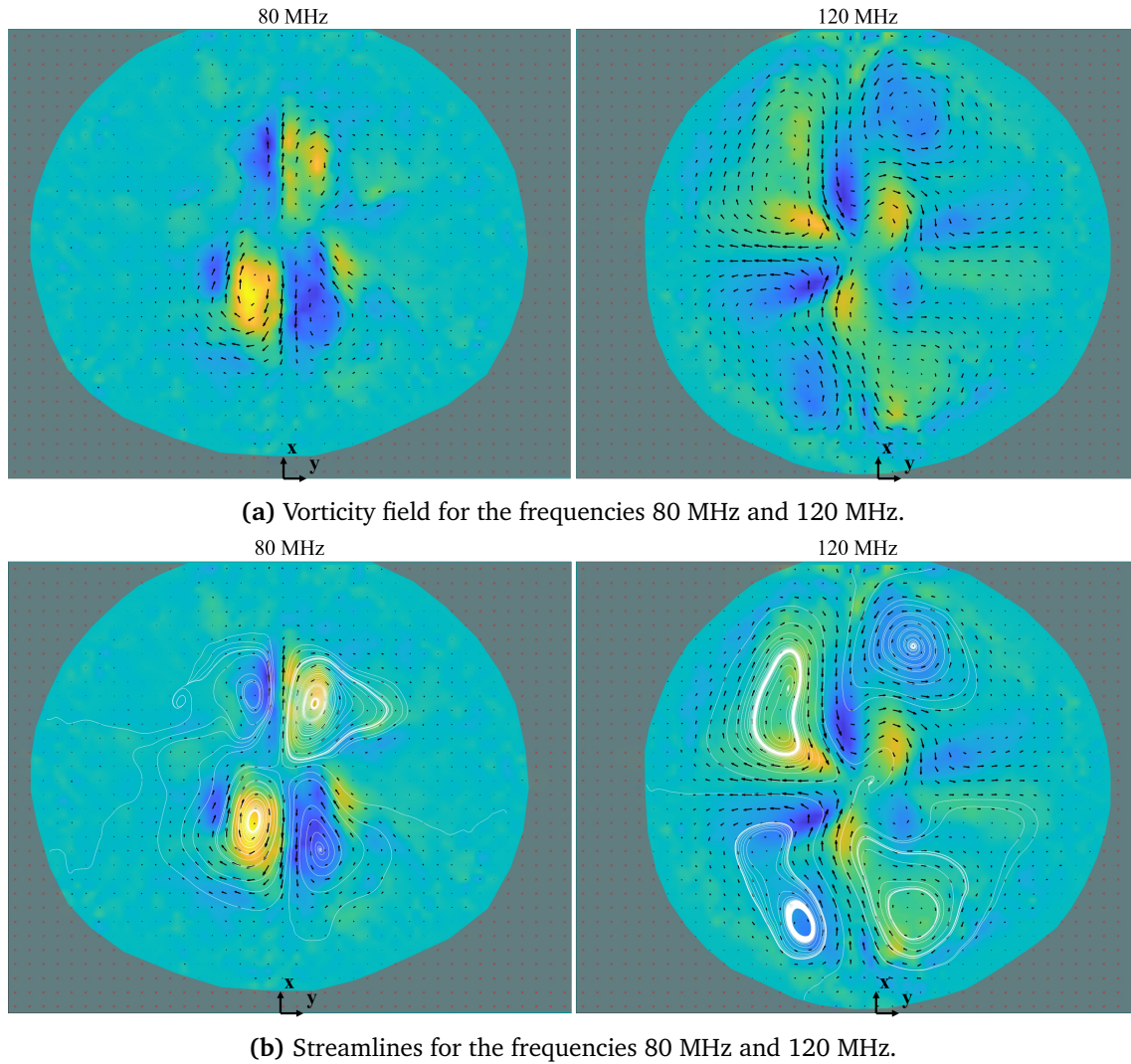
Figure 5.11: Vorticity magnitude field for the 80 MHz and 120 MHz configuration obtained by PIVlab. The colour bar represents the intensity of the vorticity field. The strength of the clockwise vorticity field is depicted by a higher level of yellow saturation. On the other hand, a stronger counterclockwise vorticity field is indicated by an increase in blue saturation. The vorticity scale bar ranges from -22.8 s^{-1} to a maximum average vorticity of 24.5 s^{-1}. The vector field indicates the flow direction of the particles. Image a) indicates that 80 MHz exhibits fewer and stronger vorticities compared to the 120 MHz configuration. Additionally, 80 MHz produces vorticities that exhibit a more circular behaviour than 120 MHz, as seen in subfigure b).

The vorticity field for both frequencies in the same scale is presented in Fig. 5.11a. It is noticeable that the 120 MHz configuration exhibits more regions of vortices, both in the central region and away from the centre. On the contrary, 80 MHz exhibits fewer vortex regions, although the ones that exist are primarily formed in the close centre region. One of the vortices is more dominant than the others. Additionally, Fig. 5.11b shows the streamlines of the particles, which are drawn over the vorticity plot to indicate the significant impact of the vorticity on particle behaviour. It is worth noting that the particles move in a circular motion for 80 MHz, while some streamlines for 120 MHz demonstrate how the particles move in a more non-circular motion.

A particle trajectory that is of a circular motion promotes the action of effective cluster aggregation due to the centripetal force. Trajectories that deviate from a circular motion will experience variation in the centripetal force, which is a disadvantage for accumulating the particles in the centre of the vortex. A circular vortex in a liquid will experience a concave formation of its free surface, implying concave isobars in the liquid [49]. When a suspended particle is subjected to the vortex, it will experience a netto pressure force induced by the centripetal acceleration and the hydrostatic pressure in a radial inward and upward direction, as presented in Sec. 2.4.1. This netto pressure force acts on all the particles that are located within the vortex, resulting in an accumulation of particles in the central top surface of the circular vortex. Figure 2.7 illustrates the netto pressure force in a vortex by simplifying it to a vortex in a cylindrical container. This is one explanation of the aggregation of clusters and why it is located in the upper part of the droplet.

Aggregation time

To effectively accomplish the first objective of characterizing the aggregation pattern, it is crucial to consider the aggregation time of the clusters. The aggregation time refers to the duration from the activation of SAW to the formation of compact clusters. Knowing the estimated time for cluster production is important, especially considering the rough flow treatment and heat treatment that the bioparticles undergo during the SAW actuation. The vortex motions of the fluid induce a centripetal trajectory of the particle, and excessive hydrodynamics may lead to significant harm to the bioparticle. The longevity of bioparticles is significantly impacted by the presence of heat. Through the conduction mechanism in the substrate, electrodes facilitate the transmission of heat to the droplet. Increasing the power input to the electrodes results in intensified heat generation, leading to a rise in droplet temperature. In turn, this will harmfully affect the particles if they are exposed to high temperatures or prolonged heat exposure. Thus, understanding the aggregation time is essential for achieving efficient aggregation within the desired time frame.

The time required for 80 MHz and 120 MHz to first assemble 7 μm particles into clusters has been quantified and presented in Tab. 5.5. On average, one cluster was created after 15 seconds at 80 MHz, and exposure to 120 MHz frequency resulted in two clusters forming after 54 seconds.

Based on the analysis of Fig. 5.9 and Fig. 5.11, it is evident that the 80 MHz frequency exhibited a greater maximum velocity in the local region where the dominant vortex was located, as indicated by the saturation of the images. Additionally, compared to the 120 MHz frequency, the circular vortex in the 80 MHz case was narrower. The presence of a high velocity in the vortex and a low radius suggests a high centripetal acceleration, which enables a fast

Table 5.5: Average aggregation time for the particles to accumulate into one cluster (80 MHz) and two clusters (120 MHz) and their respective standard deviations.

Frequency [MHz]	Cluster aggregation time [s]
80	15 ± 3
120	54 ± 17

aggregation time for the 80 MHz frequency, as observed in the subsequent subsection. The single dominant vortex also enables the creation of a single cluster that attracts the majority of the particles, explaining why 80 MHz was able to aggregate particles into a single cluster. In contrast, the 120 MHz frequency exhibited a more complex vorticity field, with multiple vortices capable of attracting particles to their centres. Consequently, a flow field containing more vortices can lead to the formation of multiple clusters, as observed in the case of 120 MHz.

Intensity plot

The surface monochrome intensity plot illustrated in Fig. 5.12 provides visualization of the aggregation performance and particle assembly formation of 7 μm polystyrene particles. Darker regions are represented by a higher intensity value. It is worth noting that the plots were generated at an instantaneous time of 60 seconds, indicating that the single cluster of 80 MHz was able to maintain its compactness after accumulating during the first 15 seconds as given in Tab. 5.5. The individual peaks depicted in the surface intensity plot represent the locations of individual particles within the flow. The presence of only a few individual particles in the 80 MHz plot suggests a highly efficient aggregation process. Conversely, the frequency of 120 MHz resulted in the detection of more individual particles, however, the amount is relatively small compared to the initial particle distribution, indicating that this aggregation process is also highly efficient.
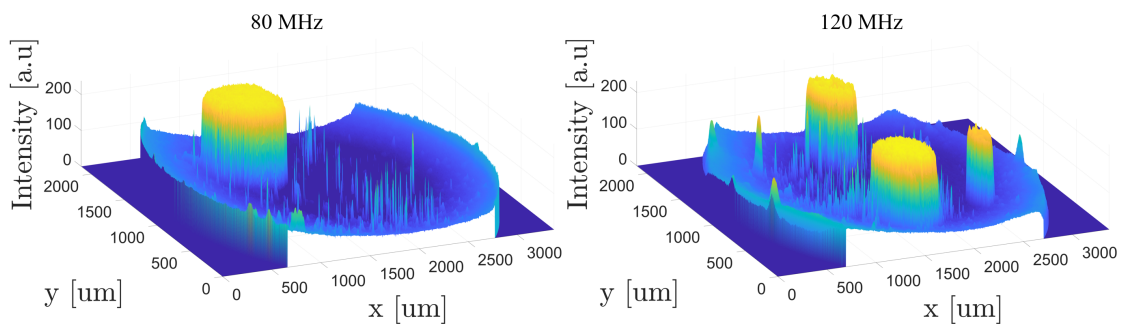
Figure 5.12: Surface monochrome intensity plot of both the 80 MHz and 120 MHz frequency at the instantaneous time of 60 seconds. Darker regions are represented by a higher intensity value, hence the high yellow saturated areas represent the produced single cluster at 80 MHz and the multiclusters at 120 MHz, both operating at 100 mW. Furthermore, the small individual peaks indicate dispersed individual particles. The higher intensity around the periphery is caused by the sharp refraction of light as it enters the droplet from above.

The line intensity plot in Fig. 5.13 illustrates the intensity over the marked line of the figure. Clusters along this line are detected and plotted with their respective position. The

higher and more consistent the intensity, the more compact the clusters are. The compactness of the clusters is reflected in their intensity, where more dispersed clusters allow greater light transmission, resulting in a brighter illumination than compact clusters, which tend to block more light. This is apparent in the case of 120 MHz, where the intensity of the upper cluster fluctuates around the centre, representing a tiny region of brighter illumination. However, the dip, in this case, is very small, indicating a compact cluster. Conversely, the single cluster for 80 MHz exhibits high and consistent intensity, suggesting a compact cluster.
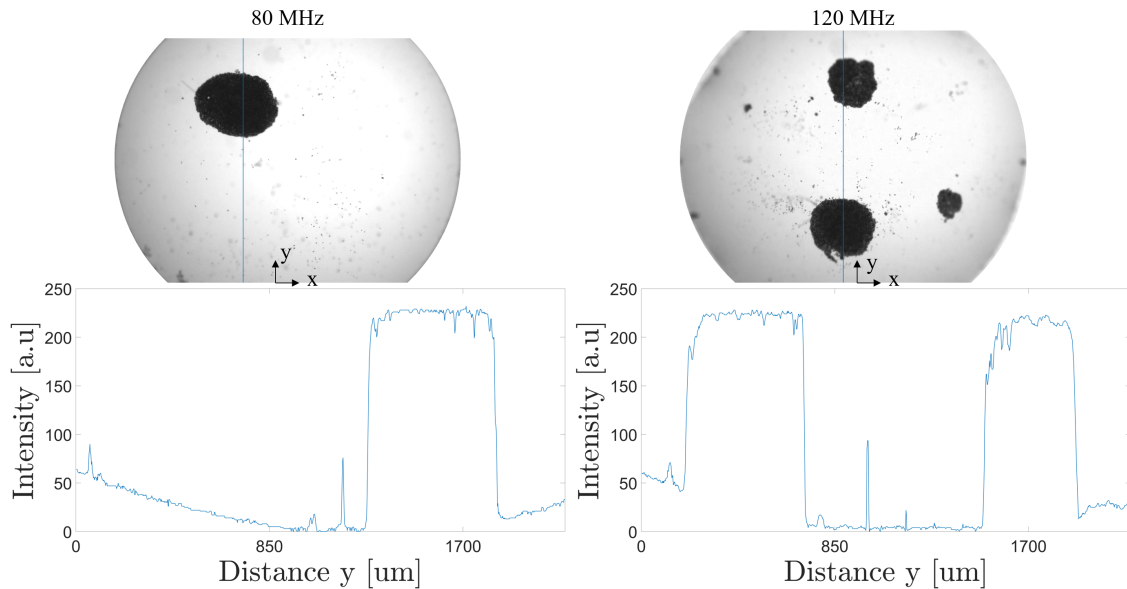
Figure 5.13: Line intensity plot showing the darker areas over the marked line for the purpose of characterising the compactness of the clusters.

A reason for the more individual particles at 120 MHz might be the complex multi-vortex flow field at the early time period, as shown previously in Fig. 5.11. The minor vortices manage to attract some particles, which will then be prevented from aggregating into the larger cluster in the early temporal stage. Conversely, the existence of fewer vortices at 80 MHz is one possible reason for the higher aggregation process.

Cluster geometry

In order to achieve the first objective of characterizing the aggregation pattern, it is important to take into account the geometry of the clusters obtained at higher frequencies. Table 5.6 shows the measured diameters of the single cluster for 80 MHz and the two multiclusters for 120 MHz at the time where the clusters first form, i.e. on average at 15 seconds and 54 seconds, respectively. The table also provides the eccentricity factor to quantify the shape of the cluster. The eccentricity factor is a measure of how circular something is compared to a perfect circle, with zero being a perfect circle and values between zero and one indicating an ellipse. The closer the eccentricity is to zero, the more circular the cluster is. The left and right values of the diameter for 120 MHz represent the clusters positioned at the higher and lower range of the y-direction, respectively.

The results indicate that the single cluster produced a larger diameter compared to the two multiclustered ones. Additionally, the single cluster had a more consistent average diameter,

as evidenced by the low standard deviation for 80 MHz compared to 120 MHz. Specifically, the relative standard deviation of the single cluster was calculated to be 5.2 %, whereas the upper and lower multi-clusters obtain a relative standard deviation of 18.2% and 23.2%, respectively. The eccentricity factor is very similar for both frequencies, but 80 MHz exhibits an eccentricity closer to zero, indicating a more circular cluster.

Table 5.6: Diameter and eccentricity of the clusters produced at the aggregation time provided in Tab. 5.5 for the frequencies of 80 MHz and 120 MHz.

Frequency [MHz]	Cluster diameter [μm]		Eccentricity factor [-]	
80		688 ± 36		0.56 ± 0.18
120	523 ± 95	652 ± 151	0.66 ± 0.10	0.62 ± 0.17

Given that 80 MHz produced a single cluster due to the dominant vortex, it was expected that the diameter was greater than for two separate ones. However, the surprising similarity in diameter between each of the two multiclusters and the single cluster suggests that the single cluster may be composed of layers of particles in the z-direction, giving it a flat appearance in the 2D horizontal focal plane. This tendency was also evident in the tornado structure observed at 110 seconds for 80 MHz, as depicted in Fig. 5.1. Although the tornado appeared small in the 2D focal plane, it actually extended from the bottom to the top of the droplet.

At a frequency of 120 MHz, the particles tended to form two clusters, with a tendency to be attracted towards either one of them in different experiments. In some experiments, the majority of particles gathered at the lower cluster, while in others they assembled at the upper one. The possibility of particles forming at multiple clusters for various experiments results in a larger standard deviation. However, at 80 MHz, all particles were drawn to one stronger cluster, resulting in a more consistent diameter across all experiments and hence a smaller standard deviation.

5.3.1 Temporal cluster dispersion and reassemble

To investigate how frequency influences the aggregation behaviour of the particles, further investigation regarding temporal cluster dispersion and reassembling seen from the temporal evolution in Sec. 5.1 was conducted. Temporal intensity plots were carried out for this purpose. Figure 5.14 and 5.15 illustrates the different regimes in which the aggregated clusters dissperse into rings or tornadoes for 120 MHz and 80 MHz, respectively, before reassembling into new clusters. This behaviour was briefly mentioned in Sec. 5.1.

80MHz

The particles aggregated into a single cluster relatively early, as described above in Sec. 5.3. After a while, the cluster dispersed into tornadoes. The tornado tended to form in the centre of the droplet where the omnidirectional flow met, and the flow field moved in a verticle direction. The tornados would often separate into two smaller assemblies, one at the top of the droplet and one at the bottom. The upper and lower assemblies would tend to lay aligned on the vertical axis, hence the lower cluster would block the visibility of the upper one. Consequently, making it sometimes challenging to see whether there was a tornado or two assemblies. This phenomenon was difficult to observe from the intensity plot since the horizontal

Figure 5.14: Surface and line intensity plot for the temporal evolution of 80 MHz frequency exposed to 100 mW input power. The cluster disperses into a tornado structure at 110 seconds for them to reassemble into clusters later on. This transformation occurs multiple times during the lifetime of the droplet. The surface plot indicates the high aggregation performance and position of the tornado structure and cluster. The line plot indicates a compact assembly of particles where minimal light is transmitted through the assembly.

focal plane made it challenging to observe motion in the out-of-plane direction. Whenever there existed a tornado structure or two clusters aligned on the same vertical axis, the intensity plot would only represent this as one peak. After a while, the particles tended to form back to either a single cluster or two multi-clusters. However, the process of accumulating into tornadoes could appear multiple times throughout the lifetime of the droplet.

Furthermore, the resulting surface intensity plot shows a relatively small amount of individual particles. There are not many small peaks indicated on these plots. Consequently, indicating a high-performance aggregation.

120 MHz

In the case of the highest targeted frequency, the multiclusters also dispersed. The break of the clusters occurred such that particles separated themselves from the cluster, or the cluster evolved into a ring formation. At some point, a tendency for the particles to form two large rings in the upper y-direction of the droplet, as depicted for 110 seconds in Fig. 5.15 occurred. Subsequently, the two rings tended to collapse together at some point and reassemble into two or three clusters. The process of cluster dispersion and reassembling could appear multiple
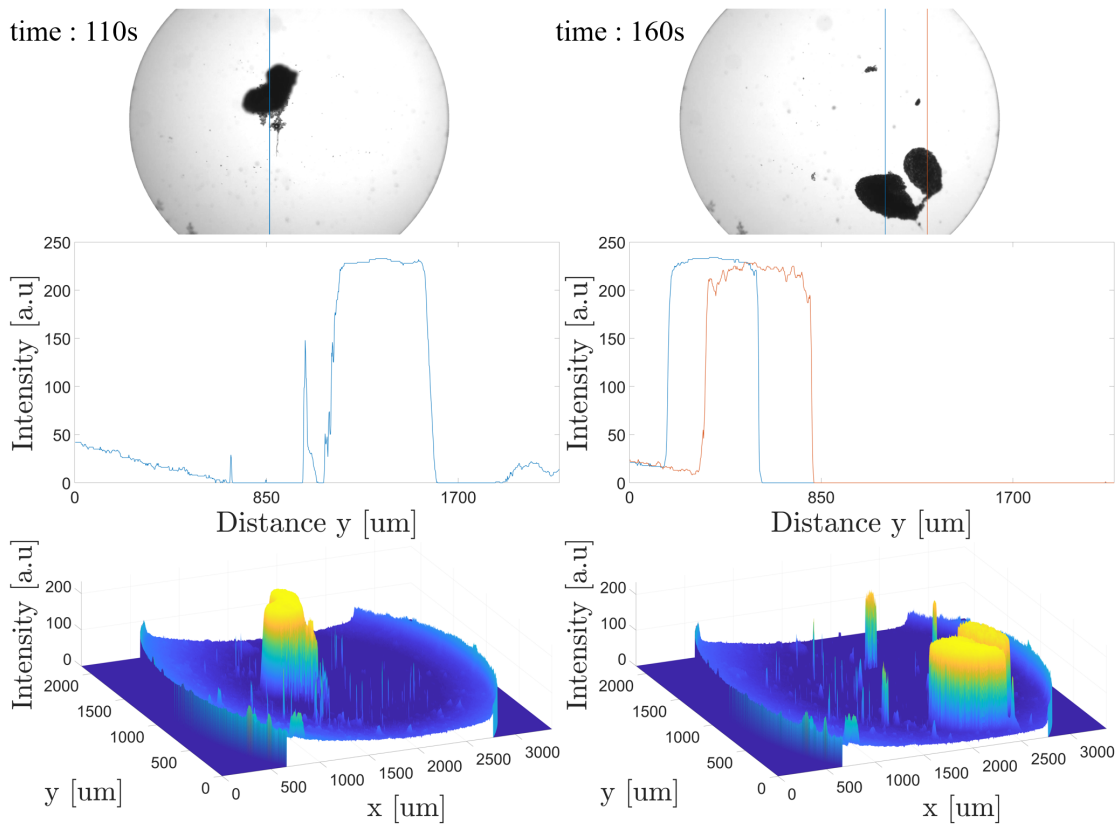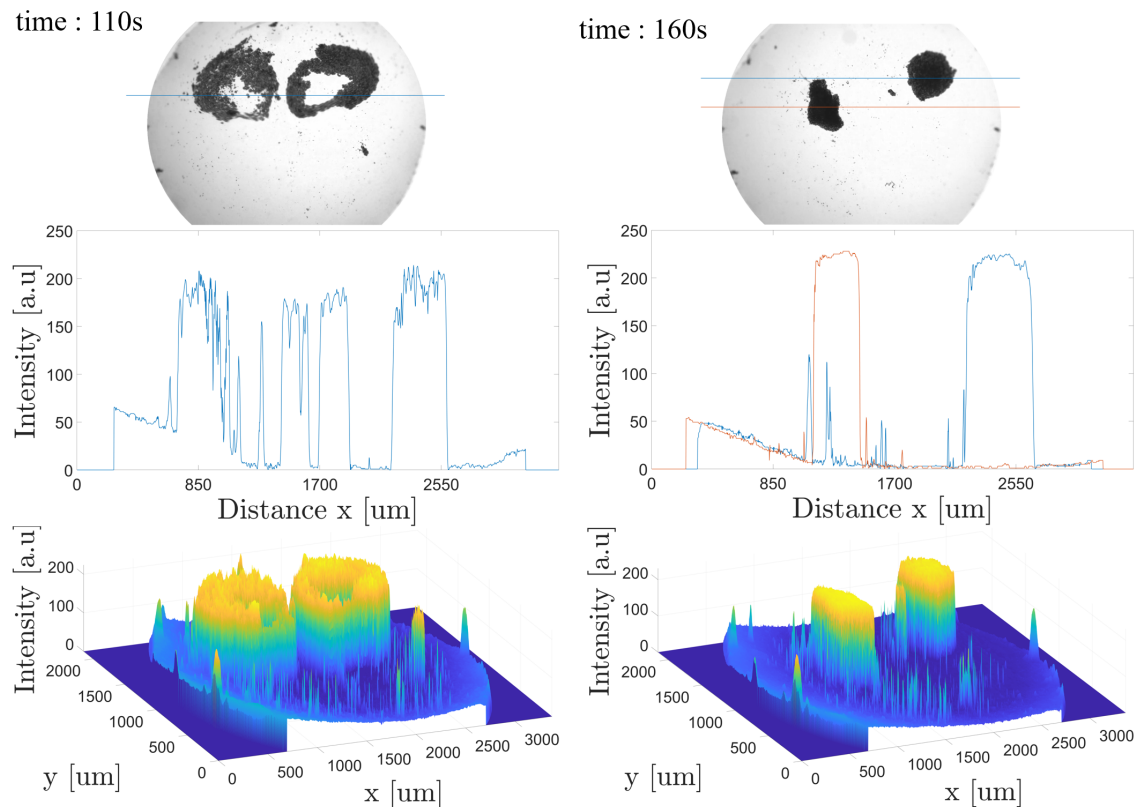
Figure 5.15: Surface and line intensity plot for the temporal evolution of 120 MHz frequency exposed to 100 mW input power. The intensity plots show the multiple-ring formation of dispersed particles. Additionally, the lower peaks in the line plot indicate the more dispersed particle assembly. On the contrary, when the rings collapse into clusters again, the peak of the line plot increases, hence indicating a more compact assembly. The surface intensity plot demonstrates a high-performing aggregation process due to few remaining individual peaks.

times.

The surface intensity plot shows more individual particles and microclusters for 120 MHz compared to 80 MHz, implying that not all particles managed to aggregate into larger clusters. However, relative to the initial particle distribution, a lot of particles still managed to aggregate. Hence, the performance of aggregation is great.

It is challenging to understand what broke up the clusters. One of the reasons was the higher velocities within the central region of the droplet, as shown previously in Fig. 5.9. When the cluster comes too close to the central region where severe velocities appear, the flow manages to influence the outer particles of the cluster. The amount of particles that are able to be torn off the cluster depends on how close to the high-velocity region the cluster is located. The outer particles are typically torn off in a chain formation. This chain of particles has the potential to form a ring formation if the particle-chain position itself in a circular vortex. Sometimes the whole cluster becomes one long chain. In the case of 80 MHz specifically, the long chain managed to get sucked up into the rotational poloidal flow in the centre of the droplet. When this occurred, the chain became a vertical swirling tornado.

The variation in velocity inside the droplet depends on a lot of factors, among them the volume. When the volume shrinks due to evaporation, the flow field changes. When the flow

field changes, the particle motion and particle behaviour change. Consequently, also the aggregation pattern changes.

5.4 Single-system 80 MHz acoustofluidic device

The second part of the results aims to explore the aggregation pattern obtained for the single-system device. The single-system would be particularly advantageous in bio-sensors, as the desired aggregation pattern could be obtained from a single device by adjusting the operating frequency and input power, eliminating the necessity of fabricating various devices for each frequency. The following section addresses the third objective with regard to the comparison of the aggregation behaviour of the single-system to the ones obtained for the multi-system presented above. This is done by first examining the single-system configuration at the targeted frequencies at an input power of 100 mW.

Furthermore, the subsection addresses the fourth and final objective by presenting a phase diagram for various aggregation patterns obtained by tuning the operational frequency and input power for the single-system. Lastly, the optimal power and frequency for concentric particle trapping and cluster formation were examined and compared to the results obtained previously for the multi-system.

5.4.1 Temporal evolution at 100 mW

An experimental comparison of particle aggregation patterns between a multi-system and a single-system at a fixed power of 100 mW was conducted. The results of the particle aggregation for the 80 MHz single-system at various operational frequencies (20 MHz, 40 MHz and 120 MHz) are shown in Figure 5.16. Note that the operational frequency of 80 MHz is excluded, as it is the same as for the multi-system where both the design and operational frequency are set to 80 MHz (Fig. 5.1). This implies that the single-system 80MHz operating at its respective frequency of 80 MHz is able to aggregate the 7 μm PS particles into a single cluster and later also into multi clusters as seen in Sec. 5.1 and Sec. 5.3. Likewise, the single-system operating at 120 MHz can aggregate particles into multiclusters, which is equivalent to the behaviour observed for the 120 MHz multi-system (Fig. 5.1). Another similarity is the location of the clusters in the top region of the droplet in both systems, which is advantageous for applications requiring particle extraction from the fluid. It is important to note from Figure 5.16 that the single-system requires more time to aggregate clusters compared to the multi-system, despite operating at the same input power of 100 mW.

In both single- and multi-system setups, a low frequency of 20 MHz results in the trapping of particles into 2D concentric ring patterns at the bottom. However, the concentric rings were thinner and discontinuous for the single-system. Furthermore, increasing the frequency to 40 MHz caused the particles to be distributed with no concentric rings formed. After some time, 40 MHz managed to produce macro particles, where single particles assembled together to form larger particles. This pattern is further explained in the next subsection, Sec 5.4.2.

Experiments conducted at low-frequency ranges of 20 MHz and 40 MHz, with a power output of 100 mW for the single-system, revealed that there was a decrease in hydrodynamic activity and a significant increase in radiation force within the droplet compared to higher
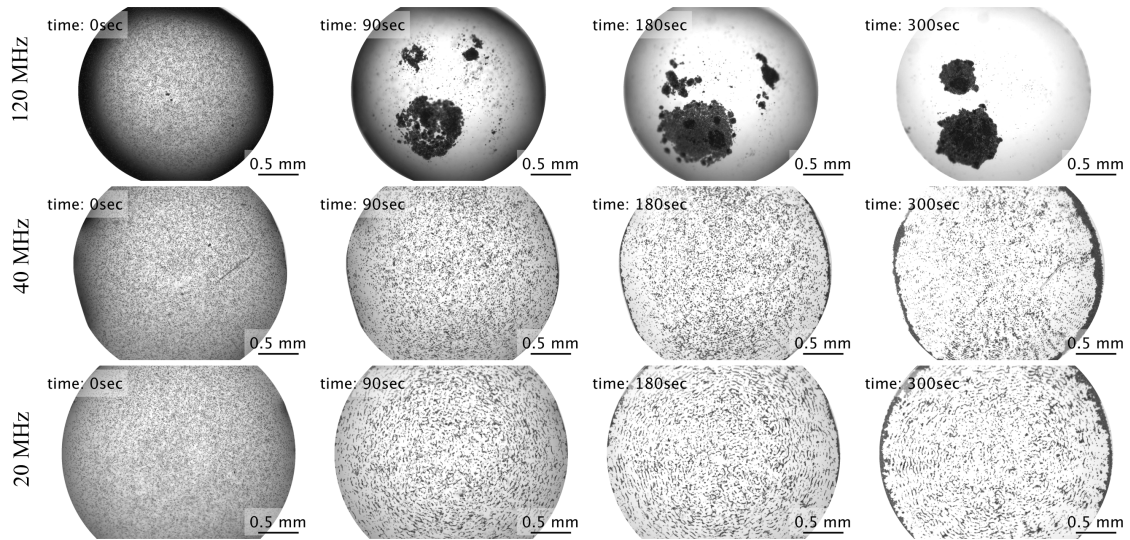
Figure 5.16: Temporal evolution at the targeted frequencies 20 MHz, 40 MHz and 120 MHz at 100 mW for the single-system. Note that the 80 MHz is not included here since the single-system at 80 MHz is similar to the traditional multi-system presented in Fig. 5.1. A similar tendency of the aggregation pattern occurs for the single-system as for the multi-system; namely, higher frequencies are capable of producing clusters while lower frequencies entrap particles at the bottom. 20 MHz manages to form a concentric pattern, whereas 40 MHz does not. 40 MHz produced rather than macro particles, i.e. assemblies of a small portion of individual particles that manage to aggregate together to form a larger particle.

frequencies. This shifting tendency of the dominant force is similar to the multi-system. Consequently, the majority of particles were found to be trapped at the bottom of the droplet at lower frequencies. However, some dissimilarities between the two systems occurred. Unlike the multi-system, particles trapped for the single-system were found to cover not only the regions closer to the periphery but also the central bottom of the droplet at low-frequency ranges. Additionally, unlike the multi-system at 100 mW, fewer particles were observed to flow with the hydrodynamic streamlines, particularly at 40 MHz. This indicates less severe hydrodynamic effects in the droplet for the single-system compared to the multi-system at the same input power of 100 mW.

The results of the single-system experiments showed that the particle aggregation pattern is influenced by both the design and operational frequency of the acoustofluidic device. The single-system can achieve similar cluster aggregation as the multi-system for high frequency. However, the cluster aggregation time is longer for the single-system than the multi-system at the same input power. The longer cluster aggregation time for higher frequencies and fewer particles following the flow at lower frequencies suggests that less hydrodynamic is induced for the single-system compared to the multi-system at the same input power. Consequently, this indicates that the optimal configuration for the most efficient power transmission is when the operational frequency is equal to the design frequency.

This can also be understood from the S-parameter explained in Sec. 2.6. A system typically obtains a low S-value for the frequency it is designed for, meaning that more power is transmitted into the system when the operational frequency matches the design frequency. The multi-system demonstrates this efficiency, with the majority of the power being transmitted into the system, indicated by the low S-value. The single-system has unequal operational

frequency and design frequency, except for 80 MHz, implying a higher S-value for every operational frequency compared with the multi-system. Consequently, meaning that even though the input power is set to 100 mW, a minor portion of the power is actually transferred to the system compared with the same operating frequency for the multi-system. This can be seen from Tab. 5.7, where the real power into the system is smaller for the single-system. The power that is not transmitted is reflected back to the SAW generator.

Table 5.7: The table compares the single-system and the multi-system for the input power, S-parameter and the real power supplied to the system at 20 MHz frequency. Notice, that even though the input power is higher for the single system, less power is actually supplied to the system

System	Input power [mW]	S-parameter [-]	Real power supplied to the system [mW]
Multi-system	99 ± 1	0.086 ± 0.003	90 ± 1
single-system	105 ± 1	0.183± 0.001	85.4 ± 0.2

The real power transmitted to the multi-system has a direct impact on the hydrodynamic behaviour of the system, resulting in faster particle aggregation into clusters compared to the single-system. Nevertheless, the experiments demonstrate that the single-system has the potential to generate similar aggregation clusters as the multi-system.

The higher S-parameter also appears for the lower frequency range of 20 MHz and 40 MHz. Less power is transferred into the acoustofluidic system, resulting in less hydrodynamics inside the droplet. There is no dominant drag force induced by the acoustic streaming, nor centripetal force, resulting in the acoustic radiation force along the bottom being the dominating one, causing the trapping of almost every particle into either macro particles or ring formation. Due to less hydrodynamics, the poloidal flow field has a negligible effect and does not interfere with the particles in the central region at the bottom. Therefore, particles are also trapped in the central bottom region at low frequencies, unlike the behaviour of the multi-system.

5.4.2   single-system aggregation regimes

Experiments showed a greater match between the particle aggregation patterns for the multi-system and the single-system by tuning the power. For instance, increasing the power to 200 mW for the 120 MHz configuration resulted in faster multicluster aggregation. By analysing the influence of both operational frequency and input power, potential new aggregation regions are possible to observe.

The experiments were conducted at various frequencies (20 MHz, 40 MHz, 60 MHz, 80 MHz, and 120 MHz) and input powers (0.5 mW, 1 mW, 2 mW, 5 mW, 10 mW, 20 mW, 50 mW, 100 mW, 200 mW and 300 mW). The maximum input value was set to 300 mW as a further increase in power evidently showed to be able to break the lithium niobate substrate. The results of the aggregation regimes are shown in the semi-logarithmic phase diagram depicted in Fig. 5.17b. The characteristics were evaluated at the middle temporal stage of the droplet's lifetime. Six regimes are mapped in subfigure Fig. 5.17a, where the concentric rings and levitating cluster aggregation presented by configurations A and F, respectively, are of the highest interest. Concentric rings (A) are formed at low frequency and over a wide range of input powers, whereas the levitating clusters are produced for high frequency and high input

power where the hydrodynamics in the droplet are most severe. These processes are already discussed previously in Sec. 5.1).

(a)

(b)
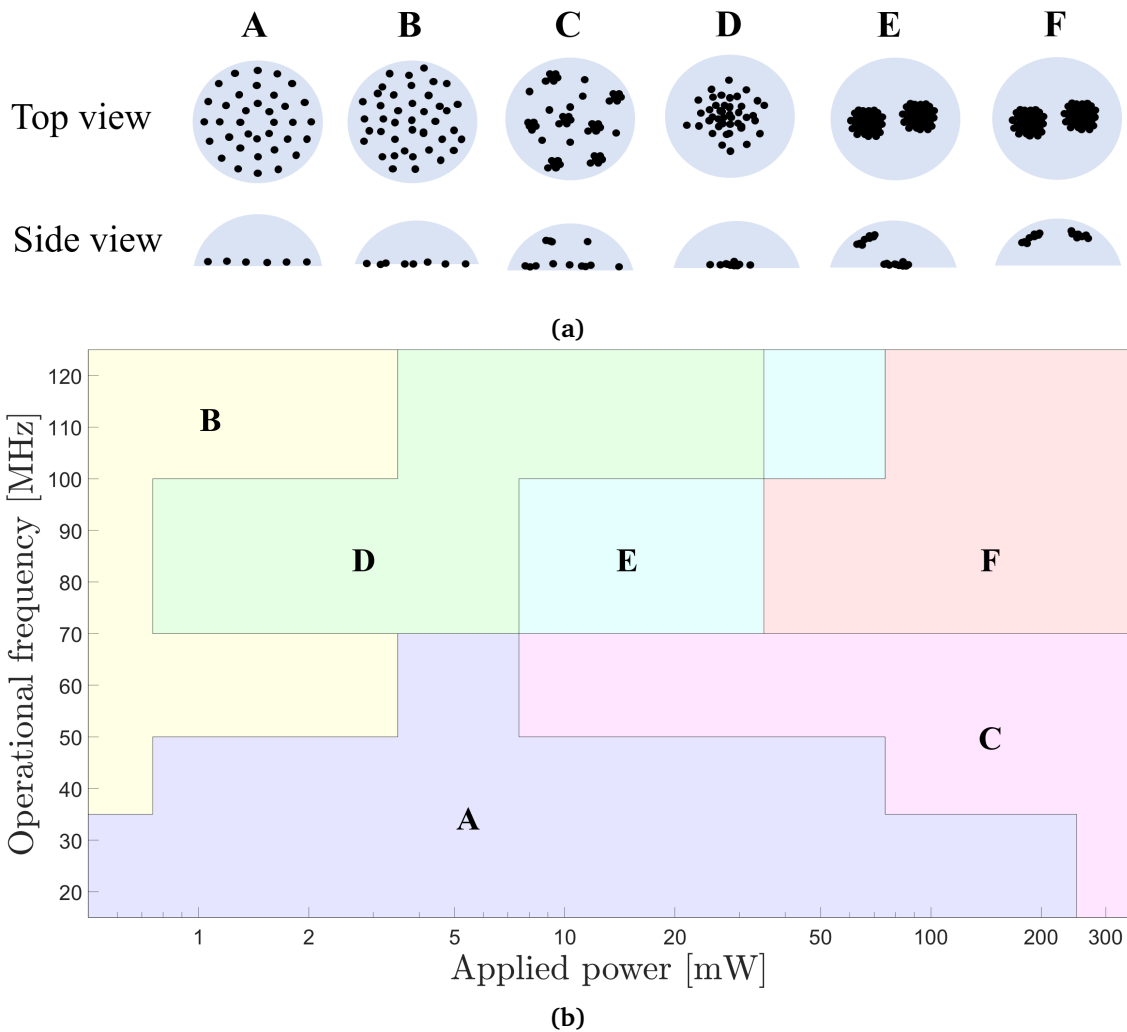
Figure 5.17: Phase diagram for the 80 MHz single-system. a) Subfigure of the various particle behaviour regimes obtained at different input powers and frequencies for the 80 MHz single-system. The letters above each configuration correspond with the letter on the phase diagram. The subfigure illustrates the particle behaviour from a top view and side view. A: Concentric particle trapping. B: Disperse particles. C: Macro particles. D: Accumulation of particles. E: Combination of sedimented and levitating particle clusters. F: Levitating single- and multiclusters. b) Phase diagram showing the various particle behaviour regimes obtained at different frequencies and input powers.

Furthermore, dispersed particles are to be found at low power over a wide range of frequencies, indicated by configuration B in the phase diagram. This region is characterised by low input power. In fact, the power is so low that neither the acoustic radiation force, acoustic streaming, nor the centripetal force manages to effectively influence the behaviour of the particles. For the higher frequency range, the attenuation length plays a major role. As mentioned previously, higher frequencies result in lower attenuation length along the solid-liquid interface. For attenuation length way smaller than the radius, the incoming opposite SAWs

won't interfere with each other, and a standing SAW field capable of effectively trapping particles into concentric rings does not appear. The particles seem to disperse even for the lowest frequency of 40 MHz, which exhibits the ability for standing SAW field due to a longer attenuation length. One possible explanation is that the low input power provides SAW with a lower amplitude [78]. The induced pressure waves will exhibit a small amplitude, resulting in a small pressure gradient that acts on the particles. The small pressure gradient is not large enough to create deep trapping wells capable of efficiently entrapping 7 μm particles. Forces that arise from the absence of the acoustic radiation force, drag force and centripetal force are the buoyancy and gravitational forces. Since the PS particles exhibit a slightly greater density than the water, the net force between the buoyancy and the gravity acts downwards, making the particles sediment at the bottom of the droplet in a randomised pattern.

Configuration C illustrates the formation of macro particles, i.e. single particles that accumulate together and form larger particles. The majority of the particles are trapped at the bottom at this low-frequency range, and some particles follow the increased hydrodynamic inside the droplet. The increased power emits more energy into the system, which results in mini vortices that are strong enough to aggregate a portion of the closest particles into a macro particle. Figure 5.18 shows the instantaneous vorticity field in the central region of the droplet. In multiple tiny regions, the vorticity manages to circulate the flow field in mini vortices that are capable of accumulating small portions of particles into a macro particle.

Configuration D represent the accumulation of particles at the centre bottom of the droplet. These cases occur at high frequency at a wide range of powers, as indicated in the phase diagram. In this configuration, the power is strong enough to cause a significant hydrodynamic effect, leading to particle accumulation. However, the power is still relatively low, preventing the particles from aggregating into a cluster. A potential explanation for the observed phenomenon is that the 7 μm particles sedimented at the bottom of the droplet are prone to the no-slip condition at the interface between the liquid and the solid substrates. However, simultaneously, these particles are subjected to a velocity gradient due to the low velocities present in the region close to the bottom of the droplet. The velocity gradient induces a rolling motion of the particles as explained by the work of Song et al. [20]. The velocity near the bottom tends to move towards the centre, similar to the poloidal flow shown in Fig. 5.10, consequently inducing a rolling motion of the particles towards this central region. One reason why the flow is moving in this direction is due to the short attenuation length for higher frequencies. The attenuation length is shorter than the radius of the droplet, implying that only travelling SAW along the solid-liquid interface is present. The travelling waves will push the particles near the bottom radially inwards with the flow field close to the bottom. Even though the particles manage to accumulate in the centre, the hydrodynamic does not manage to compress them into a cluster.

Increasing the input power for the high-frequency range results in a flow field capable of accumulating and compressing the particles together into clusters. This is presented as configuration E. The increase in power emits more energy into the flow in the form of acoustic streaming, which induces more severe hydrodynamics in the flow such that stronger vortices are produced. At this point, a forced vortex motion is established where the vortex generates a concave surface and therefore concave isobars as described in Sec. 2.4.1. The vortices are strong enough to compress the particles together to form clusters. However, the clusters are a larger accumulation of particles that exhibits a larger mass, hence it requires more effort in order to levitate them. The hydrodynamic is capable of levitating the mass of single particles and
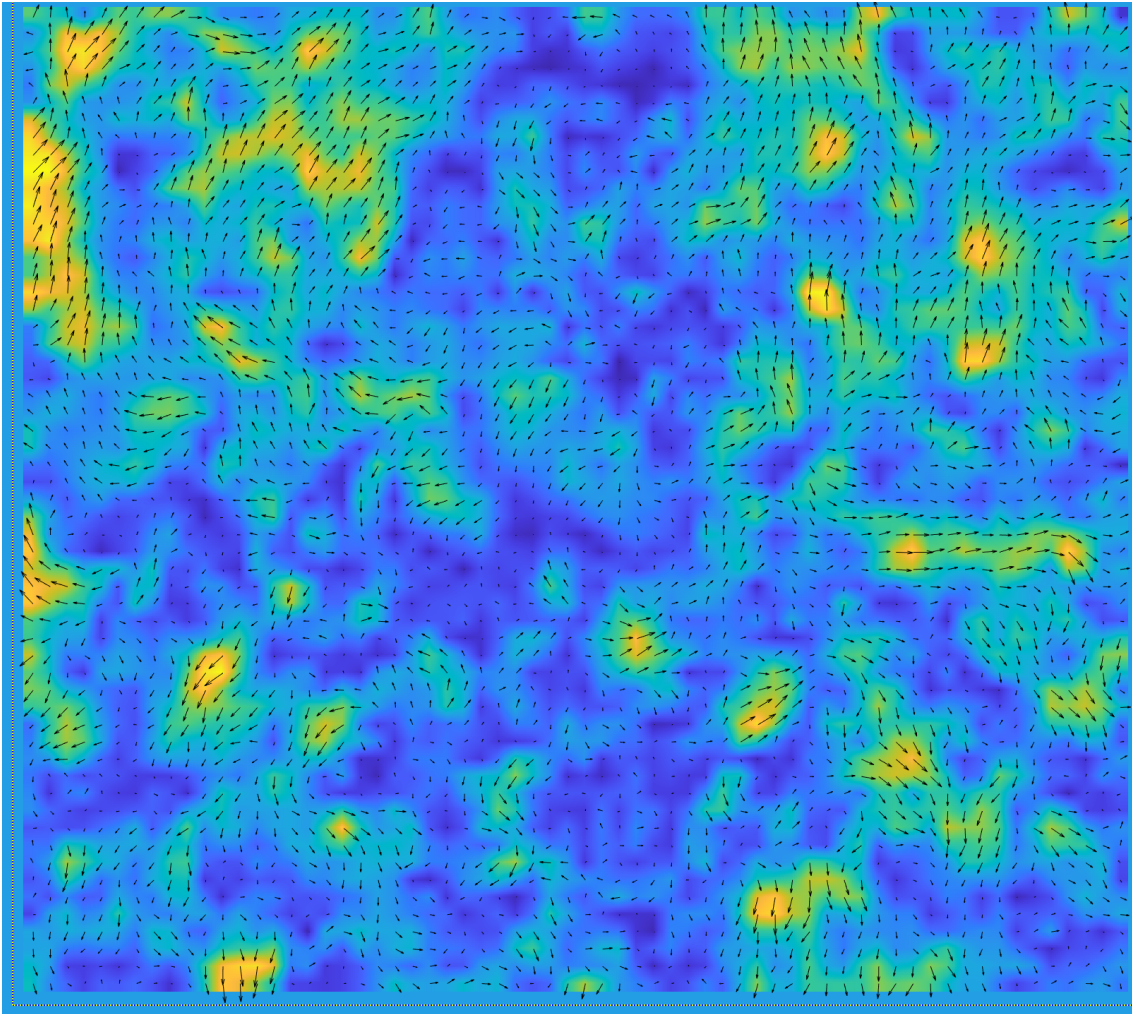
Figure 5.18: PIV measurements of the instantaneous local vorticity field for the 120 MHz single-system configuration. Multiple tiny vortices are to be observed in the flow field. In the many tiny regions, the vorticity manages to circulate the flow field in mini vortices that are capable of accumulating small portions of particles into a macro particle. Configuration C represents the macro particle aggregation pattern.

tiny clusters, but it is not strong enough to levitate the mass of larger clusters. Consequently, some smaller clusters are able to be levitated while others are left on the bottom.

It was found that the frequency of 60 MHz is a hybrid region between the entrapped particles produced at low frequencies and cluster formation occurring at high frequencies. For example, in the case of a 60 MHz single-system at 100 mW, there was observed an evolution of the particle behaviour. Macro particles and concentric rings, configuration A and C respectively, were formed in the beginning and intermediate phases but then accumulated into the central region later on, characterised by configuration D. From this point, a clear poloidal flow was observed that managed to compress and levitate particles to the top of the droplet, very much like configuration E. So a frequency of 60 MHz is able to produce hybrid configurations.

A wider droplet for the 60 MHz frequency will result in the exclusion of a standing SAW field, implying that hydrodynamic effects are dominant and cluster formation is more likely to

occur. On the contrary, if the width of the droplet is narrower such that the attenuation length along the solid-liquid surface is roughly the same distance as the radius of the droplet or larger, the standing SAW field will more effectively entrap particles in concentric rings. For the case used in the experiments of the single-system operating at 60 MHz frequency, the diameter of the droplet exhibited a smaller width compared to the other experiments. This was mainly due to a cleaning procedure where the substrate was cleaned with tap water after each experiment in order to try to change the surface energy, hence also obtaining a droplet with a higher initial contact angle. In turn, this narrows the width of the droplet. All other experiments for both the multi-system and the single-system were cleaned with the same procedure of 70% ethanol followed by isopropanol (IPA) to maintain a consistent lower initial contact angle. The radius of the droplet for 60 MHz at 100 mW was 1.0 mm ± 0.1 mm, and the attenuation length for 60 MHz given by Eq. 2.4 was calculated to be 0.83 mm. An attenuation length that is fairly close to the radius has the ability to obtain concentric particle trapping through a standing SAW field. This is because the attenuation length represents the length of the waves as they decay with a factor of e, not until the waves are fully attenuated, as seen previously for the 40 MHz multi-system. Meaning that the waves are still able to interfere with each other to establish a standing SAW field. This is one reason that explains why the 60 MHz single-system configuration is able to produce concentric rings. Furthermore, macro particles are obtained for higher input powers since the increase in power leads to the formation of mini vortices that manage to trap particles, as described above.

Knowing the various aggregation pattern accessible for the single-system, further analysis is conducted to find the optimal configuration for concentric particle trapping and cluster aggregation.

5.4.3 Optimal single-system configuration for concentric particle trapping and cluster aggregation

Until now, the same aggregation pattern is indeed achievable, namely concentric particle trapping and cluster aggregation, for both systems by tuning the frequency and the power of the single-system. This subsection will attempt to find the optimal configuration for the single-system to produce concentric particle trapping and cluster aggregation, similar to the pattern found for the multi-system.

Concentric particle trapping

Experiments showed a tendency to form concentric particle rings for low frequencies where the acoustic streaming is sufficiently low, and the acoustic radiation force dominates due to the longer attenuation length. Further investigations showed that the most optimal input power was 5 mW and 10 mW for the operational frequencies of 20 MHz and 40 MHz, respectively. Figure 5.19 shows the single-system for the 20 MHz and 40 MHz configurations. At the bottom of the droplet, there are circular patterns of particles. The rings are more closely spaced in the 40 MHz configuration because of the shorter distance between the pressure nodes due to the shorter wavelength. Consequently, the 40 MHz configuration exhibits a higher amount of pressure nodes or pressure wells for the particles to attract to. Therefore, the bottom of the droplet seems more dispersed with particles compared to the 20 MHz configuration.

When operating a single-system at lower power inputs, the particle motion decreases compared to a multi-system operating at 100 mW. This decrease leads to more particles depositing
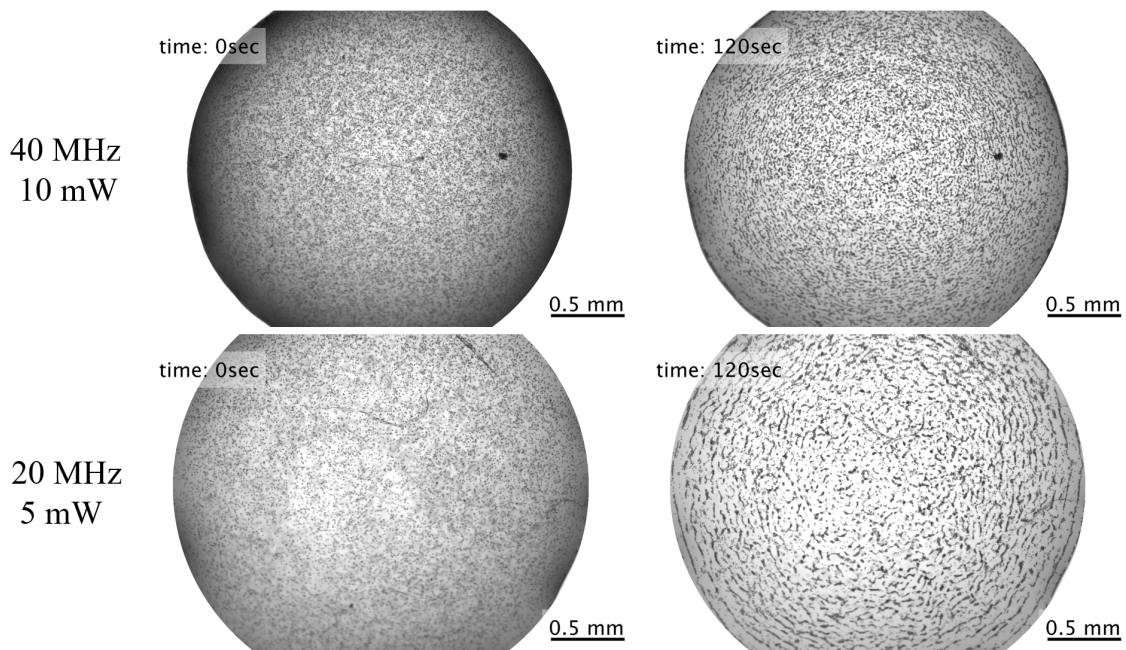
Figure 5.19: Temporal evolution of the low frequency of 20 MHz and 40 MHz for the optimal input power of 5 mW and 10 mW, respectively, for concentric rings formation in the single-system.

at the bottom, resulting in the formation of continuous concentric rings. Therefore, it is re-commended to use lower power inputs to achieve better 2D particle trapping. However, too low power inputs may not have a significant impact on particle behaviour, as indicated by the phase diagram for the single-system operating at 40 MHz and 0.5 mW input power. Lower power levels were found to generate pressure waves with insufficient amplitude to separate particles into distinct rings. Hence, an input power of 10 mW for the 40 MHz configuration is chosen as the optimal one. In the 20 MHz configuration, a power input of 5 mW was selected to achieve well-defined rings.

Cluster aggregation

The temporal evolution of the single-system at 100 mW given by Fig. 5.16 indicated that an increase in power would be suitable for reducing the time in which the system manages to create clusters for the highest frequency of 120 MHz. Experiments conducted for the single-system at input power above 100 mW showed a decrease in the aggregation time. However, high input power led to more fluctuations in the flow field and, therefore, created more unstable cluster formations. The most optimal input power was found to be 200 mW due to its ability to effectively produce stable multiclusters while simultaneously exhibiting a faster aggregation time compared to lower powers. Figure 5.20 shows the formation of multicluster aggregation from dispersed 7 μm PS particles inside a 2 μL droplet for 200 mW input power in the single-system operating at 120 MHz. Unlike the multi-system operating at 100 mW, the aggregation time for the single-system to produce multicluster was longer, even at 200 mW. However, the clusters for the single-system were more stable and did not disperse and reassembled through the lifetime of the droplet.

To conclude, concentric particle trapping is most optimal to be produced in the low-frequency
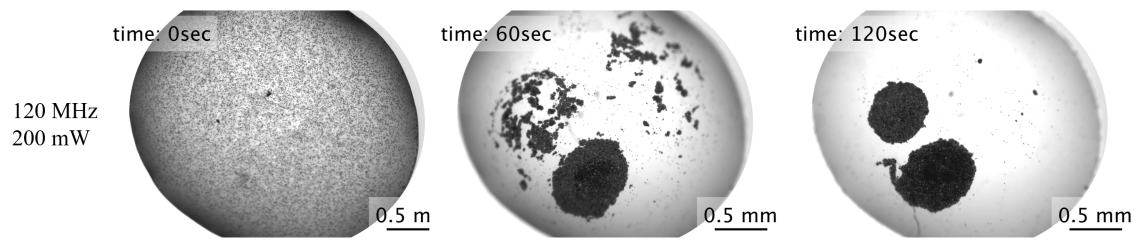
Figure 5.20: Temporal evolution of the high frequency of 120 MHz for the optimal input power of 200 mW for cluster aggregation in the single-system.

range and at a low input power where the hydrodynamics are reduced. For a single system operating at 20 MHz, the ideal input power is 5 mW, while a power of 10 mW is recommended for the 40 MHz configuration. For the highest frequency of 120 MHz, an input power of 200 mW is considered optimal. Lower power than 200 mW resulted in longer aggregation time, while higher power creates a more chaotic flow field and unstable clusters.

Chapter 6

Conclusion

The goal of this thesis was to investigate the particle aggregation pattern inside a sessile droplet subjected to surface acoustic waves (SAW) generated by spiral interdigital transducers (IDT) for various frequencies. Characterisation of the distinct aggregation patterns obtained for 7 μm polystyrene (PS) particles inside a 2 μL sessile was studied. The investigation is conducted experimentally at various frequencies of 20 MHz, 40 MHz, 80 MHz, and 120 MHz with an input power of 100 mW. A qualitative examination of the influential hydrodynamic effects and acoustic radiation force is addressed to gain a broader understanding of the aggregation mechanism.

The results showed that the higher frequencies of 80 MHz and 120 MHz were capable of accumulating the particles into levitating clusters located in the top periphery of the droplet, while lower frequencies of 20 MHz and 40 MHz trapped the particles in 2D concentric rings formation at the bottom. This results from a dominant force conversion corresponding with the frequency range. Hydrodynamic effects induced by the acoustic streaming inside the 2 μL droplet are more dominant at higher frequencies, resulting in multiple vortices in the flow capable of accumulating particles in the vortex centre to create clusters. Conversely, at lower frequencies, the acoustic radiation force along the bottom of the droplet dominates. Surface acoustic waves travelling from opposite sides of the droplet interfere and create pressure nodes that attract the particles towards them, resulting in the entrapment of particles at the bottom.

The high frequencies produced various cluster formations. The 80 MHz frequency produces mainly a single cluster after an average aggregation time of 15 seconds, whereas it takes an average of 54 seconds in order for the 120 MHz frequency to obtain its characteristic multi-cluster assembly. The slower multi-cluster formation for the 120 MHz frequency is mainly caused by the existence of a more chaotic vorticity field where the particles fluctuate more between the vortices and thereby induce a difficulty of accumulating in one specific vortex.

The spacing distance between the concentric rings formed at lower frequencies was characterised. An extensive investigation of the 2D concentric rings formed at 20 MHz and 40 MHz frequencies yielded a spacing distance between the concentric rings that corresponded

with half the wavelength of the acoustic wave in the liquid, not by half the wavelength of the acoustic wave in the lithium niobate as reported in some articles. This implies that the wave motion at the surface of the lithium niobate induces an oscillating movement of the liquid in the region close to the substrate, which in turn is able to entrap particles.

Further examination of the frequency's influence on aggregation pattern revealed that travelling surface acoustic waves at a high frequency were able to entrap particles in concentric rings at the bottom of the droplet. This was experimentally shown for a high frequency of 120 MHz to avoid a standing surface acoustic wave field. Additionally, the hydrodynamic effects in the droplet were reduced by increasing the volume to 40 μL and tuning the power to 10 mW. The spacing of the concentric rings was consistent with the self-intersection theory of two pressure waves, which was caused by wave refraction upon entering the periphery of the droplet.

Furthermore, the thesis introduces a single-system where the design frequency of 80 MHz is fixed, and the operational frequency varies between 20 MHz, 40 MHz and 120 MHz. Operating the single-system at an input power of 100 mW for the various frequencies yielded almost the same aggregation pattern compared to the multi-system. Observations of concentric rings were made at a frequency of 20 MHz, whereas cluster formations were observed at 120 MHz. However, unlike the multi-system, macro particles were produced at a frequency of 40 MHz for the single-system. Subsequent experiments demonstrated that reducing the input power led to a similar occurrence of concentric rings at 40 MHz frequency. A phase diagram was constructed by tuning both the input power and operational frequency, which revealed six aggregation regimes. The phase diagram demonstrated that the single-system can generate the same aggregation pattern as the multi-system by selecting the appropriate input power and operational frequency. The most optimal configuration for concentric particle trapping at low frequencies was found to be 5 mW for the 20 MHz configuration and 10 mW for the 40 MHz configuration. Conversely, a high input power of 200 mW for the 120 MHz configuration was found to be efficient and optimal for multiclusters aggregation.

6.1 Further work

The findings obtained from acoustofluidic particle aggregation provide a foundation for future research in the field. There are numerous opportunities for further exploration, and this section will highlight some important ones.

Firstly, one potential progression in particle manipulation is to separate particles of varying diameters, even down to the nanometer scale. While some researchers have achieved this feat with smaller particles, previous methods have primarily relied on straight or tilted circular IDTs. However, there is potential to utilize spiral IDTs for separating both nanoparticles and microparticles.

Secondly, the implementation of bioparticles or biosamples would be of high interest given that the main goal is to use the obtained results for bioapplications. It would be worthwhile to conduct further investigations to confirm the findings using bioparticles.

Finally, a potential advancement to consider is the incorporation of an extraction method into the system. The droplet's upper periphery is where aggregated multiclusters of PS particles

are located. As a result, the cluster is more accessible and extracting it would be beneficial for bioapplicatoins and further research of the particles.

Bibliography

[1] A. Marzo, S. A. Seah, B. W. Drinkwater, D. R. Sahoo, B. Long and S. Subramanian, 'Holographic acoustic elements for manipulation of levitated objects,' *Nature communications*, vol. 6, no. 1, p. 8661, 2015.

[2] M. Baudoin, J.-L. Thomas, R. A. Sahely, J.-C. Gerbedoen, Z. Gong, A. Sivery, O. B. Matar, N. Smagin, P. Favreau and A. Vlandas, 'Spatially selective manipulation of cells with single-beam acoustical tweezers,' *Nature Communications*, vol. 11, no. 1, p. 4244, 2020.

[3] F. Martınez-Pedrero and P. Tierno, 'Advances in colloidal manipulation and transport via hydrodynamic interactions,' *Journal of colloid and interface science*, vol. 519, pp. 296–311, 2018.

[4] A. Lenshof and T. Laurell, 'Continuous separation of cells and particles in microfluidic systems,' *Chemical Society Reviews*, vol. 39, no. 3, pp. 1203–1217, 2010.

[5] S. Shrestha, B. Wang and P. Dutta, 'Nanoparticle processing: Understanding and controlling aggregation,' *Advances in Colloid and Interface Science*, vol. 279, p. 102 162, 2020.

[6] J. Huang, Z. Zhu, Y. Zhang, J. Tu, X. Guo and D. Zhang, 'On-chip centrifuge using spiral surface acoustic waves on a zno/glass substrate,' *Sensors and Actuators A: Physical*, vol. 347, p. 113 901, 2022.

[7] H. Ahmed, S. Ramesan, L. Lee, A. R. Rezk and L. Y. Yeo, 'On-chip generation of vortical flows for microfluidic centrifugation,' *Small*, vol. 16, no. 9, p. 1 903 605, 2020.

[8] A. D. Stroock, S. K. Dertinger, A. Ajdari, I. Mezic, H. A. Stone and G. M. Whitesides, 'Chaotic mixer for microchannels,' *Science*, vol. 295, no. 5555, pp. 647–651, 2002.

[9] J. P. Shelby, D. S. Lim, J. S. Kuo and D. T. Chiu, 'High radial acceleration in microvortices,' *Nature*, vol. 425, no. 6953, pp. 38–38, 2003.

[10] K. Zhang, A. Jian, X. Zhang, Y. Wang, Z. Li and H.-y. Tam, 'Laser-induced thermal bubbles for microfluidic applications,' *Lab on a Chip*, vol. 11, no. 7, pp. 1389–1395, 2011.

[11] K. F. Lei and W. J. Li, 'A novel in-plane microfluidic mixer using vortex pumps for fluidic discretization,' *JALA: Journal of the Association for Laboratory Automation*, vol. 13, no. 4, pp. 227–236, 2008.

[12] A. S. W. Ng, W. L. W. Hau, Y.-K. Lee and Y. Zohar, 'Electrokinetic generation of microvortex patterns in a microchannel liquid flow,' *Journal of micromechanics and microengineering*, vol. 14, no. 2, p. 247, 2004.

[13] R. Rong, J.-W. Choi and C. H. Ahn, 'An on-chip magnetic bead separator for biocell sorting,' *Journal of Micromechanics and Microengineering*, vol. 16, no. 12, p. 2783, 2006.

[14]   M. K. Tan, L. Yeo and J. Friend, 'Rapid fluid flow and mixing induced in microchannels using surface acoustic waves,' *Europhysics Letters*, vol. 87, no. 4, p. 47003, 2009.

[15]   J. Rezaie, M. Feghhi and T. Etemadi, 'A review on exosomes application in clinical trials: Perspective, questions, and challenges,' *Cell Communication and Signaling*, vol. 20, no. 1, pp. 1–13, 2022.

[16]   F. Petersson, A. Nilsson, C. Holm, H. Jönsson and T. Laurell, 'Separation of lipids from blood utilizing ultrasonic standing waves in microfluidic channels,' *Analyst*, vol. 129, no. 10, pp. 938–943, 2004.

[17]   D. J. Collins, B. Morahan, J. Garcia-Bustos, C. Doerig, M. Plebanski and A. Neild, 'Two-dimensional single-cell patterning with one cell per well driven by surface acoustic waves,' *Nature communications*, vol. 6, no. 1, p. 8686, 2015.

[18]   J. P. Mazzoccoli, D. L. Feke, H. Baskaran and P. N. Pintauro, 'Development of multilayered cell-hydrogel composites using an acoustic focusing technique,' *Biotechnology progress*, vol. 26, no. 2, pp. 600–605, 2010.

[19]   J. L. Han, H. Hu, Q. Y. Huang and Y. L. Lei, 'Particle separation by standing surface acoustic waves inside a sessile droplet,' *Sensors and Actuators A: Physical*, vol. 326, p. 112731, 2021.

[20]   S. Song, J. Zhou and A. Riaud, 'Effect of viscosity on surface acoustic wave driven collective particle dynamics in sessile droplets: Cloud, cavities, and aggregates,' *Physics of Fluids*, vol. 34, no. 8, p. 083604, 2022.

[21]   G. Destgeer, H. Cho, B. H. Ha, J. H. Jung, J. Park and H. J. Sung, 'Acoustofluidic particle manipulation inside a sessile droplet: Four distinct regimes of particle concentration,' *Lab on a Chip*, vol. 16, no. 4, pp. 660–667, 2016.

[22]   N. Zhang, J. P. Zuniga-Hertz, E. Y. Zhang, T. Gopesh, M. J. Fannon, J. Wang, Y. Wen, H. H. Patel and J. Friend, 'Microliter ultrafast centrifuge platform for size-based particle and cell separation and extraction using novel omnidirectional spiral surface acoustic waves,' *Lab on a Chip*, vol. 21, no. 5, pp. 904–915, 2021.

[23]   B. M. Qvenild-Svennungsen, *Surface acoustic waves actuation for microparticle aggregation inside a sessile droplet*, 2022.

[24]   M. Wu, A. Ozcelik, J. Rufo, Z. Wang, R. Fang and T. Jun Huang, 'Acoustofluidic separation of cells and particles,' *Microsystems & nanoengineering*, vol. 5, no. 1, pp. 1–18, 2019.

[25]   N. Norouzi, H. C. Bhakta and W. H. Grover, 'Sorting cells by their density,' *PloS one*, vol. 12, no. 7, e0180520, 2017.

[26]   L. Rayleigh, 'On waves propagated along the plane surface of an elastic solid,' *Proceedings of the London mathematical Society*, vol. 1, no. 1, pp. 4–11, 1885.

[27]   O.-A. K. Kavli, *Surface acoustic wave acoustophoresis for microfluidic based micron and submicron particle separation*, 2016.

[28]   M. Stringer, Z. Zeng, X. Zhang, Y. Chai, W. Li, J. Zhang, H. Ong, D. Liang, J. Dong, Y. Li *et al.*, 'Methodologies, technologies, and strategies for acoustic streaming-based acoustofluidics,' *Applied Physics Reviews*, vol. 10, no. 1, p. 011315, 2023.

[29]   D. Ciplys and R. Rimeika, 'Measurements of electromechanical coupling coefficient for surface acoustic waves in proton-exchanged lithium niobate,' *Ultragarsas/Ultrasound*, vol. 33, no. 3, pp. 14–20, 1999.

[30] W. Pabst and E. Gregorová, 'Elastic properties of silica polymorphs–a review,' *Ceramics-Silikaty*, vol. 57, no. 3, pp. 167–184, 2013.

[31] H. Li, C. Tian and Z. D. Deng, 'Energy harvesting from low frequency applications using piezoelectric materials,' *Applied physics reviews*, vol. 1, no. 4, p. 041 301, 2014.

[32] P. Benech and J. Duchamp, 'Piezoelectric materials and their applications in radio frequency domain and telecommunications,' *Advances in Applied Ceramics*, vol. 114, no. 4, pp. 220–225, 2015.

[33] J. A. Capobianco, W. Y. Shih, G. P. Adams and W.-H. Shih, 'Label-free her2 detection and dissociation constant assessment in diluted human serum using a longitudinal extension mode of a piezoelectric microcantilever sensor,' *Sensors and Actuators B: Chemical*, vol. 160, no. 1, pp. 349–356, 2011.

[34] W. D. Callister jr and D. G. Rethwisch, 'Materials science and engineering,' in 9th ed. John Wiley Sons, 2015, ch. 3.

[35] D. Mandal and S. Banerjee, 'Surface acoustic wave (saw) sensors: Physics, materials, and applications,' *Sensors*, vol. 22, no. 3, p. 820, 2022.

[36] W. Connacher, N. Zhang, A. Huang, J. Mei, S. Zhang, T. Gopesh and J. Friend, 'Micro/nano acoustofluidics: Materials, phenomena, design, devices, and applications,' *Lab on a Chip*, vol. 18, no. 14, pp. 1952–1996, 2018.

[37] H. Bardaweel, O. Al Hattamleh, R. Richards, D. Bahr and C. Richards, 'A comparison of piezoelectric materials for mems power generation,' in *Proceedings of the 6th International Workshop on Micro and Nanotechnology for Power Generation and Energy Conversion Applications, Berkeley, CA, USA*, vol. 29, 2006.

[38] P. Panda and B. Sahoo, 'Pzt to lead free piezo ceramics: A review,' *Ferroelectrics*, vol. 474, no. 1, pp. 128–143, 2015.

[39] E. Directive and I. RoHS, 'Restriction of the use of certain hazardous substances in electrical and electronic equipment,' *European Union, Brussels, Belgium, Report*, no. A7-0196, 2010.

[40] K. Shibayama, K. Yamanouchi, H. Sato and T. Meguro, 'Optimum cut for rotated y-cut linbo 3 crystal used as the substrate of acoustic-surface-wave filters,' *Proceedings of the IEEE*, vol. 64, no. 5, pp. 595–597, 1976.

[41] R. Arzt, E. Salzmann and K. Dransfeld, 'Elastic surface waves in quartz at 316 mhz,' *Applied Physics Letters*, vol. 10, no. 5, pp. 165–167, 1967.

[42] M. B. Dentry, L. Y. Yeo and J. R. Friend, 'Frequency effects on the scale and behavior of acoustic streaming,' *Physical Review E*, vol. 89, no. 1, p. 013 203, 2014.

[43] J. Kushibiki, H. Takahashi, T. Kobayashi and N. Chubachi, 'Characterization of linbo3 crystals by line-focus-beam acoustic microscopy,' *Applied physics letters*, vol. 58, no. 23, pp. 2622–2624, 1991.

[44] M. Holmes, N. Parker and M. Povey, 'Temperature dependence of bulk viscosity in water using acoustic spectroscopy,' in *Journal of Physics: Conference Series*, IOP Publishing, vol. 269, 2011, p. 012 011.

[45] B. L. inc., *Product selection*, Last accessed 23 May 2023, 2023. [Online]. Available: https://www.bangslabs.com/product-selection/FSDG007.

[46] L. V. King, 'On the acoustic radiation pressure on spheres,' *Proceedings of the Royal Society of London. Series A-Mathematical and Physical Sciences*, vol. 147, no. 861, pp. 212–240, 1934.

[47] K. Yosioka and Y. Kawasima, 'Acoustic radiation pressure on a compressible sphere,' *Acta Acustica united with Acustica*, vol. 5, no. 3, pp. 167–173, 1955.

[48] L. Bellebon, H. R. Sugier, J. Larghero, J. Peltzer, C. Martinaud, M. Hoyos and J.-L. Aider, 'Characterization of mesenchymal stromal cells physical properties using acoustic radiation force,' *Frontiers in Physics*, p. 715, 2022.

[49] Y. A. Cengel and J. M. Cimbala, 'Fluid mechanic: Fundamentals and applications,' in 3rd ed. McGraw-Hill Education, 2014, ch. 2,3,11.

[50] N. Adam, 'Use of the term 'young's equation'for contact angles,' *Nature*, vol. 180, no. 4590, pp. 809–810, 1957.

[51] H. Nam, H. J. Sung, J. Park and J. S. Jeon, 'Manipulation of cancer cells in a sessile droplet via travelling surface acoustic waves,' *Lab on a Chip*, vol. 22, no. 1, pp. 47–56, 2022.

[52] MATLAB, *Standard deviation*, Last accessed 26 May 2023. [Online]. Available: `https://se.mathworks.com/help/matlab/ref/std.html`.

[53] F. F. Chen, *Introduction to Plasma Physics and Contolled Fusion*, 3rd ed. Springer, 2018.

[54] W. Petasch, B. Kegel, H. Schmid, K. Lendenmann and H. U. Keller, 'Low-pressure plasma cleaning: A process for precision cleaning applications,' *Surface and Coatings Technology 97*, pp. 176–181, 1997.

[55] K. A. Reinhardt and W. Kern, *Handbook of Silicon Wafer Cleaning Technology*, 3rd ed. Elsevier Inc., 2018.

[56] J. J. Licari and L. R. Enlow, 'Hybrid microcircuit technology handbook: Materials, processes, design, testing and production,' in 2nd ed. William Andrew Inc, 1998, ch. 3.

[57] DuPont, 'Distribution dupont electronic imaging products,' DuPont, Tech. Rep., Oct. 2021.

[58] FindLight, *Ar coating techniques: Thin film deposition methods*, Last accessed 6 Juni 2023, 2017. [Online]. Available: `https://www.findlight.net/blog/ar-coating-techniques/`.

[59] S. R. Corperation, *Heidelberg instruments mla150 the advanced maskless aligner for rd and low-volume production*, Last accessed 30 May 2023. [Online]. Available: `https://www.spectraresearch.com/product/maskless-aligner-150/`.

[60] M. Vafaiee, M. Vossoughi, R. Mohammadpour and P. Sasanpour, 'Gold-plated electrode with high scratch strength for electrophysiological recordings,' *Scientific Reports*, vol. 9, no. 1, pp. 1–11, 2019.

[61] bandelin, *Applications of ultrasonic cleaning devices*, Last accessed 18 May 2023. [Online]. Available: `https://bandelin.com/anwendungen/`.

[62] E. O. Inc., *4x objective, nikon cfi plan fluor*, Last accessed 30 April 2023. [Online]. Available: `https://www.edmundoptics.com/p/4x-objective-nikon-cfi-plan-fluor/30636/`.

[63] B. P. Documentation, *Resulting frame rate*, Last accessed 30 April 2023. [Online]. Available: `https://docs.baslerweb.com/resulting-frame-rate`.

[64] I. Bangs Laboratories, *Equations - bangs laboratories*, Last accessed 22 May 2023, 2018. [Online]. Available: `https://www.bangslabs.com/sites/default/files/imce/docs/TechNote%20206%20Web.pdf`.

[65] H. Company, *5 μl microliter syringe model 7105 knurled hub (kh) syringe, 24 gauge, 2.75 in, point style 3*, Last accessed 22 May 2023, 2022. [Online]. Available: `https://www.hamiltoncompany.com/laboratory-products/syringes/88000`.

[66] I. Grant, 'Particle image velocimetry: A review,' *Proceedings of the Institution of Mechanical Engineers, Part C: Journal of Mechanical Engineering Science*, vol. 211, no. 1, pp. 55–76, 1997.

[67] W. Thielicke and R. Sonntag, 'Particle image velocimetry for matlab: Accuracy and enhanced algorithms in pivlab,' *Journal of Open Research Software*, vol. 9, no. 1, 2021.

[68] S. Scharnowski and C. J. Kähler, 'Particle image velocimetry-classical operating rules from today's perspective,' *Optics and Lasers in Engineering*, vol. 135, p. 106 185, 2020.

[69] I. I. T. T. Conference, *Ittc - recommended procedure and guidelines, guideline on the uncertainty analysis for particle image velocimetry*, Last accessed 22 May 2023, 2014. [Online]. Available: `https://www.ittc.info/media/9579/75-01-03-03.pdf`.

[70] A. Prasad, R. Adrian, C. Landreth and P. Offutt, 'Effect of resolution on the speed and accuracy of particle image velocimetry interrogation,' *Experiments in Fluids*, vol. 13, pp. 105–116, 1992.

[71] C. J. Kähler, S. Scharnowski and C. Cierpka, 'On the resolution limit of digital particle image velocimetry,' *Experiments in fluids*, vol. 52, pp. 1629–1639, 2012.

[72] R. D. Keane and R. J. Adrian, 'Optimization of particle image velocimeters. i. double pulsed systems,' *Measurement science and technology*, vol. 1, no. 11, p. 1202, 1990.

[73] W. Thielicke and E. Stamhuis, 'Pivlab–towards user-friendly, affordable and accurate digital particle image velocimetry in matlab,' *Journal of open research software*, vol. 2, no. 1, 2014.

[74] R. B. Fisher, *Sub-pixel estimation*, Last accessed 23 May 2023. [Online]. Available: `https://homepages.inf.ed.ac.uk/rbf/PAPERS/spedraft.pdf`.

[75] H. Li, J. R. Friend and L. Y. Yeo, 'Microfluidic colloidal island formation and erasure induced by surface acoustic wave radiation,' *Physical review letters*, vol. 101, no. 8, p. 084 502, 2008.

[76] C. J. Strobl, C. Schäflein, U. Beierlein, J. Ebbecke and A. Wixforth, 'Carbon nanotube alignment by surface acoustic waves,' *Applied physics letters*, vol. 85, no. 8, pp. 1427–1429, 2004.

[77] B. Raeymaekers, C. Pantea and D. N. Sinha, 'Manipulation of diamond nanoparticles using bulk acoustic waves,' *Journal of Applied Physics*, vol. 109, no. 1, p. 014 317, 2011.

[78] M. Alghane, B. Chen, Y. Q. Fu, Y. Li, J. Luo and A. Walton, 'Experimental and numerical investigation of acoustic streaming excited by using a surface acoustic wave device on a 128° yx-linbo3 substrate,' *Journal of micromechanics and Microengineering*, vol. 21, no. 1, p. 015 005, 2010.

[79] C. Devendran, D. J. Collins, Y. Ai and A. Neild, 'Huygens-fresnel acoustic interference and the development of robust time-averaged patterns from traveling surface acoustic waves,' *Physical review letters*, vol. 118, no. 15, p. 154 501, 2017.

Appendix A

Microfabrication protocol

Protocol: Fabrication of IDT

Produced by PhD candidate Diego Sánchez Saldaña for the Thermal Two-Phase Flow Lab.

Photoresist: SPR700

Developer: MF-26A

Note: The substrate is pyroelectric, so be careful with temp ramping!

- **Clean LiNbO3 wafer**
  - Acetone → IPA → N2
  - Plasma clean
    O2 - 50/50 - 5 min

- **Dehydration bake**
  - 115°C for 5 min
  - Cool down on tissue. Reduce the risk of the breaks on the sample due to quick temperature change.

- **Spin coating SPR700**
  - 4000 rpm for 45s
    Ramp 1000 rpm/s

- **Soft bake**
  - 115°C for 1 min
  - Cool down on tissue.

- **Exposure MLA150**
  - Laser: 405 nm - Dose: 110 mJ/cm^2

- **Post Exposure Bake**
  - 115°C for 1 min
  - Cool down on tissue.

- **Developer MF-26A**
  - Take two petri dishes: 1 with developer MF-26A and 1 with water

- Place the sample into the 1 petri dish containing the developer for 1 min. Stir gently for the last 30 seconds.
- Place the sample into the petri dish containing water.
- Rinse: DI water → N2 drying

- **Reflectometer**
  - Check if the exposure went well

- **Metal deposition AJA e-beam evaporation**
  - Target: 10 nm (100 A = 0.1 kA) Ti at a rate of 2 Å/s + 80 nm (800 A = 0.8 kA) Au at a rate of 5 Å/s
  - Follow guidance located at the AJA machine.
  - **Note:** Some trouble with the deposition might occure. In that case, go to *Next menu* and *Quick edit*. From there you can adjust the threshold in which the rate must exceed before starting the deposition. By lowering the threshold, the rate might become sufficient enough to start depositing metal layers.

- **Acetone lift-off**
  - Goal: Ultrasonic bath for 1 min
  - Soak temperature: Room temperature
  - **Note:** Nothing leaves the lift-off area (except the sample ofc)
  - Fill a large beaker with acetone (acetone is found in a large container underneath the working bech / fume hood)
  - Fill the ultrasonic bath with water
  - Place the acetone beaker into the water (it will float)
  - Place the sample into a dipper (the holder with a cross) and place it into the acetone beaker.
  - When the sample is in the dipper, the dipper in the acetone beaker and the acetone beaker in the ultrasonic bath: then push the *sonic ultrashell* button
  - Stops after 1 min
  - Take the beaker out of the sonic bath and take the sample out of the acetone beaker.
  - Hold it over a new beaker and wash it with acetone. Use pointed swamp to clean the sample of gold residues (Scrub pointy swabs only in one direction on the sample for reducing the risk of damage)
  - Wash with IPA → N2 drying

- **Microscope to check surface of the IDT**

- **Saw cutting of the 4-inch LiNbO3 wafer**